

# Micro-mechanics of 3D architected metals synthesized by electrodeposition

THÈSE N° 8442 (2018)

PRÉSENTÉE LE 13 MARS 2018

À LA FACULTÉ DES SCIENCES ET TECHNIQUES DE L'INGÉNIEUR  
GROUPE SCI STI SM  
PROGRAMME DOCTORAL EN SCIENCE ET GÉNIE DES MATÉRIAUX

ÉCOLE POLYTECHNIQUE FÉDÉRALE DE LAUSANNE

POUR L'OBTENTION DU GRADE DE DOCTEUR ÈS SCIENCES

PAR

**Maxime Alain Baptiste MIESZALA**

acceptée sur proposition du jury:

Dr L. Weber, président du jury  
Dr S. Mischler, Dr L. V. S. Philippe, directeurs de thèse  
Prof. A. C. West, rapporteur  
Prof. J. Sort, rapporteur  
Dr Y. Leterrier, rapporteur



ÉCOLE POLYTECHNIQUE  
FÉDÉRALE DE LAUSANNE

Suisse  
2018



# Acknowledgements

First I would like to thank my PhD supervisors Laetitia Philippe and Stefano Mischler for giving me the opportunity to learn and work in their laboratories. I really appreciated their constant help, support and guidance. My sincere thanks also goes to Johann Michler, who provided me an opportunity to join his laboratory.

I would also like to thank the members of my PhD jury: Prof. Jordi Sort, Prof. Alan C. West, Dr. Yves Leterrier and Dr. Weber Ludger.

Even if a PhD thesis is the work of a single person, this manuscript would not be the same without the collaborative experimental work of many people. Therefore I would to thank Jens Bauer and Oliver Kraft from the KIT for providing the 3D micro-architectures. I would also like all the members of Empa Thun who contributed in some way, in particular Madoka, Gaylord, Cédric, Gaylord, Laszlo, Rejin, Jeff, Cristina and all the others that I forget. A special thanks goes to the electrochemistry team and my office mates Keith, Daniele and Juri for their positive attitude and all the fun we had together.

And finally, I would like to express my gratitude to all my colleagues (students, PhDs, post-docs, scientists, technicians and administrative staff), friends and family for their constant encouragement and support throughout this long, exciting and sometimes daunting journey. Thank you. Merci.

*Lausanne, le 20 Décembre 2017*

M. M.



# Abstract

Cellular metallic materials have emerged as a new promising class of materials due to their lightweight porous structures and advanced multi-functional properties. Originally limited to random metallic foams, modern lithography techniques have enabled the design of hierarchical cellular structures with tailored mechanical properties. In addition, the mechanical properties of micro-cellular metals can be further improved by taking advantage of the properties of metals, which are size-sensitive at this length scale. It is therefore expected that the combination of architected cellular designs with size effects in metals would result in materials with unprecedented mechanical properties.

The present thesis aims at investigating and understanding the influence of size effects on the mechanical properties of three-dimensional micro-architected metal structures synthesized using advanced lithography techniques and electrochemical deposition of metals. Electrodeposited copper films with engineered microstructures and nickel-based hierarchical micro-cellular structures were manufactured and tested under uniaxial loading conditions. The results of the tests were used to evaluate the contribution of the size effects and/or architecture to the change in mechanical properties and deformation behavior.

The influence of the intrinsic size effect was first demonstrated in electrodeposited pure copper films. Using nanoscale twins to engineer the grain boundaries, it was possible to produce copper films with high strength and significantly tune the mechanical properties by adjusting the twin orientation.

The combination of size effects was then investigated for two types of micro-architecture. The first type of metal micro-architecture was obtained by plating nanocrystalline Ni inside a self-assembled colloidal crystal of microspheres in order to produce a regular inverse opal. The second type was fabricated by metallizing a 3D polymer template produced by 3D laser lithography with an amorphous NiB coating. Results show that there is a complex interaction

## Acknowledgements

---

between the characteristic external dimension and cellular structure. For regular Ni inverse opal, there is a complex interaction between the ligament size and the grain size which defines the overall strength of cellular metals. In the case of hybrid NiB/polymer structures, the brittle-to-ductile transition in the amorphous NiB coating and the architecture effect are coupled. By varying the NiB thickness and the architecture geometry, it is possible to control the deformation mechanism from global buckling to brittle failure and to tune the energy absorption characteristics of the micro-architectures.

Through these case studies, it was demonstrated that the combination of grain boundary engineering, sub-micron geometrical features and overall architecture can yield 3D metallic micro-architectures, which are both light and strong and have tailored mechanical properties. The mechanical properties of some of these materials exceed the properties of either of the parent materials. Therefore, the constitutive mechanical laws for porous metals should be modified to account for these three effects all together. The results confirmed the potential of our experimental approach and provide a practical way to extend the material property-space.

**Key words:** cellular metals, electrodeposition, mechanical properties, size effects, microcompression.

# Résumé

Récemment les matériaux alvéolaires métalliques ont émergé comme une nouvelle classe de matériaux en raison de leur structure hautement poreuse et de leurs propriétés multifonctionnelles. Historiquement limitées aux mousses métalliques à porosité aléatoire, les techniques de lithographie modernes permettent aujourd'hui de concevoir des métaux alvéolaires avec une architecture régulière et ordonnée pour satisfaire aux propriétés mécaniques requises pour une application particulière. De plus, les propriétés mécaniques des métaux alvéolaires peuvent être améliorées en exploitant les effets de taille dans les métaux qui apparaissent à l'échelle microscopique. Il est donc attendu qu'une structure poreuse architecturée, combinée aux effets de taille dans les métaux, produise des matériaux métalliques avec des propriétés mécaniques uniques.

Le but de cette thèse est la mise en évidence expérimentale des effets de taille sur les propriétés mécaniques des structures métalliques architecturées. Ces structures 3D sont obtenues en combinant des méthodes de microfabrication avancées avec la déposition par voie électrochimique de métaux. Pour ce faire, des couches minces de cuivre avec contrôle des joints de grain et des structures micro-alvéolaires à base de nickel furent élaborées et testées sous sollicitations uniaxiales en compression. Les résultats des tests mécaniques ont permis d'évaluer la contribution des effets de taille et/ou d'architecture sur les performances mécaniques et les modes de déformation des métaux micro-alvéolaires.

L'influence des effets de taille intrinsèque a d'abord été démontrée pour des dépôts électrolytiques de cuivre. En contrôlant la nature des joints de grains, il a été possible de produire des dépôts de cuivre nanomaclé présentant une résistance à la déformation accrue dont la valeur varie avec l'orientation du maillage.

Les interactions entre les effets de taille ont ensuite été étudiées pour deux types de micro-architecture. Le premier type de micro-architecture métallique, appelée opale inverse, est

## Acknowledgements

---

obtenue par dépôt de nickel nanocrystallin dans des cristaux colloïdaux issus de l'auto-assemblage de microsphères de polystyrène. Le second type de micro-architecture est produit par la métallisation electroless d'un dépôt amorphe de NiB sur une structure polymère 3D réalisée par lithographie laser. Les résultats des tests mécaniques ont montré qu'il existe une interaction complexe entre les dimensions externes caractéristiques du dépôt métallique et la structure alvéolaire de ces matériaux. Dans le cas des opales inverses en Ni, la solidité de ces matériaux est donnée par l'interaction entre la taille des ligaments et la taille des grains. Dans le cas des structures alvéolaires hybrides en NiB/polymère, on constate que la transition fragile ductile dans la couche de NiB et l'effet de l'architecture sont couplés. Selon l'épaisseur de la couche de NiB et l'architecture, il est possible de contrôler les modes de déformations et de ruptures de ces micro-architectures

L'étude de ces matériaux a montré qu'en associant une approche d'ingénierie des joints de grain avec une structure alvéolaire organisée dont les caractéristiques géométriques sont d'une taille inférieure au micron, il était possible de produire des micro-architectures 3D en métal qui sont à la fois légères et résistantes et dont les propriétés mécaniques peuvent être finement ajustées. Les propriétés mécaniques de certains de ces matériaux dépassent en effet les propriétés du matériau dont il issu. Les lois de comportement des matériaux micro-poreux doivent donc être modifiées pour intégrer ces phénomènes. Les résultats ainsi obtenus confirment qu'il est possible d'appliquer notre approche expérimentale pour produire des matériaux aux propriétés nouvelles.

**Mots clefs :** métaux cellulaires, électrodéposition, propriétés mécaniques, effets de taille, microcompression.



# Contents

<b>Acknowledgements</b>	<b>i</b>
<b>Abstract (English/Français)</b>	<b>iii</b>
<b>List of figures</b>	<b>xi</b>
<b>List of tables</b>	<b>xvii</b>
<b>List of symbols</b>	<b>xix</b>
<b>List of abbreviations</b>	<b>xxi</b>
<b>Introduction</b>	<b>1</b>
<b>1 Literature review</b>	<b>5</b>
1.1 Cellular metals . . . . .	5
1.1.1 General characteristics . . . . .	6
1.1.2 Properties of cellular materials . . . . .	7
1.1.3 Structure optimization . . . . .	7
1.2 Combining 3D architected with size effects in metals . . . . .	9
1.2.1 Intrinsic size effect . . . . .	9
1.2.2 Intrinsic size effects: the special case of nanoscale twins in copper . . . . .	11
1.2.3 Extrinsic size effect . . . . .	13
1.2.4 Size effects interaction . . . . .	13
1.3 Processes controlling the size effects in metals . . . . .	14
1.3.1 Electrochemical deposition of metals . . . . .	14
1.3.2 Lithography techniques . . . . .	16
	vii

## Contents

---

1.4	Summary of the literature . . . . .	21
1.5	Goals of research . . . . .	22
<b>2</b>	<b>Materials and Methods</b>	<b>25</b>
2.1	Lithography techniques . . . . .	25
2.1.1	UV-LiGA lithography . . . . .	25
2.1.2	Colloidal crystal templating . . . . .	27
2.1.3	2 photon lithography . . . . .	28
2.2	Metal electrodeposition . . . . .	29
2.2.1	Copper with nanoscale twins . . . . .	29
2.2.2	Nanocrystalline nickel . . . . .	30
2.2.3	Electroless Nickel-Boron . . . . .	30
2.3	Microstructural analysis . . . . .	32
2.3.1	Scanning and Transmission electron microscope (SEM & TEM) . . . . .	32
2.3.2	X-Ray Diffraction (XRD) and Reflectivity (XRR) . . . . .	32
2.3.3	Focused Ion Beam . . . . .	33
2.4	Mechanical testing . . . . .	34
2.4.1	Nanoindentation . . . . .	35
2.4.2	Microcompression . . . . .	36
<b>3</b>	<b>Investigation of the intrinsic size effect in electrodeposited copper with nanoscale twins</b>	<b>39</b>
3.1	Introduction and motivation . . . . .	40
3.2	Synthesis of copper with nanoscale twins . . . . .	40
3.2.1	Experimental . . . . .	40
3.2.2	Controlling the twin density . . . . .	41
3.2.3	Controlling the twin orientation . . . . .	43
3.2.4	Twin formation mechanism during pulse plating . . . . .	45
3.3	Mechanical properties . . . . .	45
3.3.1	Experimental . . . . .	46
3.3.2	Influence of twin orientation . . . . .	47
3.3.3	Deformation mechanisms in nt-Cu . . . . .	48

3.3.4 Elastic properties of nt-Cu . . . . .	51
3.4 Summary . . . . .	53
<b>4 Investigation of the extrinsic size effect</b>	<b>55</b>
4.1 Effect of the NiB thickness in micro-lattices . . . . .	55
4.1.1 Control of the NiB film thickness . . . . .	56
4.1.2 Structural properties of the reference film . . . . .	57
4.1.3 Mechanical properties of the reference film . . . . .	57
4.1.4 Mechanical properties of micro-lattices as a function of NiB thickness . . . . .	58
4.1.5 Brittle-to-ductile transition in amorphous NiB . . . . .	61
4.1.6 Load drops analysis as an indirect evidence of brittle-to-ductile transition . . . . .	62
4.2 Effect of the ligament size in nc-Ni inverse opals . . . . .	64
4.2.1 Synthesis of porous regular foams with metals . . . . .	65
4.2.2 Mechanical properties of as-deposited Ni inverse opals . . . . .	69
4.2.3 Is the strength the result of the ligament size? . . . . .	69
4.3 Summary . . . . .	70
<b>5 Investigation of the architecture effect on the mechanical properties</b>	<b>75</b>
5.1 NiB/polymer hybrid micro-architectures . . . . .	75
5.1.1 Strength and stiffness <i>vs.</i> architecture . . . . .	75
5.1.2 Energy absorption <i>vs.</i> architecture . . . . .	77
5.2 Summary . . . . .	78
<b>6 Combination of size effects</b>	<b>83</b>
6.1 Controlling the buckling behavior with ductile to brittle transition in NiB/polymer micro-architectures . . . . .	83
6.2 Combination of intrinsic and extrinsic size effects in inverse opals . . . . .	85
6.2.1 Annealing tests of Ni inverse opals . . . . .	85
6.2.2 Mechanical properties as a function of annealing time . . . . .	86
6.2.3 Reverse approach to measure the strength . . . . .	87
6.2.4 Comparison with other materials from the literature . . . . .	88
6.2.5 Summary . . . . .	89

## Contents

---

<b>7 General discussion</b>	<b>91</b>
7.1 Comparison with other materials . . . . .	91
7.1.1 Scaling laws for Ni inverse opals . . . . .	91
7.1.2 Scaling laws for 3D metal-polymer hybrid micro-architectures . . . . .	92
7.2 Expanding the material property space . . . . .	94
7.3 Towards a unified scaling law including the size effects . . . . .	94
<b>Conclusions</b>	<b>97</b>
<b>Bibliography</b>	<b>114</b>
<b>Curriculum Vitae</b>	<b>116</b>

# List of Figures

1	Ashby material property chart. a) Young's modulus $E$ versus density $\rho$ and b) Strength $\sigma$ versus density $\rho$ . . . . .	1
1.1	SEM micrographs of different types of metallic foams: a) Ultralight Ni/Ag foam with random structures obtained by electroless deposition; b) metallic hollow spheres foam; c) Silver inverse opal obtained by electrodeposition. . . . .	8
1.2	a) Strength of polycrystalline metals as a function of the grain size, known as the Hall-Petch relation. b) Normalized shear stress as a function of the grain size and the sample diameter revealing both the intrinsic and extrinsic size effect in Ni (and Ni-4wt%W). . . . .	10
1.3	Schematic illustration of two types of interfaces: a) a typical grain boundary (GB) and b) a coherent twin boundary (TB). c) Comparison of the mechanical properties of copper with nanoscale twins, nanocrystalline and coarse-grained microstructure. . . . .	12
1.4	UV-LiGA fabrication process for fabricating metallic micro-parts. . . . .	19
1.5	Challenges of electrochemical deposition inside UV-LiGA lithographic features. . . . .	20
1.6	Comparison between single photon polymerization and two photon polymerization. . . . .	21
2.1	Setup for colloidal crystal templating. . . . .	27
2.2	Polymer template fabrication with 3D laser lithography. . . . .	28
2.3	Tilted and top view SEM images of microcellular architectures after NiB metallization. The scale bar in all the images is 10 $\mu\text{m}$ . . . . .	29
2.4	Undeformed (left) and deformed (right) micropillar with geometrical parameters. . . . .	30

## List of Figures

---

2.5	a) Schematic of a dual FIB/SEM instrument. An example of b) a FIB cross-section, c) a micropillar obtained by FIB milling and d) an ion channeling contrast image.	33
2.6	Aleminis nanoindentation platform for compression test installed inside the SEM.	34
2.7	Schematic illustration of a) indentation load-displacement data and b) contact tip geometry with important parameters. c) Residual indentation imprint made by a sharp Berkovich tip.	35
2.8	Undeformed (left) and deformed (right) micropillar with geometrical parameters.	37
3.1	(a-d) TEM micrographs of the corresponding Cu films with horizontally aligned twins (e). TB: twin boundary. GB: grain boundary. SF: stacking fault.	42
3.2	(a-e) Effect of the off-time pulse on the microstructure of Cu films for a fixed on-time of 20 ms and various off-time. The twin density distribution is shown for 2, 3 s and 4 s off-time. f) Texture coefficient of the Cu films as a function of the off-time pulse.	43
3.3	(a-d) TEM micrographs of the corresponding Cu films with vertically aligned twins (e) obtained at -0.6V vs. SCE ( $t_{on} = 20\text{ ms}$ , $t_{off} = 4\text{ s}$ ). TB: twin boundary.	44
3.4	Growth mechanism of nanotwinned copper as a function of the plating potential and pulse off-times.	45
3.5	Ion contrast channeling of the microstructure and micropillars	46
3.6	Representative stress-strain curves for a) quasi-static and b) strain rate jump microcompression.	49
3.7	a) Thompson tetrahedron for twinned fcc crystal in the (111) plane and b) Angular dependence of the Schmid factor for each slip system.	50
3.8	Ion channeling contrast micrographs of (a) ufg-Cu, (b) horizontal nt-Cu and (c) vertical nt-Cu micropillars after compression. A schematic of the deformation mechanisms as a function of the microstructure, slip planes, slip directions and dislocation activity is given for each microstructure (d, e and f respectively). Here GB is grain boundary, T is twin, M is matrix, TB is twin boundary and $\lambda$ is the twin thickness.	51
3.9	Magnitude of the elastic deformation in Cu as a function of the yield stress for several values of Young's modulus.	52

4.1 SEM images showing conformal NiB coverage in complex features and uniform NiB coating thickness for a,d) 10 nm, b,e) 30 nm, and c,f) 100 nm. . . . .	56
4.2 a) XRD diffractogram of the NiB reference on Au-coated Si wafer. Au peaks are indexed in red. b) Bright field image of a representative 30 nm NiB coating. Inset: corresponding SAED pattern. . . . .	57
4.3 Engineering stress-strain curves as a function of the NiB coating thickness for micro-lattice A, B, C, D and E (a, c-f). b) SEM micrographs of structure A during microcompression at various levels of strain for 10 nm, 30 nm and 100 nm NiB coating. . . . .	59
4.4 SEM images of the micro-architectures after compression revealing the ductile nature of NiB at 10 nm but its brittle nature at 100 nm. Scale bars are 1 $\mu\text{m}$ . . .	62
4.5 a) Engineering stress-strain curves for structure A with corresponding $ \Delta\sigma/\Delta\varepsilon $ vs. strain plotted on the same graph. b) Stress drop magnitude against strain. c) Cumulative probability distribution of the stress drops as a function of the stress drop magnitude. Solid lines present a power-law scaling. . . . .	63
4.6 Number of stress drops as a function of the micro-architecture and NiB thickness. 64	
4.7 Schematic of a) nickel inverse opal unit cell and b) cross-section of the unit cell revealing the ligament size. . . . .	65
4.8 Schematic of the process to obtain porous Ni inverse opals by dual templating. 66	
4.9 Schematic of a) the geometry of the pillars with characteristic length $l$ and b) optical microscopy of the corresponding UV-LiGA molds. . . . .	66
4.10 SEM images of the polystyrene colloidal crystals for a) 500 nm, b) 836 nm, and c) 2560 nm PS spheres. The corresponding FFTs are shown in all cases. Color-coded triangular mesh of the corresponding SEM micrographs with sphere orientation (d-f). . . . .	71
4.11 a) Radial distribution function for 500 nm spheres. b) Normalized radial distribution function comparing 500 nm, 836 nm, and 2560 nm PS colloidal crystals. 72	
4.12 SEM images of Ni inverse opal produced with 500 nm polystyrene spheres seen along a) 111, b) {100}, and c) {110} directions. The windows interconnecting the air cavities with those in the underlying plane can be seen: three for 111 faces, four in the case of 100, and five for 110. . . . .	72

## List of Figures

---

4.13 SEM images (a-d) polished dense Ni micropillars and porous (f-h) porous Ni micropillars obtained by UV-LiGA and PS sphere lithography. . . . .	72
4.14 Stress-strain curves of a) dense Ni micropillars and porous Ni micropillars with b) 2560 nm and c) 500 nm pore size. . . . .	73
4.15 Electrodeposited Ni micropillars before and after micrompression with dense a) dense Ni with b) 2560 nm and c) 500 nm pore size. . . . .	73
4.16 FIB cross-section of a Ni inverse opal micropillar with a) 2560 nm and b) 500 nm pore size. . . . .	74
5.1 a) Stress-strain curves for 100 nm NiB coating as a function of the architecture. b) Specific strength $\sigma/\rho$ and modulus $E/\rho$ of the micro-architectures as a function of the NiB coating. . . . .	76
5.2 a) Typical stress-strain curve of micro-archiected structures, showing the important energy parameters and the energy dissipated by a theoretic ideal absorber (area shaded in gray). Variation of b) the plateau stress, c) the absorbed energy per unit volume and d) the energy absorption efficiency versus NiB thickness for each microarchitecture. Solid lines are guidelines for the eyes. . .	80
5.3 (a-e) Energy absorption diagrams for each NiB/polymer hybrid micro-architectures. f) Energy absorption diagrams for micro-architectures with similar density. Comparison with a PE foam and Al foam. . . . .	81
6.1 Model geometry parameters for hollow cylindrical shell and hollow cylindrical shell filled with a compliant core a) before and b) after buckling. c) Buckling wavelength parameter plotted as a function of the radius to thickness ratio. The values for the 3 NiB thicknesses are indicated on the plot. . . . .	84
6.2 FIB images of a) as-deposited nanocrystalline Ni films and annealed 30 minutes at b) 300°C c) 400°C, and d) 500°C. . . . .	85
6.3 Yield strength of Ni inverse opals as a function of the annealing time at 250°C for 500 nm and 2560 nm PS spheres. . . . .	87
6.4 Comparison of our mechanical results with data from the literature considering only the extrinsic size (ligament) or only the extrinsic size (grain) effect. A: annealed, H: hardness and MD: molecular dynamics. . . . .	89



7.1	Material property plot of strength versus density for our Ni inverse opals with current scaling laws. . . . .	92
7.2	Material property plot of a) elastic modulus and b) strength versus density for our NiB/polymer hybrid micro-lattices (red squares) compared with other micro-lattices from literature. . . . .	93
7.3	A strength versus density chart showing the position in the material property space of nanotwinned Cu, Ni inverse opals and 3D hybrid micro-lattices. . . . .	95



# List of Tables

1	Thesis overview. . . . .	4
1.1	Scaling laws of cellulars materials . . . . .	7
2.1	Bath composition and parameters for the electrodeposition of copper with nanoscale twins . . . . .	29
2.2	Bath composition and parameters for the electrodeposition of nanocrystalline nickel . . . . .	30
2.3	Bath composition and parameters for the electroless deposition of NiB . . . . .	31
3.1	Aspect ratio, diameter, $\varnothing$ , and mechanical properties of electrodeposited copper micropillars with fine grained microstructure, vertical twins and horizontal twins. The strength, $\sigma_{5\%}$ , loading modulus, $E$ , strain rate sensitivity exponent, $m$ , and apparent activation volume, $V$ , are given together with the standard deviation. . . . .	48
3.2	Slip plane and twin directions in a twinned crystal . . . . .	51
4.1	Physical and mechanical properties as a function of the NiB thickness for each micro-architecture. . . . .	60
6.1	0.2% offset yield strength (MPa), $\sigma_{0.2\%}$ , of porous Ni inverse opals in as-deposited and annealed conditions. . . . .	86
6.2	Grain size, ligament size, relative density, measured yield stress and calculated ligament strength for Ni inverse opals with 500 nm pore size or 2560 nm pore size. A stands for annealed. . . . .	88



# Nomenclature

$\nu$	Poisson's ratio
$\sigma$	Stress
$\theta$	taper angle of pillar
$\varepsilon$	Strain
$A$	Projected contact area
$C_{Sneddon}$	Sneddon's correction coefficient
$d$	Displacement
$D_0$	Nominal pillar diameter
$E$	Elastic modulus
$E_r$	Reduced modulus
$h_c$	Penetration depth
$h_{max}$	Maximum indentation depth
$L_0$	Initial length of pillar or micro-architecture
$P$	Load
$P_{max}$	Maximum indentation load
$S$	Contact stiffness



# List of Abbreviations

**3D** three dimensional

**APTES** 3-Aminopropyltriethoxysilane

**DMAB** dimethyl amine borane

**fcc** face-centered cubic

**FIB** focused ion beam

**NiB** nickel-boron

**nt-Cu** nanotwinned copper

**PS** polystyrene

**RIE** reactive ion etching

**SAED** selected-area electron diffraction

**SEM** scanning electron microscope

**SRS** strain rate sensitivity

**TEM** transmission electron microscope

**XRD** X-ray diffraction





# Introduction

When examining the Ashby charts [1] in Figure 1, which plot strength and Young's modulus  $E$  as a function of the density  $\rho$ , it is striking that some parts are filled with materials while others are not. It appears that the mechanical properties and densities of traditional materials are coupled; all of the materials lie on the diagonal [2]. At the top right corner, we find materials such as metals and ceramics which exhibit both strong and stiff properties but at the expense of weight. On the other hand, materials located at the bottom left corner, such as polymeric foams, are lightweight but possess weak mechanical properties. The white space in the top left corner of the Ashby charts indicates that light-yet-stiff or light-yet-strong materials are yet to be developed. These "holes" represent great opportunity for extending the material-property space by developing materials with unprecedented property combinations.

Traditional strategies to improve the mechanical properties of materials consist of altering either the microstructure or the composition [3]. Both strategies, albeit successful, have

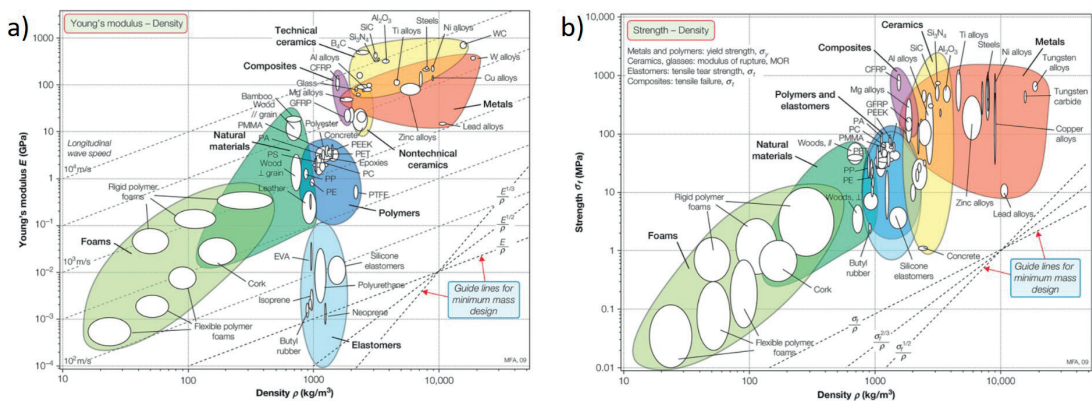


Figure 1 – Ashby material property chart. a) Young's modulus  $E$  versus density  $\rho$  and b) Strength  $\sigma$  versus density  $\rho$ . [1]

## Introduction

---

already been extensively explored and tend to be rather incremental. A third approach is that of controlling not only the microstructure but also the architecture [4]. By doing so, a new class of engineering materials has emerged: the architected cellular materials. Historically, this was first achieved by the production of stochastic foams with random architecture [5]. Later, regular simple three dimensional (3D) architectures were developed such as honeycombs in sandwich panels. Recently, true 3D cellular architectures, including regular foams and micro-lattices, provide tailored materials with unique properties [6].

Driven by the constant demand for stronger and yet lighter materials, architected cellular materials find applications in various engineering fields including lightweight design, energy absorption, metamaterials, acoustic or thermal management or any combinations of these. The growing interest in multiscale cellular materials was supported by the appearance of new manufacturing capabilities, referred to as additive manufacturing or 3D printing technologies which permit the fabrication of complex 3D geometries with sub-micron resolution.

Micro-architected cellular materials were first made of polymer [7, 8] due to processing constraints. Shortly after that, the micro-architectures were coated with ceramic or oxides via sol-gel [9, 10] or atomic layer deposition [11, 12] processes. Finally, the microarchitectures were metallized [13, 14]. This technique provides an efficient way to produce coatings, foils or even complex 3D shapes with high uniformity. Electrodeposition of metals can also be used to produce new materials in which the microstructure is finely tuned with the plating parameters. Although electrodeposition is a well-established technique, metal electroforming of cellular micro-materials is demanding. Specific challenges include the electrodeposition onto non-conductive surfaces, adequate surface preparation, appropriate throwing power for electrolyte infiltration into submicron features or proper process optimization to control the microstructure.

Current design capabilities of 3D cellular materials, combined with electrochemical deposition of metals, will be used to produce low-density metal structures with high strength and/or stiffness. This process combination will generate structures with enhanced mechanical properties that would not be normally achievable [15]. This is made possible by the combination of the three following phenomena:

- 
1. the intrinsic size effect in metals which depends on the microstructure;
  2. the extrinsic size effect in metals which depends on the external dimension;
  3. the dependence of the micro-architected geometry on deformation.

In this thesis, we explore the possibility of combining lithography techniques with electrochemical deposition in order to tailor the microstructure and the architecture to achieve light but strong materials.

### **Structure of the thesis**

The present thesis is divided into six main parts. The first chapter presents a critical literature review highlighting the current state of the art in the mechanics of 3D cellular metals. On that basis, we identify the scientific questions that need to be addressed.


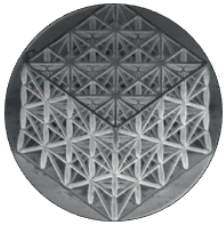
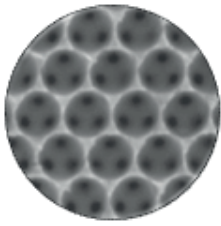
The following four chapters cover the three size effects in metals (intrinsic, extrinsic and architecture) and their interactions. In this framework, we designed three types of samples. Each sample type deals with one or multiple size effects. For clarity, Table 1 presents the three materials under investigation, starting with nanotwinned copper electrodeposits. In this case, the effect of nanoscale twins inside face-centered cubic (fcc) copper is used to demonstrate the possibility to tailor the mechanical properties by using the intrinsic size effect. We also studied the mechanical behaviour of hybrid 3D micro-architectures to show the effect of both the effect of the extrinsic size effect given the amorphous nature of the nickel-boron (NiB) coating and the effect of the architecture by designing micro-lattices. Finally, nickel inverse opals were chosen as model material because they combine three size effects. The intrinsic size effect is controlled by the grain size; the extrinsic size effect is controlled by the ligament size, while the architecture effect result from the fcc porous structure.

Chapter 6 compares the mechanical properties of the tested microstructures and micro-architectures with the literature data. The potential implications of our findings to design light-yet-strong cellular metals are discussed.

**Introduction**

---

Table 1 – Thesis overview.

			
	<b>nt-Cu</b>	<b>3D architecture</b>	<b>Ni inverse opals</b>
Material	Copper	Hybrid polymer/NiB	Nickel
Crystal structure	Crystalline with $\Sigma 3$ twin boundaries	Amorphous	Nanocrystalline to fine grained
Size effects ?			
→ Intrinsic	✓ nanoscale twins		✓ grain size
→ Extrinsic		✓ NiB thickness	✓ ligament size
→ Architecture		✓ 3D micro-lattices	✓ inverse opals
Scientific challenges	<ul style="list-style-type: none"> <li>• Grain boundary engineering</li> <li>• Effect of twin orientation</li> <li>• Comparison with conventional Hall-Petch</li> </ul>	<ul style="list-style-type: none"> <li>• Thickness effect on the ductile to brittle transition in amorphous NiB</li> <li>• Effect of the architecture on strength and buckling behaviour</li> </ul>	<ul style="list-style-type: none"> <li>• Produce highly regular porous metal foams</li> <li>• Origin of the strength: grain size vs. ligament size</li> </ul>

---

# 1 Literature review

Recent techniques allow the design and production of 3-dimensional ordered cellular materials with a submicron resolution. This emerging new class of materials demonstrates a unique combination of materials properties. The mechanical properties of cellular solids are the result of the architecture and the mechanical properties of the bulk material that it is made of. However, when the dimensions are reduced to the micrometer range, additional size effects must be considered. That is particularly true for metals, which show both intrinsic and extrinsic size effects.

This chapter will review the characteristics and mechanical properties of metallic cellular materials. The size effects in metals will be presented along with their strengthening mechanisms. Finally, the processing techniques which allow for production of 3D micro-architected metals while combining the metal size effects are described.

## 1.1 Cellular metals

The constant need to reduce manufacturing costs while minimizing the environmental impact is driving the research for novel materials with structural hierarchy for improved performances and functionalities. These materials are referred to as cellular materials. The term 'cellular material' is generally understood as any solid that is composed of a continuous solid phase (i.e. matrix) and a gaseous phase. In other words, the phrase cellular materials is applied to any solids that contain voids or pores in excess of 30% volume fraction. Cellular materials are

present in nature (e.g. bones, woods) but they can also be artificially fabricated. Polymeric cellular materials are the most common type of cellular material but even ceramics and metals can be shaped into cellular materials.

3D cellular metals are attracting considerable interest due to their many potential applications in energy harvesting, micro- and nano-porous electrodes or micro-electro-mechanical systems (MEMS). The mechanical properties of such materials are therefore a key parameter to guarantee the performance and reliability of the final device.

Taking advantage of the cellular structure, materials with unprecedented mechanical and functional properties are now possible. These unique mechanical properties stem from the structure or architecture rather than the chemistry. However, if one wants to further expand the material property space the design of efficient structure should be complemented with other strengthening strategies. The control of the microstructure is key to developing and tuning the mechanical properties.

### 1.1.1 General characteristics

The growing interest in cellular metals was supported by the appearance of new manufacturing capabilities, which permit the fabrication of complex 3-dimensional geometry down to the nanometer scale. Some remarkable features of cellular material include high stiffness-to-weight ratios [13, 11, 16–18], negative Poisson's ratio (auxetic materials) [7, 8], negative coefficient of thermal expansion [19–21], and superior electrical conductivity, heat transfer or energy absorption [22].

Such structures are reported to exhibit high strengths and yet very low densities by combining well-engineered cellular solids and size effects at the nanometer scale resulting in structures with outstanding properties. The main route to producing cellular structures is a two-stage process: (i) manufacturing of a 3D polymeric template, and (ii) subsequent deposition of a coating. Cellular materials are traditionally divided into two categories open-cell and closed-cell structures. Open cell cellular structures include open-cell foams, lattices and inverse opals, whereas closed-cell structures include hollow-sphere packing.

Table 1.1 – Scaling laws of cellulars materials as derived by Ashby [23] for bending- and stretching-dominated structures.

	Bending-dominated	Stretching-dominated
Stiffness	$\frac{E^*}{E_s} \propto \left(\frac{\rho^*}{\rho_s}\right)^2$	$\frac{E^*}{E_s} \propto \left(\frac{\rho^*}{\rho_s}\right)$
Yielding	$\frac{\sigma_{pl}}{\sigma_s} \propto \left(\frac{\rho^*}{\rho_s}\right)^{1.5}$	$\frac{\sigma_{pl}}{\sigma_s} \propto \left(\frac{\rho^*}{\rho_s}\right)$
Elastic buckling	$\frac{\sigma_{el}}{\sigma_s} \propto \left(\frac{\rho^*}{\rho_s}\right)^2$	$\frac{\sigma_{el}}{\sigma_s} \propto \left(\frac{\rho^*}{\rho_s}\right)^2$
Fracturing	$\frac{\sigma_{cr}}{\sigma_{cr,s}} \propto \left(\frac{\rho^*}{\rho_s}\right)^{1.5}$	$\frac{\sigma_{cr}}{\sigma_{cr,s}} \propto \left(\frac{\rho^*}{\rho_s}\right)$

### 1.1.2 Properties of cellular materials

Ashby [23] developed analytical models and scaling laws for open-cell and closed cell-cellular structures. These scaling laws are given as a function of the relative density, which is the density of the structure normalized by the density of the parent material. Comparisons between the micro-architectures are then possible regardless of their design or microstructures.

We distinguish two different types of architectures depending on the deformation mechanism: bending-dominated and stretching-dominated architecture [24]. Yield strength and stiffness are related to the relative density by a power-law as described in Table 1.1. The exponent of the power-law indicates the preferred deformation mode. Bending-dominated and stretching-dominated architectures constitute upper and lower mechanical bounds because mixed-mode deformation is likely to occur.

### 1.1.3 Structure optimization

Three-dimensional cellular architectures are complex structures with many design variables such as the shape, size, volume, material, etc., which can be varied to optimize material characteristics such as stiffness, strength, displacement, volume, heat conduction.

#### Metallic foams

Hodge et al. [28] showed that the mechanical properties of stochastic metallic foams outperform Ashby’s prediction when the ligament size is below 1  $\mu\text{m}$ . An example of such metal foam is given in Figure 1.1a. They proposed the introduction of a yield strength dependent formula

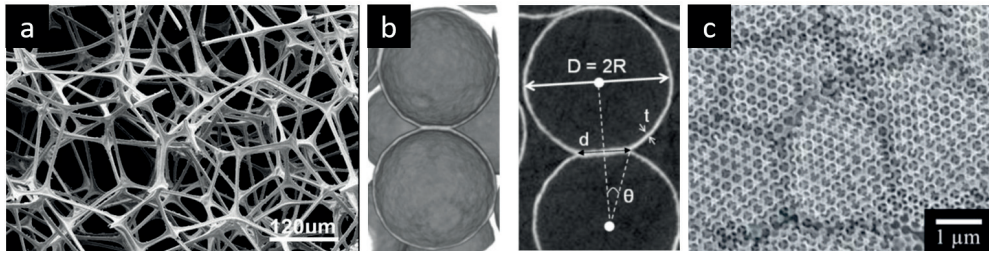


Figure 1.1 – SEM micrographs of different types of metallic foams: a) Ultralight Ni/Ag foam with random structures obtained by electroless deposition [25]; b) metallic hollow spheres foam [26]; c) Silver inverse opal obtained by electrodeposition [27].

to account for the extrinsic size effect:  $\sigma^* = C_1(\sigma_0 + \frac{k}{\sqrt{L}}) \frac{\rho_s^*}{\rho_s}^{3/2}$ , where L is the ligament size. Similarly, nanoporous metal foams with ligament size below 100 nm have shown outstanding mechanical properties, sometimes close to the theoretical strength [29–31]. For regular stacking of spheres as shown in Figure 1.1b and c, Sanders and Gibson [32] calculated the scaling laws and showed that the specific strength and stiffness are higher for fcc than body-centered cubic and for a simple cubic structure.

### Micro-lattices

Unlike ordered metallic foams where a single unit cell is repeated in all directions, micro-lattices offer an additional degree of freedom in designing complex architectures. 3D direct laser writing has promoted the development of 3D architectures at the micron scale [33]. A polymer template is fabricated and then coated. Materials used to coat the micro-lattices include crystalline metals [13, 34], amorphous metals [35] and ceramic [11, 36]. Additionally, the removal of the polymeric template is optional. The mechanical properties of micro-lattices are also compared using the scaling laws given in Table 1.1. However, metal micro-lattices offer one additional level of hierarchy: the direct control of each element within the micro-lattice. By properly designing the architecture, one can take advantage of the microstructure of the metal, the thickness of the coating and the morphology of the architecture.

In summary, 3D cellular materials present many interesting properties. However, their porous nature limits their use in load bearing applications because the mechanical properties scales with the relative density. As the porosity increases, both the yield strength and elastic modulus decreases. In this theoretical framework, the mechanical properties are assumed to be inde-



## 1.2. Combining 3D architected with size effects in metals

---

pendent of the pore size. However, when the characteristic length scale is in the micron range, the intrinsic and extrinsic size effects in metallic micro-cellular materials cannot be ignored. The size effects in regular metallic foams need to be addressed, especially when the ligament size is small enough to induce a strengthening effect. Therefore opportunities exist to explore the unique combination of size effects in micro-cellular metals. These considerations are discussed in the following section.

## 1.2 Combining 3D architected with size effects in metals

The previous section demonstrated the potential of highly regular cellular metals. In the present section, size effects in metals are reviewed.

It is well-known that the plasticity of pure metals are largely determined by the microstructure – whether through defects, interfaces or grain boundaries [37]. Grain boundary engineering is therefore a typical approach to tune the mechanical properties and take advantage of the intrinsic size-effect. More recently, it has also been found that the strength scales inversely with the external dimension of the specimen [38]. This phenomenon is referred to as the extrinsic size effect.

### 1.2.1 Intrinsic size effect

Intrinsic size effects are well-known and used by engineers and scientists to tune the mechanical properties of metals. This strengthening technique is based on using microstructural modifications to enhance the properties of metals. This includes solid solution strengthening, precipitation hardening and grain boundary engineering. Studying pure metals, we will limit our review to the understanding of grain boundary engineering known as the Hall-Petch effect [39] because it was first described by Hall [40] and Petch [41]. This relation states that the strength of a material is inversely proportional to the square root of the grain size:

$$\sigma = \sigma_0 + \frac{k}{\sqrt{d}} \quad (1.1)$$

Although numerous articles in the literature deal with this effect, the exact physical model

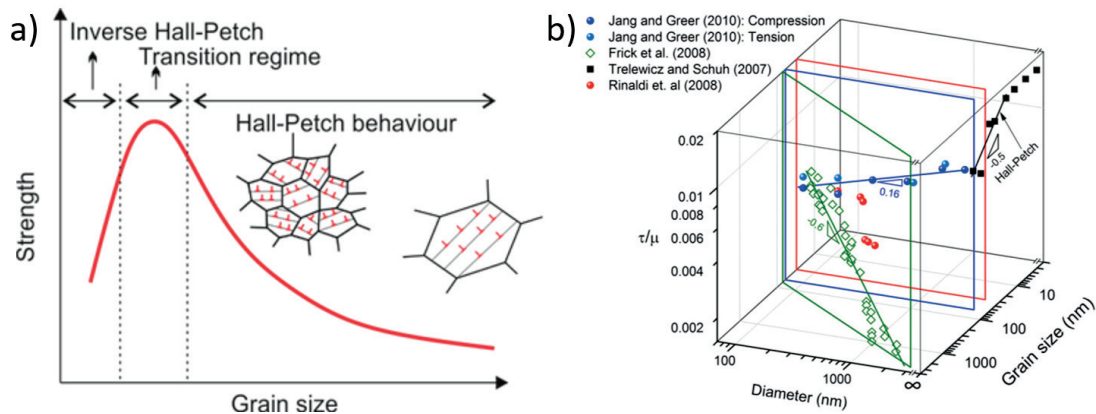


Figure 1.2 – a) Strength of polycrystalline metals as a function of the grain size, known as the Hall-Petch relation. b) Normalized shear stress as a function of the grain size and the sample diameter revealing both the intrinsic and extrinsic size effect in Ni (and Ni-4wt%W). Reproduced from Greer and De Hosson [44].

is not yet clear. To explain this effect, several types of models have been proposed such as a dislocation pile-up model, a grain boundary source model, a slip distance model and a model based on geometrically necessary dislocations. However, the most widely accepted strengthening mechanism is the dislocation pile-up model. In this model, the grain boundaries serve as barriers to dislocation motion, as shown in Figure 1.2a. The smaller the grain size, the fewer dislocations are contained inside the pile-up and therefore larger is the stress necessary to deform the metal.

Due to this behavior, the development of nanocrystalline metals has attracted a lot of attention. However, further reduction in the grain size results in a strength saturation or even softening below a critical grain size [42]. This regime is often called the inverse Hall-Petch regime.

Therefore the idea of grain boundary engineering was taken to the next level. Lu et al. [43] found that nanoscale twins in copper were even more effective in blocking dislocation motion than grain boundaries in nanocrystalline metals, while maintaining high electrical conductivity and good ductility. This type of advanced microstructure is highly desirable for an industry such as microelectronics. Up to now, grain boundary engineering was limited because the conventional processes failed to deliver Cu films with highly oriented nanoscale twins but recent progress in Cu electrodeposition provide new development routes.

### 1.2.2 Intrinsic size effects: the special case of nanoscale twins in copper

Nanocrystalline copper, in comparison to coarse grain copper, offers improved yield strength and hardness. The grain boundaries act as barriers to dislocation motion, the Hall-Petch strengthening mechanism. However, below a certain grain size a soft deformation mechanism is favored, limiting the maximum strength. In addition, other properties of interest – such as ductility, creep resistance and the electrical resistivity of nanostructured metals – decreases with grain size. One solution would be to actively block the motion of dislocations while limiting the electron scattering induced by these barriers. One defect which allows the combination of both characteristics is known as a twin boundary. A twin boundary is characterized by a defect in the stacking sequence of atomic planes (Figure 1.3a) in fcc crystals. As a result, the grains on either side of the twin boundary show a mirror symmetry with each other, making the twin boundary a high order boundary when compared to regular grain boundaries (Figure 1.3b).

Unlike nanocrystalline copper, copper electrodeposits with nanoscale twins reveal remarkable mechanical properties (Figure 1.3c) with enhanced ductility and electrical conductivity. Lu et al. first reported the mechanical properties of electrodeposited nanotwinned copper [43]. Tensile tests of ultra-fined grained copper with nanoscale twins resulted in a yield strength in excess of 1 GPa and enhanced ductility. Subsequent studies [45, 46] showed that: 1) the yield strength increases as the twin spacing is reduced in an analogous manner to Hall-Petch strengthening, 2) the ductility is inversely proportional to the twin spacing. Another important feature of nanotwinned copper (nt-Cu) is its high sensitivity to strain rate [47–49].

Several processing routes are possible to produce growth twins. However, the electrochemical route is the most promising both in terms of potential fine control of the twin morphology and distribution and in terms of potential applications. The fabrication of copper electrodeposits with highly-oriented nanoscale twins enables the discrimination of the strengthening effect of twin boundaries and grain boundaries. Values of strength as high as 2.43 GPa were achieved in micropillars compression tests with a twin spacing of 0.6nm and in the absence of other microstructural features [50].

The effect of the twin orientation with respect to the loading direction on the strength of nt-Cu

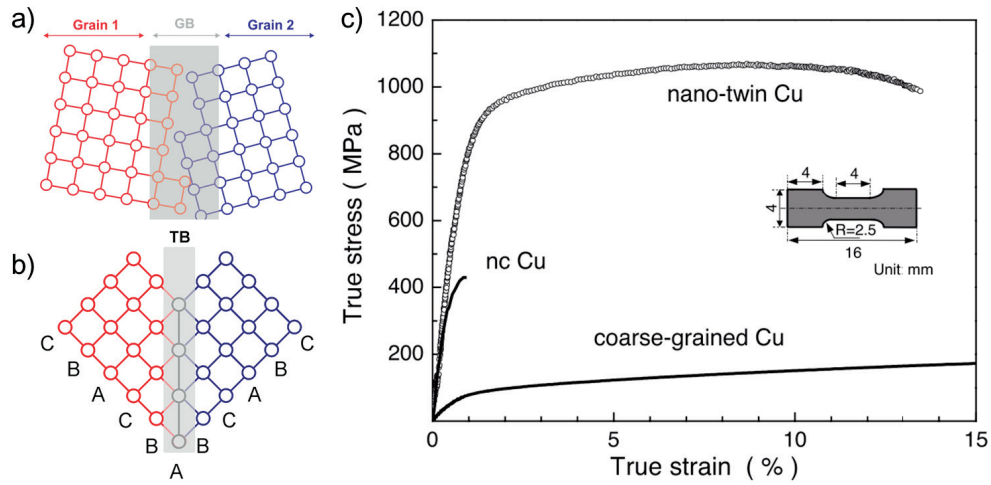


Figure 1.3 – Schematic illustration of two types of interfaces: a) a typical grain boundary (GB) and b) a coherent twin boundary (TB). c) Comparison of the mechanical properties of copper with nanoscale twins, nanocrystalline and coarse-grained microstructure [43].

is also under investigation [45, 50, 51]. Experimentally, few papers study the mechanical properties of copper as a function of the twin orientation. However, Jang et al. [50] demonstrated a 30% reduction in yield strength when the twins are tilted by  $18^\circ$  with respect to the loading direction. You et al. [52] observed three distinct deformation mechanisms as a function of the loading directions, which are responsible for the strong anisotropy. When the nanoscale twins are aligned with the loading direction, the motion of threading dislocations is confined within the twin lamella. When the twins are perpendicular to the loading direction, dislocation pile-ups against the twin boundaries dominate. Twin boundary migration occurs for tilted twins. These results, supported by atomistic simulations, indicate that the dramatic change in strength with twin orientation is driven by different deformation mechanisms.

The literature review on copper with nanoscale twins outlines the importance of the intrinsic size effect when studying advanced microstructures. However, detailed mechanisms of crystal plasticity in highly-oriented twinned copper as a function of twin spacing and orientation need to be addressed.

One should also mention that copper films with highly-oriented nanoscale twins can be produced by physical vapour deposition (PVD). However PVD processing, unlike electrodeposition, is a line-of-sight deposition technique. Therefore, only electrodeposition offers the

## 1.2. Combining 3D architected with size effects in metals

---

opportunity to combine the deposition of nanotwinned structures with complex 3D geometries. That is why the fabrication of nanotwinned copper by electrodeposition is preferred in this thesis framework.

### 1.2.3 Extrinsic size effect

Complementary to microstructural effects, numerous researchers have shown that the extrinsic size effect also influences the mechanical properties of single crystal metals [53]. In particular, as the dimension of the sample is reduced, the yield strength increases due to a change in dimensional constraint restricting the nucleation and glide of dislocations as illustrated in Figure 1.2b. In extreme cases this constraint can also lead to changes in the deformation mechanism. This effect was first observed in thin-film technology. A similar size effect was later observed in nano-laminates [54] and micropillars [55] with sub-micron length scales. Several models have been proposed to explain the strengthening mechanism. These include the confinement of dislocations within the coating thickness [56] or their interaction with the free surfaces, which leads to dislocation starvation [57]. Higher loads are then necessary to plastically deform the sample by nucleating new dislocations.

The origins of size effects in metals are strongly dependent on the atomic structure: whether it is a single-crystal, a polycrystalline or even an amorphous film. In amorphous metals, plasticity occurs through shear transformation zones rather than dislocation-based mechanisms [58]. As a result, bulk amorphous metals show superior mechanical properties but fail macroscopically in a brittle manner. However, when the specimen volume is reduced, deformation by shear banding is no longer possible and local shear processes dominate, resulting in homogeneous flow [59]. Therefore, the brittle to ductile transition observed in amorphous metals is the result of an extrinsic size effect.

### 1.2.4 Size effects interaction

Interaction of both intrinsic and extrinsic effects is non-trivial. For instance, one could think that reducing the grain size together with the thickness would result in stronger samples than just playing with one size effect. However, Greer et al. showed that in the case of

nanocrystalline micropillars a reduction of the pillar diameter decreases the yield strength. Thus, there is a "smaller is weaker" effect for nanocrystalline metals. The reason is that the stress is accommodated by grain boundary sliding and rotating due to free surfaces instead of dislocation-based processes. This effect is unclear because for pillars above  $>1\mu\text{m}$ , opposite effects have been observed. It turns out that the boundary conditions drastically affect the mechanical response.

At low dimensions or grain sizes the strength increase with the characteristic feature size. The consequence of this length scale effect opens the way for multi-functional, light and yet strong porous metals. Few studies have explored the relation between the size effects in the case of 3D cellular metals. The synthesis of such cellular metals is now possible with modern microfabrication techniques, as described in the following section.

### 1.3 Processes controlling the size effects in metals

The development of new manufacturing capabilities, referred to as additive manufacturing or 3D printing technologies, permits the fabrication of complex 3-dimensional hierarchical structures. In this section, we review the top-down and bottom-up methods required to fabricate these cellular metals. The processes are based on lithography techniques and electroplating.

#### 1.3.1 Electrochemical deposition of metals

Electrochemical deposition processes provide the possibility to control the microstructure like any other deposition method. Researchers reported microstructure varying from large grains to nanocrystalline grains, and even amorphous films. Metal electroplating is a versatile processing technique for plating metal films onto conductive, semi-conducting and even insulating substrates. The basic concept of metal electrodeposition consists in an oxidation and reduction (redox) reaction of metallic ions dissolved in an aqueous solution onto the surface of a substrate. This electrochemical reaction involves a charge transfer between the

metal ions  $M^{z+}$ :



where  $z$  is the number of electrons exchanged. We can distinguish two types of metal plating processes according to the origin of the electrons. In metal electrodeposition, the electrons are supplied by an external source of current. If no external power supply is necessary to supply the electrons, the process is referred to as electroless deposition. The electrons are provided by a redox reaction in the electrolyte or at the substrate surface.

#### **Electrodeposition of metals**

The metal film results from the reduction of metallic ions at the cathode by an external current source, as stated in equation 1.2. The current is flowing through the cathode (substrate) and a counter electrode. A third electrode can be added for precise electrochemical measurements or potentiostatic deposition. The microstructure is controlled by the plating parameters and the electrolyte composition. Additives can be added to alter the electrochemical deposition mechanism and thus change the microstructure and deposit uniformity. Those are organic compounds that adsorb at the cathode surface. For example, brighteners are known to induce grain refinement and produce nanocrystalline microstructures. More advanced microstructures such as nanotwins can be obtained by applying the right combination of additives, plating parameters and hydrodynamic conditions.

#### **Electroless deposition**

The deposition of a metal coating can also be performed without the use of an external source of electric current, that is electroless deposition or electroless plating. The source of electrons is provided by a chemical reaction within the electrolyte. This process can be performed on both conductive and non-conductive substrate, if the substrate surface is suitably treated before deposition. There are two main types of electrodeposition processes for metals:

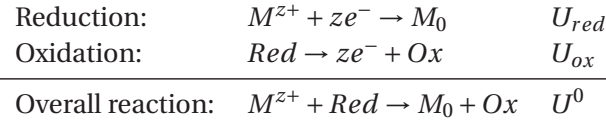
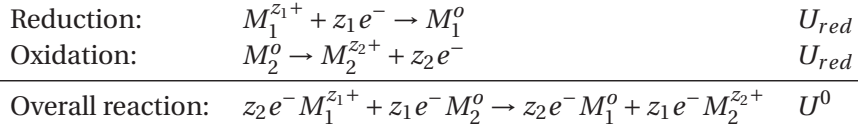
1. displacement (immersion) deposition
2. autocatalytic deposition

## Chapter 1. Literature review

---

In the first process the electrons are provided by the substrate, while they come from the oxidation of a reducing agent in the latter process. Displacement reaction is a self-limiting process. As soon as the substrate is completely covered, the substrate dissolution is no longer possible and the deposition reaction stops.

Electroless deposition offers another important advantage which is particularly useful for the fabrication of cellular metals; it can be performed on non conductive substrates (e.g. glass, ceramics, polymer), provided that an adequate surface preparation is performed. This generally include the following steps: surface activation, functionalization and catalyzation. The electroless deposition of metals on non-conductive substrates has been reported in the interconnects industry [60] and on 3D polymeric micro-architectures [35].



### 1.3.2 Lithography techniques

Additive manufacturing (AM), also known as 3D printing, refers to the processing techniques that produce complex 3D geometries using a layer-by-layer approach. Unlike conventional manufacturing technologies that removes material from a larger block, 3D printing works by addition of material. As a result, the design of complex forms can be generated with new properties and functionalities.

#### Direct 3D metal printing

The most common methods to produce 3D metal structures are based on local melting of a metallic powder with a laser beam. This technique includes selective laser melting (SLM) and direct metal laser melting (DLM). While these methods demonstrated their capability to generate 3D metallic structures, their resolution is limited and they usually require post-



### 1.3. Processes controlling the size effects in metals

---

processing steps. Higher resolution, down to the nanometer scale, can be achieved with an electron or ion beam, such as electron beam melting (EBM), focused electron beam induced deposition (FEBID) and focused ion beam (FIB) assisted deposition. All these methods operate in high vacuum and require complex gas injection systems, which means high costs and low fabrication efficiency.

Recently, the deposition of 3D metal structures via electrochemical additive manufacturing (ECAM) has emerged [61]. Here, 3D metal structures are produced through the localized electrochemical reduction of metals ions from an electrolyte onto a conductive substrate. The ECAM techniques can be subdivided into two categories: a meniscus confined electrode technique and a localized electrochemical deposition technique. In the former technique, the electrochemical reaction occurs inside the electrolyte meniscus formed between the substrate surface and a micropipette containing a counter and/or a reference electrode. In the latter technique, a microelectrode, acting as the anode, is immersed inside the plating bath and is brought close to the surface so that a confined electrical field is produced, resulting in a localized metal deposition. Scanning either the micropipette or the microelectrode with a positioning stage over the conductive surface enables the fabrication of arbitrarily-shaped structures. Those electrochemical techniques, albeit promising, require complicated setups and need further development to produce mechanically relevant metal structures with fine control over the microstructure.

Another approach for the fabrication of 3D metal structures is based on the combination of a lithography technique and electrodeposition. Both techniques are well-established, with the fabrication of a polymer structure using a lithography technique, which serves as template for the electrochemical deposition of a metal. The polymer template can be structured on a conductive substrate or not, depending on the subsequent electrochemical deposition. Within the scope of the present thesis, we explore various lithography techniques for producing cellular structures with different hierarchical structures and complexities. The lithography techniques are described in the following sections.

### Colloidal lithography

Colloidal lithography is a lithography technique, also known as soft or natural lithography, which relies on a bottom-up approach in which 2D and 3D periodic arrays of microspheres are self-assembled into nanostructured colloidal crystals. The periodic colloidal crystals can be then used as templates for the formation of well-ordered porous metal structures. Compared to the photolithography techniques, this technique presents the advantages of being simple, cost-effective and applicable to large surface areas.

The microspheres, usually monodisperse silica or polystyrene microspheres, can be deposited by spin coating [62], Langmuir-Blodgett technique [63], capillary force assisted vertical deposition [64], gravity sedimentation [65] and electrophoresis [66]. The first two methods are often used for monolayer colloidal crystal formation, even though multilayer crystals are achievable by repeating the process. The other methods are suitable for forming multilayer colloidal crystals with a volume fraction of  $\sim 74\%$ .

Previous work has demonstrated the possibility to perform electrodeposition of metals and metal oxides inside colloidal crystals of spheres with a  $\sim 26\%$  volume fraction of void space. The application of light weight structural materials with low density due to engineered porosity and high strength due to grain size engineering may be even more significant. The dependence of the mechanical behavior of materials on various aspects of porosity such as size, shape and connectivity have been studied extensively, but the models are based on assumptions of a random porous structure. In addition, external (sample size) and internal (microstructure) size effects of non-porous materials have generally been studied using small individual test samples or nanocrystalline material. Therefore, an ordered porous structure with well-defined ligament and well-defined microstructure within the ligaments would allow for easier engineering of ultralight, high strength porous materials.

### UV-LiGA lithography

The UV-LiGA technology is a microfabrication technique for metallic micro-components combining both photolithography and electrodeposition and yielding high and ultra high aspect ratio structures. The term LiGA is an acronym in German for Lithographie, Galvanoformung,

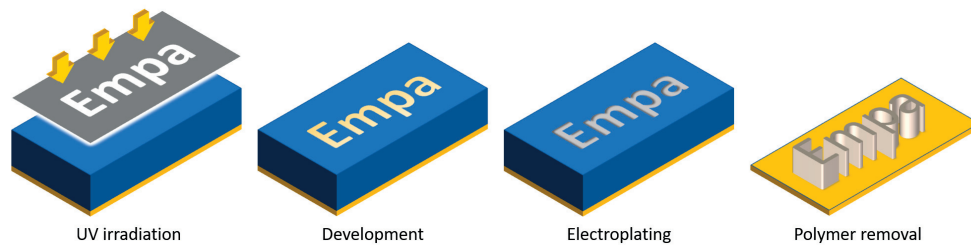


Figure 1.4 – The UV-LiGA fabrication process consists of UV irradiation, development, electroplating and resist stripping.

Abformung which means lithography, electroplating and moulding, respectively.

During LiGA processing, a photoresist is exposed to a radiation source through a mask to produce high aspect ratio structures, as illustrated in Figure 1.4. The resist is then developed and polymer molds are obtained. The mold cavities are filled by metal electroplating, which yield metallic components after the template removal by wet or dry etching. Originally developed using a deep X-Ray source, the LiGA process was then adapted using an UV light, and was therefore called UV-LiGA. The X-ray LiGA technology offers higher aspect ratio (100:1) and better quality but requires a costly synchrotron source for deep X-rays. An alternative to this issue was to apply the same principle with a UV-source instead of the X-rays [67]. High aspect ratio structures (20:1) are also achievable with higher throughput and considerably lower costs. This has made this technology attractive for various applications like MEMS and NEMS devices, sensors, actuators and micro-parts.

Deposition into high aspect ratio structures generates specific issues and challenges to take into consideration when performing micro-electroplating of 3D structures [68]. In particular, a non-uniform plating profile is observed (Figure 1.5a). The major factors influencing uniformity are: the current distribution (Figure 1.5b) and mass transfer limitations (Figure 1.5c). The current distribution depends on the geometry of lithographic features. Careful design of the anodes and cathodes is the main solution to minimize or suppress this shortcoming. Given the small size and high aspect ratio of lithographic features, the concentration of metal ions may vary with the position inside the feature. If this is the case, the reaction is said to be mass transport limited. To prevent the local depletion of metal cations, one solution consists of depositing under pulse plating conditions. If as-plated uniformity is the objective,

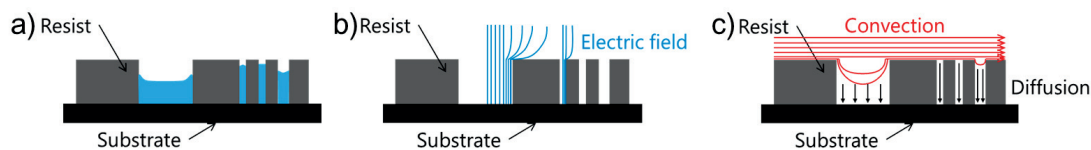


Figure 1.5 – Challenges of electrochemical deposition inside UV-LiGA lithographic features. These challenges result in a) non uniform deposition due to b) non uniform electric field and c) mass transport limited reaction.

then electroactive organic species, called additives, are added to the electrolyte to modulate the deposition rate depending on the deposition location. One important example of this approach is the damascene process for copper interconnects [69, 70].

### Two-photon lithography

Most 3D printing techniques of polymer structures rely on the principle of photopolymerization. During photopolymerization, a photoreactive resin undergoes a light-induced polymerization reaction, which converts a liquid resin into a solid resin. Unlike conventional photolithography methods like stereolithography, two-photon lithography differs by the possibility to write feature sizes below the diffraction limit (i.e. well below  $1\ \mu\text{m}$ ) [71, 72].

This process takes advantage of a nonlinear optical phenomenon called two photon absorption and of the high photon density provided by a femtosecond laser (see Figure 1.6a). During two photon absorption, a molecule simultaneously absorbs two photons that induce an electronic transition from a ground state to an excited state inaccessible by single photon absorption. The two photon absorption triggers in turn the local photopolymerization. Given that the probability of two photon absorption depends on the square of the light intensity, the photopolymerization is confined within the focus of the laser beam, as shown in Figure 1.6b. Thus, the interaction volume (or voxel) is very small, on the order of 100 nm. It is therefore possible to write true 3D micro-structures directly inside the resin, instead of using a layer-by-layer approach.

Two photon polymerization microfabrication has been successfully applied to produce a variety of 3D structures with intricate features and a sub-micron resolution that would not be possible with another technique. Current research applications include photonics, micro-

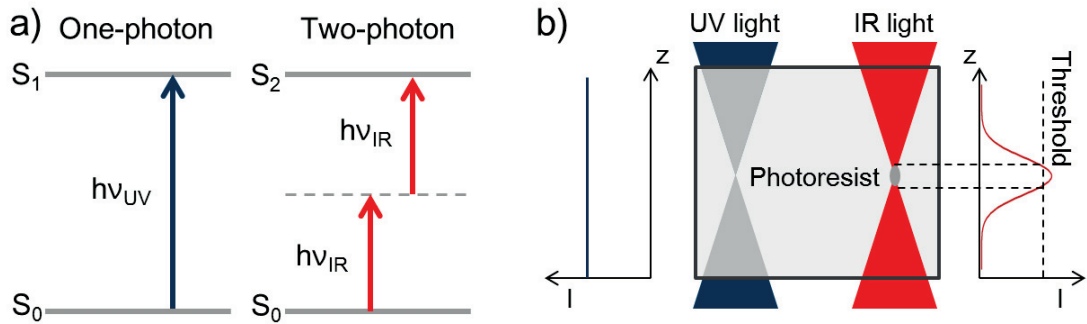


Figure 1.6 – Comparison between single photon polymerization and two photon polymerization. a) Schematic of energy levels between a ground state  $S_0$  and the excited states  $S_1$  and  $S_2$ . In two photon absorption, there exist an intermediate virtual state. b) Polymerized volume of photosensitive material for single and two photon absorption.

optics, microfluidics, biology, MEMS and metamaterials. Made of polymer, these microstructures can be used as template for ceramic or metal deposition to produce hybrid microarchitectures. The micromechanics of these structures is still at its inception due to the many technical challenges to produce, metallize, characterize and test them.

## 1.4 Summary of the literature

The literature review outlined the current development of new advanced cellular metals with improved mechanical properties and functionalities relying on the combination of tailored microstructure and designed cellular structure at the micrometer length scale. However, further investigation of the microstructure-architecture-mechanical properties relationships of architected metals is needed.

The mechanical properties of 3D cellular metals depend on the mechanical properties of the parent material(s), their relative density, the size effects and the morphology. With the emergence of novel lithographic techniques, the manufacturing of 3D cellular solids at a micrometer length scale with a submicron resolution was made possible. Polymers, ceramics, oxides or metals have been used to fabricate architected cellular solids. However the size effects in metals makes them the preferred materials for studying the mechanical properties at this length scale.

Electrochemical deposition of metals in or onto a polymeric template is rarely used to produce 3D cellular structures and is mostly restricted to commercial baths. However, electrodeposition offers many opportunities. Modern electroplating techniques have demonstrated their relevance in producing highly conformal coatings with high aspect ratios on a variety of substrates. The grain size can be adjusted from coarse-grained to nanocrystalline structure and even amorphous microstructure. The metal thickness is also finely controlled in the nanometer range by the plating parameters. These advantages could be combined with self-assembled templates or even tailored 3D micro-lattices to prepare complex nanomaterials with novel properties and further explore the role of size effects.

### 1.5 Goals of research

The present thesis focuses on investigating the mechanical properties and failure mechanisms of advanced microstructures, metallic regular foams and micro-lattices under uniaxial compression loading. This approach intends to examine the various size effects by incrementally increasing sample complexity starting from the microstructure only, through 3D architected structures with a simple unit cell, to complex hybrid 3D micro-architectures. The goals of this thesis include:

- Investigate the effect of advanced microstructure of pure metals for enhanced mechanical and functional properties by electrochemical deposition. We aim to produce electrodeposited copper films with nanoscale twins. The mechanical behavior including the strength, strain rate sensitivity and activation volume of these films will be explained in relation with the preferred twin orientation.
- Understand the synthesis of controlled metallic architectures by means of electrochemical deposition inside colloidal templates and onto 3D polymeric templates. Specific challenges arise from this unique process combination. First a high throwing power is necessary to plate inside cavities. To achieve metal coatings with homogeneous thickness, composition and microstructure, a fine control of the plating conditions is required. Indeed, the coating thickness and microstructure are affected by the non-uniform electric field, due to the complex shape of the cathode whereas the composition

may vary due to local ion depletion inside submicron features.

- Examine the mechanical properties and failure mechanisms under uniaxial loading of two types of regular metallic microporous foams and metallic micro-lattice structures, both experimentally and analytically.
- Relate the mechanical properties to the design parameters (porosity, ligament size, coating thickness) on one hand and to the microstructure on the other hand. The goal is to quantify the dominant effects between intrinsic and extrinsic size effect and explore their interactions.
- Investigate the optimum combination of architecture and microstructure for improving and/or tailoring mechanical properties of complex metallic cellular micro-architectures. Ultimately, these results would provide insights and guidelines to expand the material property space.





## 2 Materials and Methods

The present chapter describes the experimental techniques that were used to synthesize, test and characterize the metallic micro-architectures. The first section covers the lithography techniques employed to create the polymer templates for the 3D micro-architected metals. The second section deals with the electrochemical deposition of nickel and copper into the polymeric templates with tailored microstructures. Finally, the characterization methods for the microstructure and the mechanical properties are presented in section 2.3 and 2.4, respectively.

### 2.1 Lithography techniques

#### 2.1.1 UV-LiGA lithography

In this thesis, the UV-LiGA technique was employed to produce polymeric micro-structures that will be later used as templates to produce metallic micropillars of various shapes and aspect ratios by electroplating. The UV-LiGA process is conducted according to the following experimental procedure:

1. The polymeric micro-structures were deposited onto a Au-plated silicon wafer. The Si wafer was prepared by depositing a 5 nm thick layer of chromium followed by a 100 nm thick layer of gold using an electron beam evaporator (Alliance-Concept EVA 760). The chromium layer ensures a good adhesion between the Si wafer and the gold layer, and

the Au provides the conductive substrate that is required for subsequent electrochemical deposition.

2. Before coating the substrate with the resist, the substrate is heated on a hot plate at 160°C for 10 minutes to dehydrate the surface, which in turn improves the adhesion of the resist coating. The resist, an epoxy-based SU-8 photopolymer, is spin-coated onto the substrate surface using a Sawatec LSM-200 coater at a rotation speed of 2310 RPM for 40 seconds. The process parameters were selected to reach a uniform thickness of 80  $\mu\text{m}$ . Spincoating is followed by a softbake at 120°C for 30 minutes on a hot plate. The softbake step reduces the amount of residual organic solvent present in the resist film. It also hardens the film and improves its adhesion.
3. The resist is exposed with a maskless aligner MLA-150 from Heildeberg Instruments using a 375 nm laser with a spot size of 1  $\mu\text{m}$ . This exposure tool was preferred over conventional illumination through a Cr mask because this system provides an easy and flexible way to write the designs on the wafer. After exposure, a post-exposure bake is performed at 90°C for 60 minutes in order to complete the photoreaction initiated during exposure.
4. The development step consists of dissolving the unexposed SU-8 with propylene-glycol-methyl-ether-acetate (PGMA) for 3 minutes. This operation is repeated twice. The SU-8 micro-structures are then rinsed with IPA for 1 minute and dried under a nitrogen flow.
5. The resist structures can now be filled with metal by electroplating. Details of the electrodeposition procedure are given in section 2.2.
6. The polymeric template is finally removed by reactive ion etching (RIE) to make free-standing metallic micro-structures. The RIE process was carried out on a Muegge instrument at a power of 900 W power for 25 minutes. The other process parameters are: chamber pressure of 450 mT, gas flow rate of 1200 sccm  $O_2$  and 15 sccm  $CF_4$  and 60°C stage temperature.

### 2.1.2 Colloidal crystal templating

#### Self-assembly of colloidal PS templates

The PS templates were assembled by sedimentation method which consists of sedimenting a colloidal solution containing 0.25 to 1wt% monodisperse polystyrene (PS) spheres (diameter ranging from 500 nm to 4.5  $\mu\text{m}$ ). The deposition process proceeds by the action of gravity and solvent evaporation [64, 9, 73]. A clean gold-coated silicon wafer substrate was settled horizontally into the solution of PS spheres and then placed into an oven at 60°C until complete evaporation of the solvent (Figure 2.1). Driven by gravity and capillary forces, the PS spheres self-assembled into colloidal crystals with a preferred fcc structure [74]. Due to the light interaction within the PS templates, the samples appear opalescent with colors varying with the angle of observation. This is the reason why the structures that are made by filling the gaps between the spheres are sometimes referred to as inverse opals. We will use this terminology in this document.

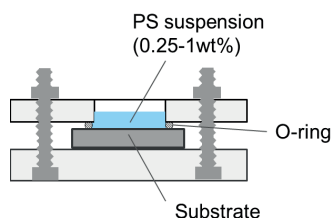


Figure 2.1 – Setup for colloidal crystal templating.

#### Annealing of the colloidal crystal

After the formation of the crystal templates, an additional annealing step was performed. The PS templates are annealed at 96°C (temperature below the glass transition temperature –  $T_g \approx 100^\circ\text{C}$ ). The annealing time depends on the PS sphere diameter: 20 min for 500 nm and 1h for 2.56  $\mu\text{m}$  PS spheres. The increase in surface of contact between the spheres during annealing stabilizes the colloidal structure for subsequent electrodeposition.

### Dual templating with colloidal crystal

The dual templating technique was used to produce porous micropillars of various shapes for mechanical characterization. This technique combines two lithography methods. First, UV-LiGA molds are fabricated to achieve the desired pillar shape, as described in Section 2.1.1. Then, the colloidal templating method presented above can be performed inside a UV-LiGA template. As a result, colloidal crystal templates in the shape of pillar are obtained.

### 2.1.3 2 photon lithography

The polymer micro-architectures were produced using two photon laser lithography on a 3D-DLW system Photonic Professional (Nanoscribe). The laser lithography was operated in the dip-in mode, *i.e.* the microscope lens is directly immersed inside the liquid photoresist (Figure 2.2). The IP-dip photoresist (Nanoscribe) was used.

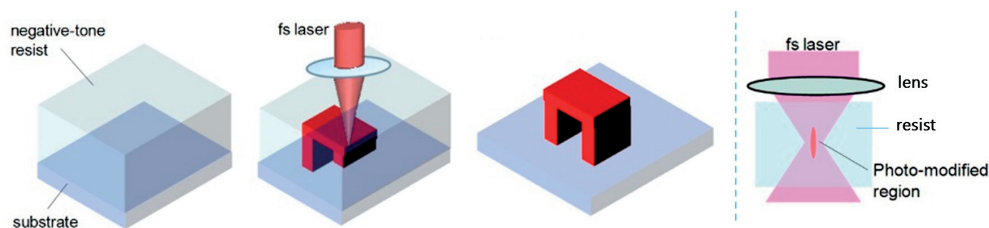


Figure 2.2 – Polymer template fabrication with 3D laser lithography. Adapted from [75]

The micro-architectures under investigation in this thesis were developed and provided by Bauer et al. [11]. Five microarchitectures were considered: 4 micro-lattices and 1 honeycomb structure (Figure 2.3), which are representative of different structural architecture. The polymeric structures were printed on a glass substrate. On each glass substrate, the design A and the designs B, C, D and E are replicated 4 and 3 times respectively. Structures A, B and C are microlattices based on a common cubic unit cell. They only differ by the number of structural reinforcing elements. Structure D is a microlattice with a hexagonal unit cell. The last geometry (Structure E) is very distinctive from the previous ones owing to its honeycomb structure in which the load is supported by thin-wall elements instead of lattice elements.

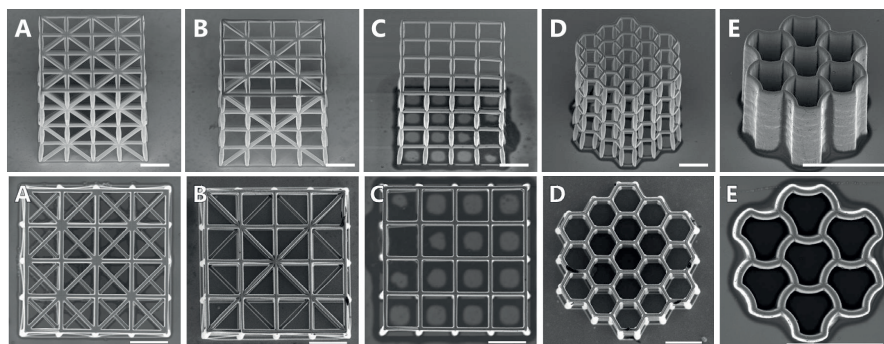


Figure 2.3 – Tilted and top view SEM images of microcellular architectures after NiB metallization. The scale bar in all the images is 10  $\mu\text{m}$ .

## 2.2 Metal electrodeposition

### 2.2.1 Copper with nanoscale twins

The composition of the copper electrolyte is given in Table 2.1. Copper sulfate provides the Cu ions for deposition while sulfuric acid has two roles. First, it facilitates the dissolution of the copper salt and second it increases the electrolyte conductivity. The other three organic compounds present in the bath are conventional bath additives.

Table 2.1 – Bath composition and parameters for the electrodeposition of copper with nanoscale twins.

Compound	Formula	Concentration	Parameters
Copper (II) sulfate	$\text{CuSO}_4$	$0.26 \text{ mol.L}^{-1}$	T=20°C
Sulfuric acid	$\text{H}_2\text{SO}_4$	$2 \text{ mol.L}^{-1}$	
PEG	$\text{H}(\text{OCH}_2\text{CH}_2)_n\text{OH}$	$100 \text{ mg.L}^{-1}$	
Chlorine ions	HCl	$50 \text{ mg.L}^{-1}$	
MPS	$\text{HSCH}_2\text{CH}_2\text{CH}_2\text{SO}_3\text{Na}$	$10 \text{ mg.L}^{-1}$	

The electrodeposition was performed on gold-coated silicon wafers using a three-electrode cell setup at room temperature. A saturated calomel electrode (SCE) was used as a reference electrode and a platinized titanium mesh was used as a counter electrode. Prior to deposition, the substrates were cleaned in a Piranha solution, rinsed in ultra-pure water and dried under air. The copper deposition was carried out under pulse potential conditions using a potentiostat (Autolab PGSTAT 30, Metrohm).

### 2.2.2 Nanocrystalline nickel

Nanocrystalline nickel samples were produced by electrodeposition in a two-electrode cell setup in which the cathode and the anode are the substrate and Ni-pellets in a titanium coated basket, respectively. The composition of the nickel sulfamate bath is given in Table 2.2. The pH of the solution was adjusted to 3.5 by addition of sulfamic acid. The role of saccharin is to act as a grain refinement agent [76] so that the nickel sulfamate bath produces bright low-stress deposits with a nanocrystalline microstructure. Electrodeposition was carried out galvanostatically at  $-80 \text{ mA}\cdot\text{cm}^{-2}$  at  $60^\circ\text{C}$  by employing a computer-aided potentiostat system (PGSTAT 30, Autolab). After deposition, the samples were rinsed in deionized water and dried under argon flow.

Table 2.2 – Bath composition and parameters for the electrodeposition of nanocrystalline nickel.

Compound	Formula	Concentration [g/L]	Parameters
Nickel sulfamate	$\text{Ni}(\text{SO}_3\text{NH}_2)_2\cdot 6\text{H}_2\text{O}$	450	pH=3.5
Nickel chloride	$\text{NiCl}_2\cdot 6\text{H}_2\text{O}$	30	T=60°C
Boric acid	$\text{H}_3\text{BO}_3$	20	
Saccharin	$\text{C}_7\text{H}_5\text{NO}_3\text{S}$	2.5	
SDS	$\text{CH}_3(\text{CH}_2)_{11}\text{SO}_4\text{Na}$	0.1	

### 2.2.3 Electroless Nickel-Boron

NiB plating was used to coat polymer micro-architectures with a thin conformal layer of metal. The schematic in Figure 2.4 breaks down the metallization process into four steps: activation, functionalization, catalyzation and deposition.

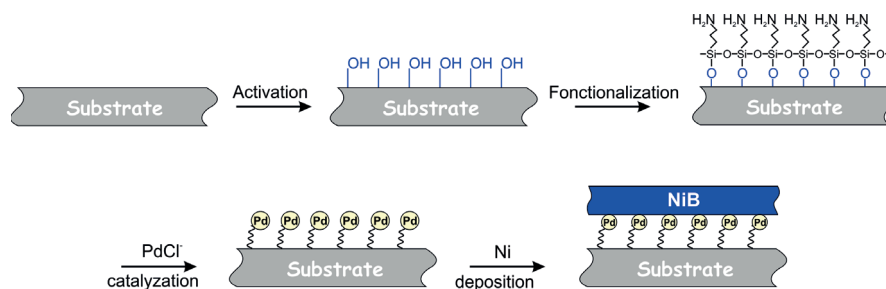


Figure 2.4 – Undeformed (left) and deformed (right) micropillar with geometrical parameters.

### Surface preparation of non-conductive substrate

Electroless deposition on non electrically conductive substrates requires a thorough surface preparation to achieve a uniform and adherent coating. The surface activation step is intended to create hydroxyl groups on the polymer surface by exposing the surface to oxygen plasma for 1 minute at a power of 250W. The surface can now be functionalized. The sample is immersed for 10 minutes at 60°C into 10 w/v% (3-aminopropyl)triethoxysilane (APTES) in isopropanol solution. The freshly formed -OH groups bind to the 3-Aminopropyltriethoxysilane (APTES) molecules and thus form a self-assembled monolayer at the polymer surface of silane compounds terminated by an amino group. After that treatment, the sample is rinsed with isopropanol. The catalyzation is accomplished by immersing the sample for 1 minute in an aqueous solution of Pd<sup>2+</sup> and HCl and rinsing in water. Palladium ions (Pd<sup>2+</sup>) are chemisorbed on the surface because of the strong affinity of these species towards the nitrogen contained in the positively-charged amino group [77]. The Pd-catalyzed organosilane surface modification ensures a good adhesion of the palladium catalyst for the subsequent metallization [78].

### NiB deposition on catalyzed substrate

Once the surface is adequately prepared, the metallization of the non-conductive surface can proceed via NiB electroless plating. The process leads to the deposition of a thin conformal layer of NiB on the catalyzed structures. The plating bath consisted of an aqueous solution of nickel sulphate, which is the nickel ion source, potassium citrate, which is the complexing agent and dimethyl amine borane (DMAB) as the reducing agent. It should be noted that DMAB has a dual role; it also reduces Pd<sup>2+</sup> species into the Pd(0) state [79] and these act as nucleation sites for the nickel. Detailed composition and operating conditions are given in Table 2.3. The deposition was conducted at 70°C and pH of 9 (pH is adjusted with an aqueous solution of NaOH).

Table 2.3 – Bath composition and parameters for the electroless deposition of NiB.

Compound	Formula	Concentration [mol/L]	Parameters
Nickel (II) sulfate	NiSO <sub>4</sub> .6H <sub>2</sub> O	0.1	pH=9
DMAB	(CH <sub>3</sub> ) <sub>2</sub> NH.BH <sub>3</sub>	0.05	T=70°C
Sodium citrate	HOC(COONa)(CH <sub>2</sub> COONa) <sub>2</sub> .2H <sub>2</sub> O	0.2	

### 2.3 Microstructural analysis

#### 2.3.1 Scanning and Transmission electron microscope (SEM & TEM)

A high-resolution scanning electron microscope (Hitachi S4800) was used to image the surface topography of samples, to measure film thickness and to perform image analysis to extract physical features.

The transmission electron microscope (TEM) and high resolution TEM images and the associated selected-area electron diffraction (SAED) pattern were recorded on a JEOL 2200 FX microscope operated at 200 keV.

#### 2.3.2 X-Ray Diffraction (XRD) and Reflectivity (XRR)

The crystal structure of the various metallic specimens was analyzed with X-ray diffraction (XRD) on a Bruker D8 Discover diffractometer using a monochromatic X-ray beam  $\text{CuK}\alpha$  ( $\lambda = 1.5406 \text{ \AA}$ ) in a Bragg-Brentano configuration.

The preferred crystallographic orientation of the metal films was quantified with the texture coefficient,  $TC$ . This parameter is calculated for each reflection peak ( $hkl$ ) using the following equation:

$$TC_{(hkl)} = \frac{I_{(hkl)}}{I_0(hkl)} \left[ \frac{1}{n} \sum \frac{I_{(hkl)}}{I_0(hkl)} \right]^{-1} \quad (2.1)$$

where  $I_{(hkl)}$ ,  $I_0(hkl)$  and  $n$  represent the measured intensity of the ( $hkl$ ) reflection, the powder intensity of the ( $hkl$ ) reflection, and the number of reflections, respectively. A  $TC$  value of 1 corresponds to randomly oriented crystallites, while larger values indicate a preferred crystallographic orientation in the ( $hkl$ ) direction.

The mean crystallite size was measured by applying the Scherrer equation:

$$d = \frac{K\lambda}{L \cos\theta} \quad (2.2)$$

where  $\lambda$  is the X-ray wavelength,  $\theta$  is the Bragg angle,  $L$  is the full width at half maximum of



the considered peak and  $K$  is a crystal shape factor close to unity.

X-ray reflectometry is a non-destructive technique used to determine the thickness of thin films with a high precision. The intensity of the reflected X-ray beam is monitored as the sample is scanned in a grazing incidence configuration.

### 2.3.3 Focused Ion Beam

The focused ion beam (FIB) is a characterization and microfabrication technique that uses an ion beam to image and mill materials with high resolution. The dual FIB-SEM instrument (Tescan Vela) consists of an gallium ion column coupled with a SEM instrument as shown in Figure 2.5a. The ion beam is used for sample preparation to produce cross-sections and TEM lamellae or as a micro- and nano-milling tool.

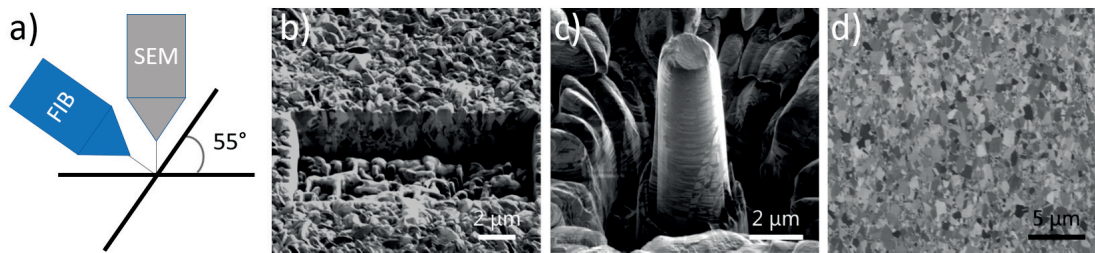


Figure 2.5 – a) Schematic of a dual FIB/SEM instrument. An example of b) a FIB cross-section, c) a micropillar obtained by FIB milling and d) an ion channeling contrast image.

FIB milling is the typical method used to produce cross-sections (Figure 2.5b) and micropillars (Figure 2.5c) for determining the micromechanical properties under uniaxial compression at small scale. However, FIB milling can induce surface damage due to Ga ion implantation potentially leading to amorphization [80]. For that reason, the micropillars were prepared following a 3 step procedure which is designed to reduce the FIB damage. First, a coarse milling is carried out to mill a large micropillar with a diameter which 3 times the final diameter. Second, a fine milling at 1000 pA is performed to decrease the sample diameter close the final one. Finally, a polishing step is performed at very low beam current (100-300 pA) to reach the final dimensions and minimize both the FIB-induced defects and the taper angle. The milling approach was also used to extract electron transparent lamellae for TEM inspection.

Microstructural observation of fine-polished metal surfaces is possible with the ion contrast

channeling capability of the dual beam instrument. Figure 2.5d shows a FIB image of cross-section of a Ni specimen. The ion channeling contrast depends on the atomic mass and crystal orientation of the sample.

### 2.4 Mechanical testing

Nanoindentation methods emerged with the necessity to probe the mechanical properties of materials at the micron scale. With this method, one can access the elastic properties such as Young's modulus ( $E$ ) or the plastic properties such as hardness ( $H$ ) or yield strength ( $\sigma_y$ ).

All the mechanical tests presented in this thesis were performed using an *in situ* Alemnis nanoindenter installed inside a Zeiss DSM96 SEM chamber, as shown in Figure 2.6. The Alemnis platform is composed of a positioning x-y stage and a 500 mN load cell that records the load as a prescribed displacement is imposed to the indenter tip using a piezo actuator. The mechanical properties are then extracted from the load-displacement data acquired during a displacement controlled test. The fact that the tests are carried out under vacuum provide data with low noise. In addition, the SEM can be used to image the deformation mechanisms during testing.

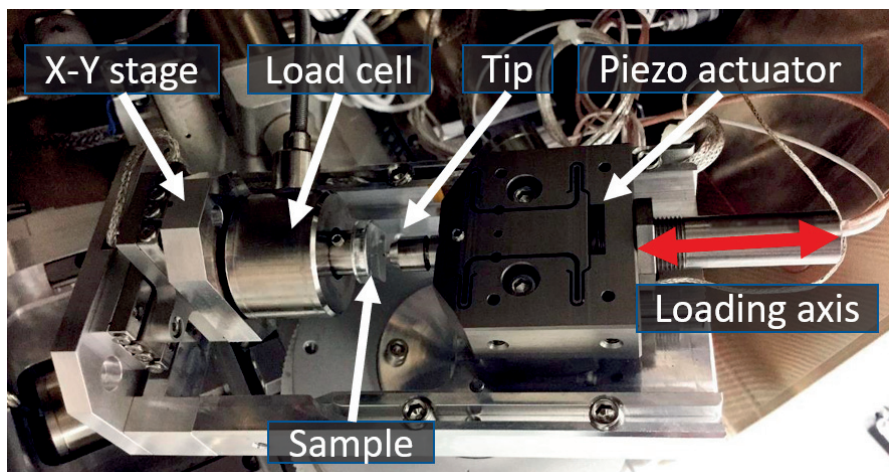


Figure 2.6 – Alemnis nanoindentation platform for compression test installed inside the SEM.

### 2.4.1 Nanoindentation

The mechanical properties of metallic films can be evaluated by nanoindentation technique using the Oliver and Pharr [81] method. The hardness and elastic modulus of the metal deposit are evaluated based on the unloading part of the load-displacement data (Figure 2.8a).

The hardness of a metallic film is calculated by dividing the maximum load  $P_{max}$  by the projected contact area  $A$ :

$$H = \frac{P_{max}}{A} \quad (2.3)$$

The contact area  $A$  is a function of the penetration depth  $h_c$  ( *i.e.*  $A = f(h_c)$  ) which depends on the indenter geometry and the elasto-plastic response of the material as shown in Figure 2.8b. The penetration depth is given by:

$$h_c = h_{max} - \epsilon \frac{P_{max}}{S} \quad (2.4)$$

where  $h_{max}$  is the maximum displacement,  $\epsilon$  is tip geometry constant ( $\epsilon=0.75$  for a Berkovich tip) and  $S$  is the contact stiffness, defined as the slope of the unloading curve.

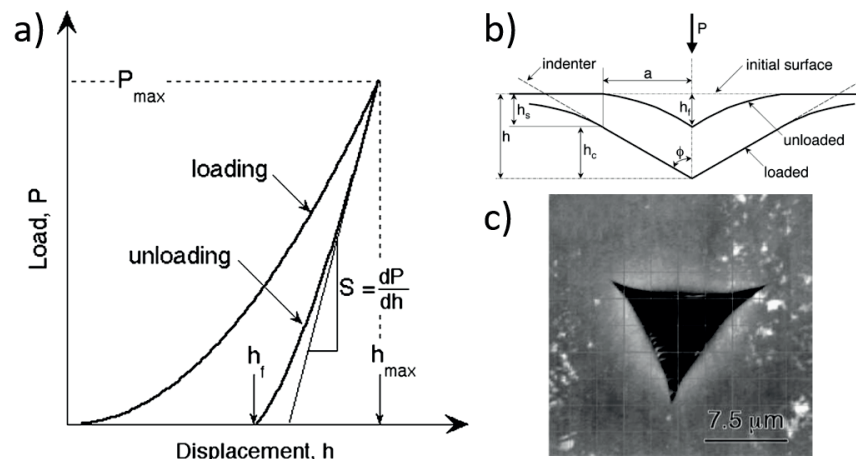


Figure 2.7 – Schematic illustration of a) indentation load-displacement data and b) contact tip geometry with important parameters. c) Residual indentation imprint made by a sharp Berkovich tip. Adapted from Oliver and Pharr [81].

The Young's modulus of the material is derived from the reduced modulus  $E_r$  which accounts

for the deformation of both the material and the indenter tip:

$$E_r = \frac{\sqrt{\pi}}{2\beta} \frac{S}{\sqrt{A}} \quad (2.5)$$

Using the Young's modulus and Poisson's ratio of the indenter,  $E_i$  and  $\nu_i$ , the Poisson's ratio of the specimen,  $\nu$ , and the reduced modulus  $E_r$  calculated in equation 2.5, the Young's modulus  $E$  of the material is:

$$\frac{1}{E_r} = \frac{1-\nu^2}{E} + \frac{1-\nu_i^2}{E_i} \quad (2.6)$$

This technique is well-suited to measure the mechanical properties of dense metals, but it is not relevant to test 3D cellular metals. In addition, little information is gained on the deformation mechanisms by this method given the complex stress state under the indent and the absence of a stress-strain curve.

### 2.4.2 Microcompression

Compression testing of micro-architectures and micropillars is an extension of the previous technique. Unlike for the nanoindentation technique, the stress-state is assumed to be uniform in micropillar compression. A flat punch is used to compress a micropillar while the load and the indenter depth are measured. From the data, the stress-strain curve of the studied material is extracted.

Figure 2.8 shows the geometry of a typical micropillar before and after deformation. The total deformation of a micropillar is measured by the indentation depth. As the pillar is compressed, not only the pillar deforms but also the substrate underneath. This is referred to as the sink-in phenomenon. A similar effect can occur at the indenter tip. A final contribution comes from the compliance of the indentation device, but this term is a known value and is removed during data acquisition. In short, the total deformation is:

$$d_{tot} = d_{pillar} + d_{indenter} + d_{substrate} \quad (2.7)$$

where  $d_{pillar}$ ,  $d_{indenter}$  and  $d_{substrate}$  are the deformation of the pillar, the indenter and

the substrate, respectively. The compliance of the substrate and the indenter are accessible through the Sneddon's correction[82]:

$$C_{Sneddon} = \frac{(1 - \nu^2)\sqrt{\pi}}{2E\sqrt{A_p}} \quad (2.8)$$

where  $\nu$  is the Poisson's ratio,  $E$  the Young's modulus and  $A$  is the projected contact area. Therefore the displacement due to the substrate and the indenter are:

$$d_{indenter} = C_{indenter}^{Sneddon} f \quad d_{substrate} = C_{substrate}^{Sneddon} f \quad (2.9)$$

where  $f$  is the measured force. Therefore the deformation of the pillar is the difference between the measured displacement and:

$$d_{pillar} = d_{measured} - F \left( \frac{1 - \nu_{sub}^2}{E_{sub}D_0} + \frac{1 - \nu_{ind}^2}{E_{ind}D_0 + 2H \tan \theta} \right) \quad (2.10)$$

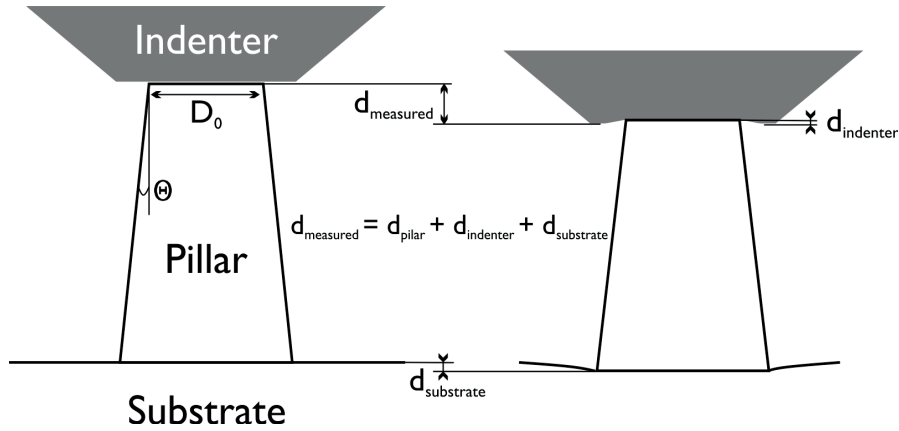


Figure 2.8 – Undeformed (left) and deformed (right) micropillar with geometrical parameters. The stress-strain curves are derived from the collected load-displacement data. The engineering stress is defined as the applied load  $P$  divided by the nominal section of the pillar and the engineering strain  $\epsilon$  is the measured pillar displacement divided by the initial length  $L_0$ :

$$\sigma = P/A_0 \quad \epsilon = d_{pillar}/L_0 \quad (2.11)$$

When the pillar is compressed by the indenter, the pillar deforms and its cross-section is no longer constant. This is characterized by an apparent softening in the stress-strain curve. If

## Chapter 2. Materials and Methods

---

the volume of the micro-pillar is assumed to be constant  $A_0P_0 = AP$ , the true stress and true strain are related to the engineering stress and strain according to:

$$\sigma_T = \sigma(1 + \varepsilon) \qquad \varepsilon_T = \ln(1 + \varepsilon) \qquad (2.12)$$

In the case of 3D cellular metals (*i.e.* regular porous inverse opals or 3D micro-architectures), the same data analysis applies except that the cross-sectional area is defined as the total projected area of the structures. The load-displacement data are expressed as engineering stress-strain curves.

### **3 Investigation of the intrinsic size effect in electrodeposited copper with nanoscale twins**

The mechanical properties of metals depend primarily on their composition and microstructure. Grain boundary engineering is therefore the main strategy to tailor the strength of pure metals. A typical approach consists of refining the grain size to increase the material's strength. This yields a Hall-Petch strengthening of the material. The grain boundaries serve as barriers to dislocation motion. However, other properties such as ductility and electrical conductivity deteriorate. As a result, the optimal grain size results from a trade-off between the optimum strength and the desired physical or electrical properties. To reconcile this contradiction, we propose investigating a method that allows us to control not only the grain size, but also the nature of the grain boundary by electrodeposition. In this chapter, we report the synthesis and mechanical properties of electrodeposited copper films with nanoscale twins for enhanced mechanical properties and good electrical conductivity.

*Parts of this chapter use materials adapted from Hasegawa et al. [83] (Elsevier Copyright) and from Mieszala et al. [84] with permission from the Royal Society of Chemistry.*

## **3.1 Introduction and motivation**

In this study, we explore the effect of nanoscale twins on the mechanical properties of electrodeposited copper films. First, the electrochemical parameters leading to controlled deposition of electrodeposited copper films with highly oriented nanoscale twins are presented and discussed. Second, we present the mechanical properties of nt-Cu as a function of the twin orientation. Based on these observations, insights in the deformations behavior and mechanisms of nt-Cu are proposed.

## **3.2 Synthesis of copper with nanoscale twins**

### **3.2.1 Experimental**

#### **Electrodeposition of copper with nanoscale twins**

The electrodeposition was performed on gold-coated silicon wafers using a three electrode cell setup at room temperature. The bath composition and plating parameters are described in 2.2. Prior to deposition, the substrates were cleaned in a Piranha solution, rinsed in ultra-pure water and dried under air.

The copper electrodeposition was performed under pulse potential conditions using a potentiostat (Autolab PGSTAT 30, Metrohm). The pulse potential during on-time was set at -0.2 and -0.5 V vs. SCE and a pulse off-time potential of +0.55 V vs. SCE was prescribed, corresponding to the open circuit potential. The duty cycle of the pulse was varied between 0.5 and 2% by changing the pulse off-time from 1s to 4s, while keeping the pulse on-time constant at 20ms. Therefore, both the effect of the deposition potential and the relaxation time (i.e. off-time) were examined.

#### **Microstructure characterization**

Microstructure characterization of the specimens was conducted in as-deposited conditions as well as after mechanical testing with a range of apparatus including XRD, high-resolution SEM, ion contrast FIB imaging, transmission electron microscopy and transmission Kikuchi



diffraction (TKD). High-resolution micrographs of the pillars were taken before and after microcompression tests. The pillar diameter and height were extracted from the micrographs to check if they were suitable for compression and to calculate the stress-strain curves. SEM imaging after mechanical testing was used to identify evidence of the deformation mechanisms.

### 3.2.2 Controlling the twin density

Figure 3.1e shows the cross-sectional FIB-scanning ion images of a Cu film prepared by pulse plating at an on-potential of -0.2 V vs. SCE with an on-time of 20 ms and an off-time of 3 s. The FIB image shows that the deposit consists of columnar grains with 1 to 2  $\mu\text{m}$  diameters. Further analysis of the channeling contrast image show that the grains are subdivided into finer horizontal lamellae structure, suggesting the presence of nanotwins.

A TEM study of this sample confirmed the presence of the horizontally oriented nanotwins. Figure 3.1a shows a low magnification image of the sample cross-section, which reveals a high density of nanotwins with an average spacing of approximately 100 nm, consistent with the FIB observation. A high-resolution image showing the lattice plane is presented in Figure 3.1b. A twin boundary in the (111) plane is clearly seen. The Fourier transformation of the image shows the typical signature of a nanoscale twin inside a cubic crystal, characterized by mirror symmetry along (111) plane. Vertically oriented stacking faults interconnecting the twin boundaries are also observed, as shown in Figure 3.1c. The nature of the stacking faults is expected to be a twin boundary in the (112) plane, known as an incoherent twin boundary, which plays an important role in the detwinning of nt-Cu during plastic deformation [85, 86].

Figure 3.2 shows the effect of the pulse off-time on the twin density in Cu films prepared with a constant time-on of 20 ms and potential -0.2V vs. SCE. In DC plating or  $t_{off} = 0\text{s}$ , a nanocrystalline microstructure is obtained with some rare twins (Fig. 3.2a). Room temperature recrystallization was observed for this type of microstructure. Such poor thermal stability has been reported for electrodeposited nanocrystalline Cu [87]. With an off-time of 1s, we observed randomly oriented coarse grains with diameters of a few micrometers. Although some grains seem to contain some twins, they were oriented in random directions. As the pulse

### Chapter 3. Investigation of the intrinsic size effect in electrodeposited copper with nanoscale twins

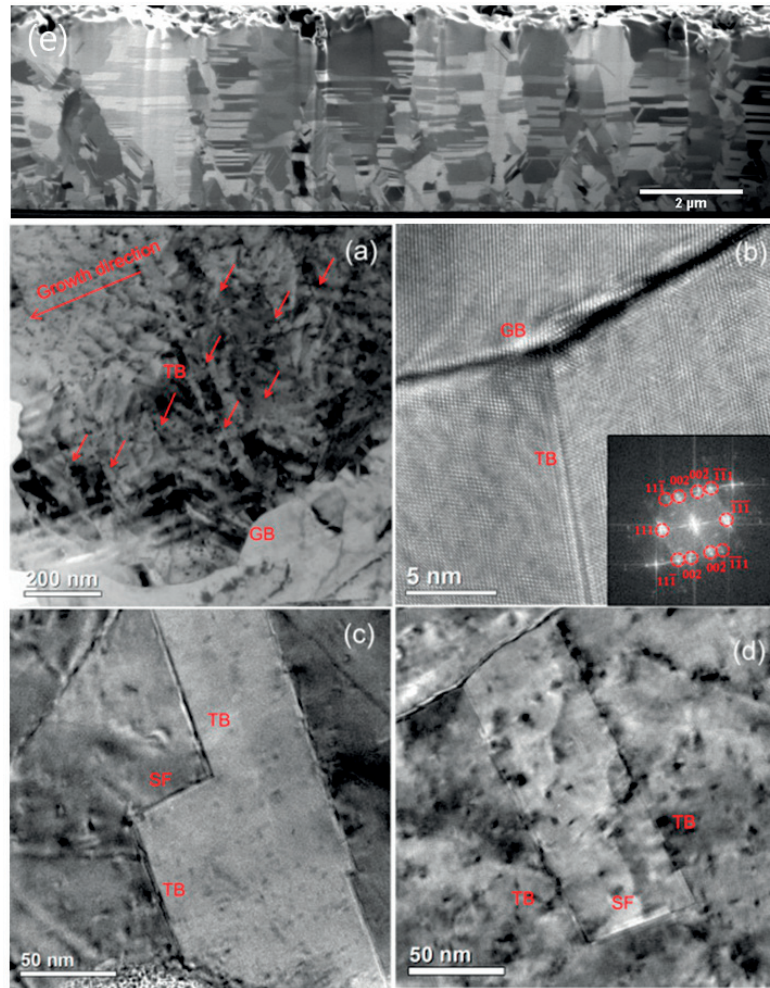


Figure 3.1 – (a-d) TEM micrographs of the corresponding Cu films with horizontally aligned twins (e). TB: twin boundary. GB: grain boundary. SF: stacking fault.

off-time increases from 2 to 4 seconds, a columnar grain structure is favored with horizontally-aligned twins. The twin density increases with longer off-time. The mean twin thickness is reduced from 180 nm to 111 nm, as illustrated by the FIB cross-sections. The twin distribution is improved for a longer off-time. It is worth noting that the number of incoherent twin boundaries decreases with a longer off-time. Unlike the nanocrystalline Cu sample, samples with nanoscale twins have proved to be extremely stable over long period of times. The change in microstructure is also revealed by the change in texture coefficient (TC) as shown in Figure 3.2f. The graph shows that all the samples prepared by pulsed electrodeposition are highly (111)-textured whereas the sample prepared by DC plating has no preferred orientation. The (111) orientation corresponds to the orientation of the twins in the (111) plane. Chan et al.

[88] suggested that this texture was favored in fcc crystals because it is the plane of lowest surface energy.

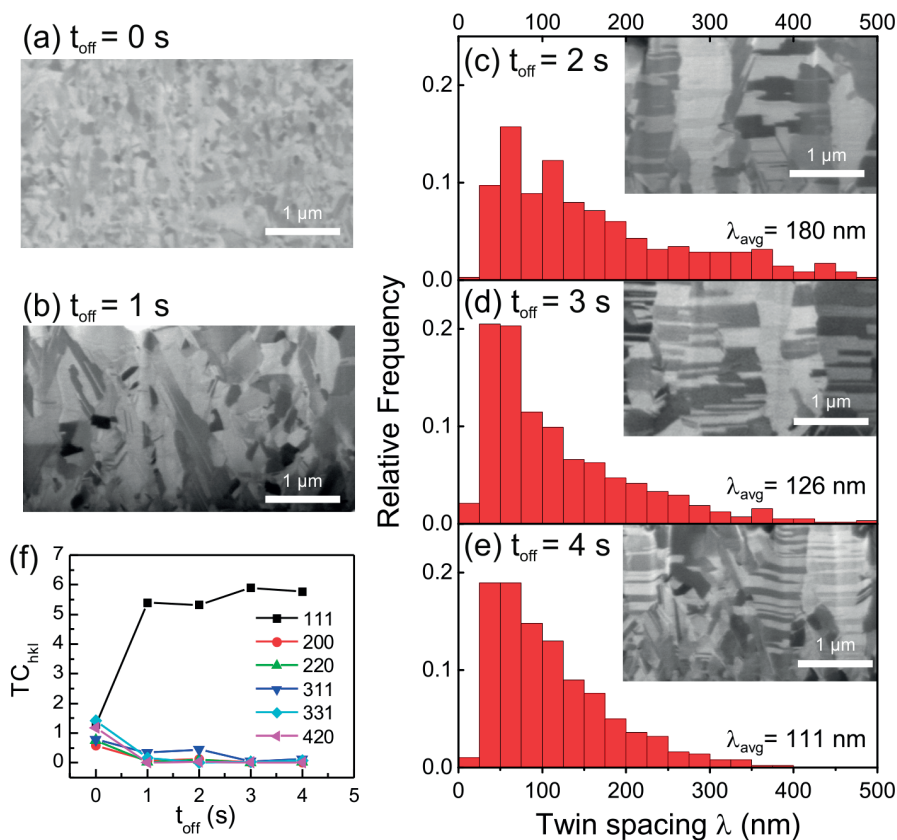


Figure 3.2 – (a-e) Effect of the off-time pulse on the microstructure of Cu films for an off-time varied from 0 s to 4 s. The twin density distribution is shown for 2 , 3 s and 4 s off-time. f) Texture coefficient of the Cu films as a function of the off-time pulse.

### 3.2.3 Controlling the twin orientation

Modification of the applied overpotential drastically modifies the morphology of the copper deposits. In particular, when we applied a potential of -0.6V vs. SCE ( $t_{\text{on}} = 20$  ms,  $t_{\text{off}} = 4$  s), the ion channeling contrast image in Figure 3.3e shows that the orientation of twin was vertical or slightly slanted ( $\pm 5^\circ$ ), *i.e.* parallel to the growth direction. The vertical twins are observed inside large columnar grains. For copper deposits prepared at the same potential but in DC-mode, the deposition proceeded in a nodular growth induced by the hydrogen evolution. Again, TEM characterization was conducted in order to confirm the presence of nanoscale twins inside the Cu deposits. A high density of the twin boundaries with the direction parallel

### Chapter 3. Investigation of the intrinsic size effect in electrodeposited copper with nanoscale twins

to the growth direction is shown in a low-magnification image in Figure 3.3a. The Fourier transformation of the high-resolution image in Figure 3.3b is consistent with the pattern from a nanotwin. In addition, the resolved lattice planes show mirror symmetry, as shown in Figure 3.3c and d. Unlike the horizontally oriented nanotwins, the vertically oriented nanotwins propagate through the grain up to the surface without intersections by grain boundaries or stacking faults, suggesting a significant difference in the growth mechanism between the horizontal and vertical nt-Cu.

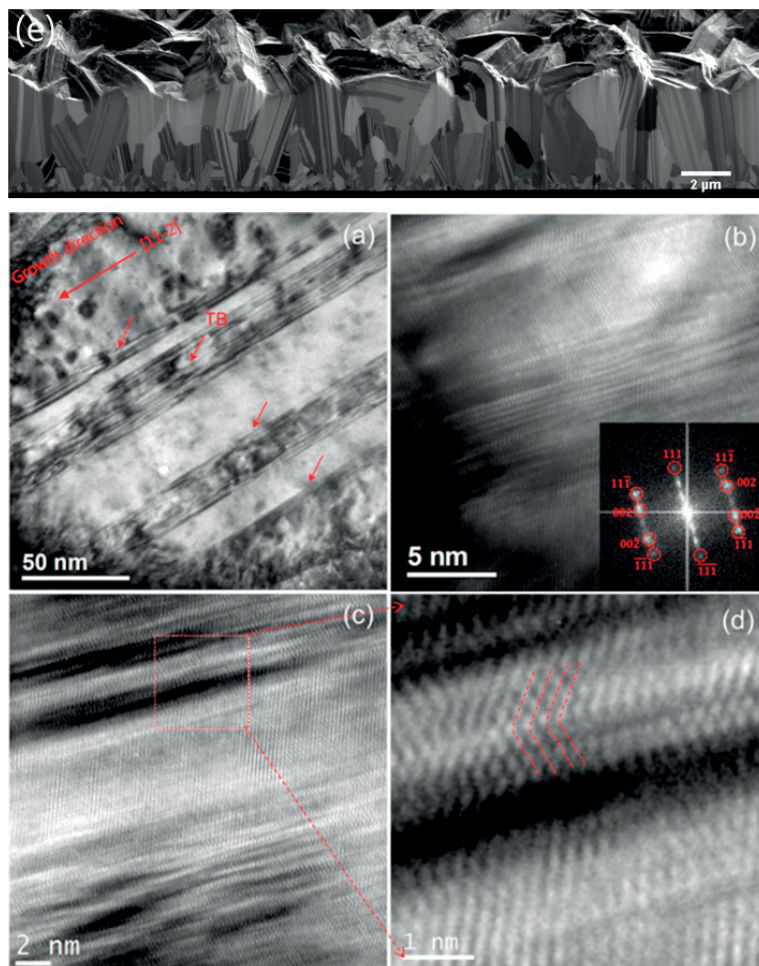


Figure 3.3 – (a-d) TEM micrographs of the corresponding Cu films with vertically aligned twins (e) obtained at  $-0.6\text{V}$  vs. SCE ( $t_{on} = 20\text{ ms}$ ,  $t_{off} = 4\text{ s}$ ). TB: twin boundary.

### 3.2.4 Twin formation mechanism during pulse plating

The results indicate a strong influence of the plating conditions on the twins orientation and density, in particular the applied potential and pulse-off time. Based on the present experimental work and previous works in the literature, a twin growth formation mechanism is proposed in Figure 3.4. At low-overpotential (i.e.  $-0.2$  vs. SCE), the copper atoms are adsorbed at the surface during on-time, which contributes to increasing the stress in the copper deposit. Part of this stress is then relieved during the off-time by diffusion of the copper adatoms and their rearrangement into a lower energy configuration. Twinning has been shown to reduce the overall energy configuration. It is consistent with the increase in twins density with longer off-time. At a larger potential (i.e.  $-0.6$  vs. SCE), hydrogen evolution is promoted. It is therefore believed that the hydrogen bubbles generated at the surface of the electrode shorten the diffusion path of copper atoms. In that case, the most favorable configuration to reduce the stress is the formation of a twin in the growth direction.

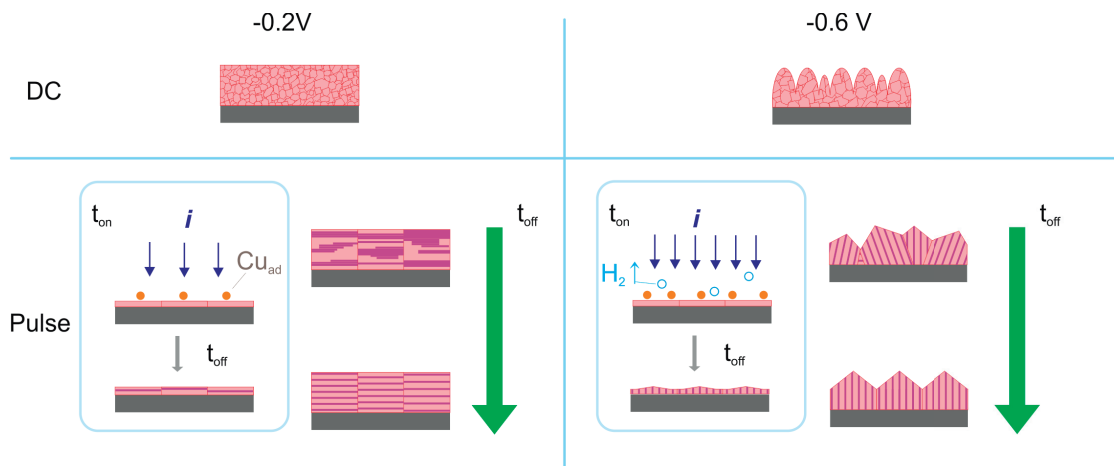


Figure 3.4 – Growth mechanism of nanotwinned copper as a function of the plating potential and pulse off-times.

## 3.3 Mechanical properties

In this section, the mechanical properties of the electrodeposited copper films with uniform and preferentially-oriented nanoscale twins were investigated by micropillar compression. Three samples with different microstructures were obtained by varying the applied potential and the duty cycle during deposition:

### Chapter 3. Investigation of the intrinsic size effect in electrodeposited copper with nanoscale twins

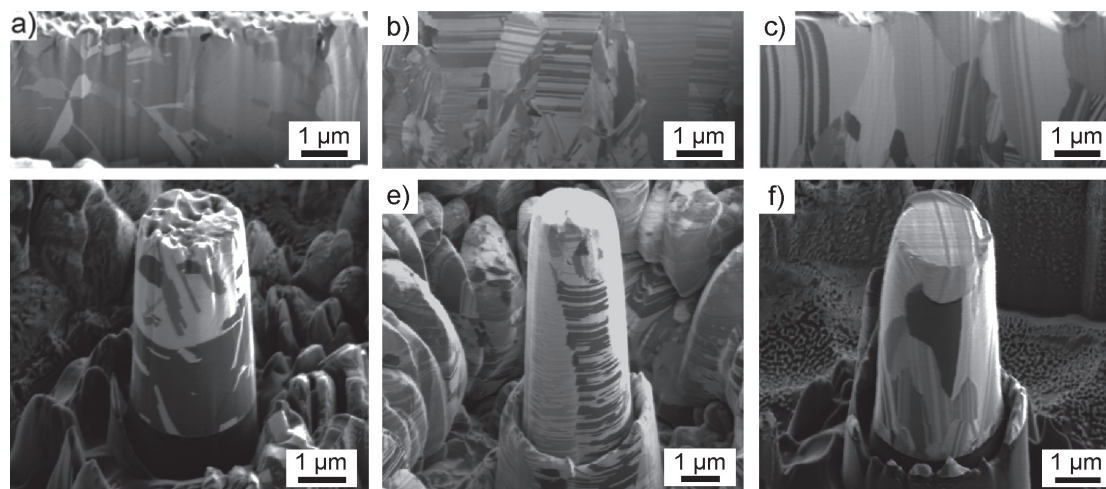


Figure 3.5 – Ion contrast channeling of the microstructure and micropillars.

- fine grained copper as a reference:  $-0.6$  V vs SCE,  $20$  ms  $T_{on}$ ,  $100$  ms  $T_{off}$ ;
- horizontally-oriented nanotwins:  $-0.2$  V vs SCE,  $20$  ms  $T_{on}$ ,  $4$  s  $T_{off}$ ;
- vertically-oriented nanotwins:  $-0.6$  V vs SCE,  $20$  ms  $T_{on}$ ,  $4$  s  $T_{off}$ .

The objective of these tests is to assess the mechanical response of nt-Cu deposits as a function of the twin orientation and density. In particular, the effect of the twin orientation of the nt-Cu deposits on their deformation mechanisms is demonstrated for both the  $\langle 111 \rangle$ - and  $\langle 11\bar{2} \rangle$ -textured nt-Cu deposits.

#### 3.3.1 Experimental

##### Micropillar fabrication by focused ion beam

The micropillars were prepared via Focused Ion Beam (FIB) using a dual beam SEM-FIB Tescan Vela instrument in a three-step approach. The milling procedure is described in Section 2.3.3. The microstructure and representative micropillars are depicted in Figure 3.5.

##### Micropillar compression testing and analysis

The mechanical properties of the nanotwinned copper (nt-Cu) micropillars were measured by micropillar compression tests using both quasi-static tests and strain rate jump tests.

The former gives the yield strength and elastic properties of the micropillars and the latter measures the activation volume which is an indirect indication of the plastic deformation mechanism. The experiments were conducted with an in situ scanning electron microscope (SEM) Alemnis indenter equipped with a diamond flat punch ( $E_{indenter} = 1040 \text{ GPa}$  and  $\nu_{indenter} = 0.07$ ). The quasi-static compression tests were performed at a constant strain rate of  $\dot{\epsilon} = 10^{-3} \text{ s}^{-1}$ . Strain rate jump tests consist of varying the deformation rate during compression and measuring the corresponding changes in flow stress. The strain rate was varied after the onset of plasticity by a factor of 25 from  $\dot{\epsilon} = 2 \times 10^{-4} \text{ s}^{-1}$  to  $\dot{\epsilon} = 5 \times 10^{-3} \text{ s}^{-1}$ . For each jump, the strain rate sensitivity (SRS) exponent is calculated as:

$$m = \frac{\delta \ln(\sigma)}{\delta \ln(\dot{\epsilon})} \quad (3.1)$$

where  $\sigma$  is the flow stress and  $\dot{\epsilon}$  is the strain rate. The apparent activation volume,  $V$ , was also estimated:

$$V = \frac{\sqrt{3}k_B T}{m\sigma} \quad (3.2)$$

where  $k_B$  is the Boltzmann constant and  $T$  is the temperature [89].

#### 3.3.2 Influence of twin orientation

Figure 3.6 shows the stress-strain curves obtained by quasi-static compression of micropillars. The mechanical properties of a fine-grained copper specimen are compared to specimens with nanoscale twins oriented either vertically or horizontally. Table 3.1 gives the loading modulus  $E$  and yield strength  $\sigma_y$  extracted from the stress-strain curves for each specimen.

Stress-strain curves displayed in Figure 3.6a highlight the enhancement of mechanical properties with the presence of twins. Copper micropillars with highly-oriented horizontal twins present the highest strength of all the samples. The yield strength is increased by a factor of two when compared to fine-grained copper. This demonstrates the beneficial effect of the inclusion of twins within the microstructure. The mechanical response is also sensitive to the twin orientation. Horizontal nanotwins outperform vertical nanotwins. When the twins are perpendicular or almost perpendicular to the loading direction, the stress-strain curve show

### Chapter 3. Investigation of the intrinsic size effect in electrodeposited copper with nanoscale twins

Table 3.1 – Aspect ratio, diameter,  $\varnothing$ , and mechanical properties of electrodeposited copper micropillars with fine grained microstructure, vertical twins and horizontal twins. The strength,  $\sigma_{5\%}$ , loading modulus,  $E$ , strain rate sensitivity exponent,  $m$ , and apparent activation volume,  $V$ , are given together with the standard deviation.

	ufg-Cu	Vertical nt-Cu	Horizontal nt-Cu
Aspect ratio	$\sim 2$	2.4–2.7	2.5–2.9
$\varnothing$ ( $\mu m$ )	2.2–2.4	1.8–2	2.6–2.8
$E$ (GPa)	$37 \pm 2$	$35 \pm 4$	$47 \pm 3$
$\sigma_{5\%}$ (MPa)	$269 \pm 40$	$389 \pm 34$	$618 \pm 62$
$m$	$0.012 \pm 0.003$	$0.030 \pm 0.008$	$0.011 \pm 0.002$
$V$ ( $b^3$ )	$24 \pm 4$	$9.3 \pm 6$	$26 \pm 2$

an intermediate strength between horizontally-aligned twins and fine-grained copper.

Another way to assess the deformation mechanisms is by measuring the strain rate sensitivity exponent and activation volume through strain rate jump tests (Figure 3.6). Similar  $m$  values are measured for ufg-Cu and horizontally oriented nanotwins with  $m = 0.012 \pm 0.003$  and  $m = 0.011 \pm 0.002$ , respectively. However, vertical twins present a strain rate sensitivity which is higher:  $m = 0.030 \pm 0.008$ . A larger standard deviation is also observed for vertical twins. This deviation can be related to the twin mis-orientation or tilt with respect to the loading direction. The tilt may slightly vary from one pillar to another depending on the probed grains. The apparent activation volume is inversely proportional to the strain rate sensitivity exponent and the stress. As a result, activation volume for ufg-Cu is  $24 \pm 4b^3$ ,  $26 \pm 2b^3$  for horizontal nanotwins and  $9.3 \pm 6b^3$  for vertical nanotwins, where  $b$  is the Burger's vector of copper ( $b_{Cu} = 0.255$  nm).

#### 3.3.3 Deformation mechanisms in nt-Cu

The strong anisotropy as a function of the twin orientation is consistent with literature [52] and indicates a change in deformation mechanism. Two effects need to be considered: the average twin spacing and the twin orientation. It is thought that above 100 nm twin spacing, no difference in deformation mechanism with the loading direction occurs, because deformation proceeds via intra twin dislocation–dislocation interaction. However, all the tested samples have a twin spacing below this size. In this case, the relative loading direction will drive the



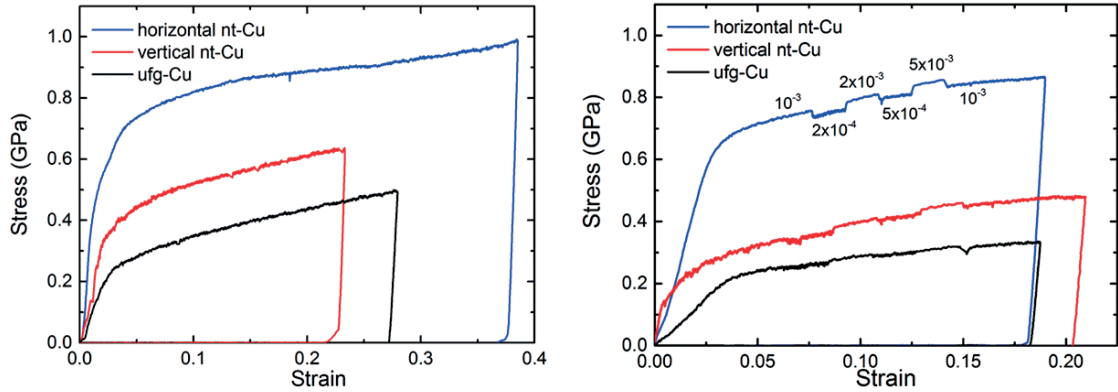


Figure 3.6 – Representative stress-strain curves for a) quasi-static and b) strain rate jump microcompression.

deformation mechanism.

The value of the activation volume as a function of the twin orientation in as-deposited conditions confirms previous observation reported in the literature [51]. Typically, activation volume in fcc metals with coarse grained structure is of the order of  $100\text{--}1000b^3$  [90]. This corresponds to a mobile dislocation interacting with forest dislocations. At the other end, diffusion-based mechanisms are as small as  $1b^3$  [91]. However, our results present an intermediate activation volume in the order of  $10b^3$ , suggesting a different rate-controlling deformation mechanism. Similarly low values of small activation volumes are expected and observed in nt-Cu (typically  $10\text{--}20b^3$ ) and in pure nanocrystalline metals [92]. Diffusion-based mechanisms dominate at low stresses and high homologous temperatures, both of which are not the conditions in the present study. Hence, it is correct to expect dislocation-based deformation mechanisms as the main mechanism even in the vertically-oriented nt-Cu. In fact, the presence in the microstructure of both grain boundaries and a high density of twin boundaries may introduce additional plastic deformation mechanisms. In particular, the emission of partial dislocations at the grain boundaries or at the twin boundaries results in complex twin-dislocation and dislocation–dislocation interactions. These processes could cause the higher strain rate sensitivity and lower activation volume observed in nanotwinned copper when compared to their coarse-grained counterparts.

Plastic deformation in fcc metals occurs through activation of  $\langle 111 \rangle \{110\}$  slip systems. There are 12 slip systems in copper: 4 slip planes and 3 slip directions for each plane. They can

### Chapter 3. Investigation of the intrinsic size effect in electrodeposited copper with nanoscale twins

be represented with a Thompson tetrahedron (cf. Figure 3.7a). The faces of the tetrahedron are the slip planes and the edges are the dislocation amplitude and direction. In the case of a horizontal twin boundary contained in a (111) plane, one can depict the twinned fcc structure with a double Thompson tetrahedron. The line between the Greek letters and the tetrahedron corners indicates the direction and amplitude of the partial dislocations.

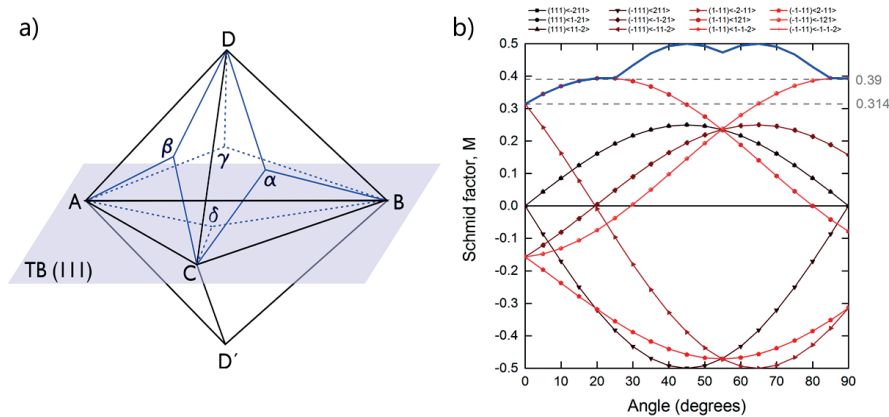


Figure 3.7 – a) Thompson tetrahedron for twinned fcc crystal in the (111) plane and b) Angular dependence of the Schmid factor for each slip system.

Let's now consider what would be the slip system in a twinned crystal. The slip system in twinned cubic crystal is  $\langle 111 \rangle \{11\bar{2}\}$ , as described in Table 3.2. The preferred deformation is captured by the Schmid factor,  $M = \cos\lambda \sin\theta$ , where  $\lambda$  is the angle between the slip plane and the loading direction whereas  $\theta$  is the angle between the slip direction and the loading direction. A higher value of M means a higher mechanical strength because  $\sigma = M \times \tau$ . When computing the Schmid factor for each loading direction, the value for vertical twins ( $M = 0.393$ ) exceeds the one for horizontal twins ( $M = 0.314$ ). Therefore an increase of 25% in strength is expected for horizontally-aligned nt-Cu when compared to vertically-aligned nt-Cu. An actual difference of 59% was found experimentally between the two directions (cf. Figure 3.7b). The discrepancy can be attributed to non-idealities in micropillars, such as grain boundaries and twin boundary misorientations. It is actually possible to quantify the effect of twin misorientation on the Schmid factor.

The reason for this behavior is that both the slip plane and slip direction in horizontal twins are inclined to the twin boundary, which favors dislocation pile-up against the twin boundary. On the other hand, in vertical twins the slip plane is inclined to the twin boundary but the

Table 3.2 – Slip plane and twin directions in a twinned crystal

Twinning plane	Directions	Twinning plane	Directions
(111)	$\begin{bmatrix} \bar{2}11 \\ 121 \\ 112 \end{bmatrix}$	( $\bar{1}\bar{1}$ )	$\begin{bmatrix} 2\bar{1}1 \\ 121 \\ 112 \end{bmatrix}$
( $\bar{1}\bar{1}$ )	$\begin{bmatrix} 211 \\ \bar{1}21 \\ 112 \end{bmatrix}$	(111)	$\begin{bmatrix} 2\bar{1}1 \\ 121 \\ 112 \end{bmatrix}$

slip direction is parallel to the twin boundary. In that case, the development of threading dislocations is expected. This simple analysis is able to explain the difference in strength observed experimentally as a function of the twin orientation. It also supports the change in deformation mechanism that was shown by the higher strain rate sensitivity for vertical twins.

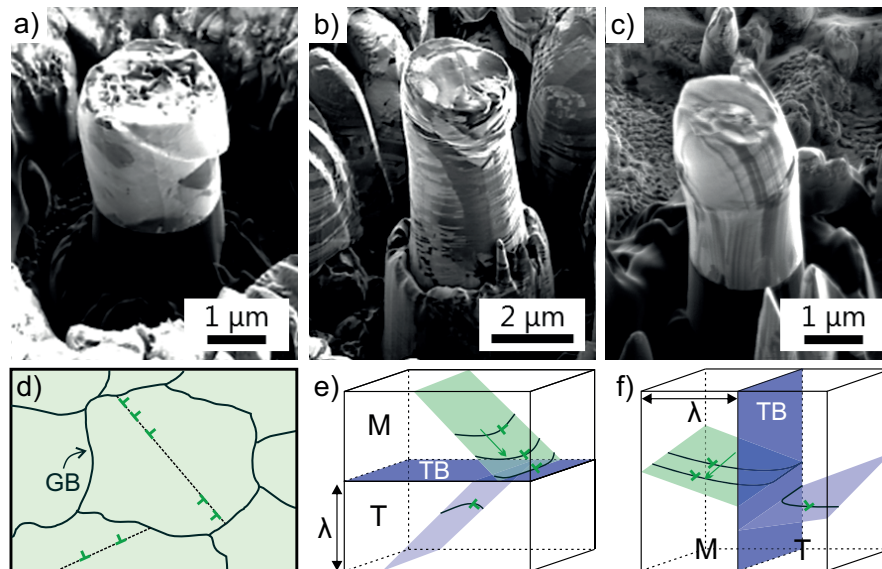


Figure 3.8 – Ion channelling contrast micrographs of (a) ufg-Cu, (b) horizontal nt-Cu and (c) vertical nt-Cu micropillars after compression. A schematic of the deformation mechanisms as a function of the microstructure, slip planes, slip directions and dislocation activity is given for each microstructure (d, e and f respectively). Here GB is grain boundary, T is twin, M is matrix, TB is twin boundary and  $\lambda$  is the twin thickness.

### 3.3.4 Elastic properties of nt-Cu

The Young's modulus was also extracted from the stress-strain curves for horizontal and vertical twins (Table 3.1). Small variations were observed between the different specimens but the absolute value was abnormally small: the actual value being only one third of the

### Chapter 3. Investigation of the intrinsic size effect in electrodeposited copper with nanoscale twins

expected modulus ( $E_{Cu} = 160 - 180 \text{ GPa}$  in the (111) orientation [93]). The elastic modulus is the measure of the bond strength between atoms. Therefore atom arrangement strongly influences the modulus of elasticity but this is not enough to explain the observed difference. Small misalignment of the pillar top surface relative to the loading direction can result in a dramatic reduction of the loading modulus. Zhang et al. [94] demonstrated a 50% reduction of modulus with a  $2^\circ$  misalignment. In order to investigate the effect of the geometry on the elastic properties, a reverse approach has been implemented. The onset of plasticity was determined from the stress strain curves. Then the elastic deformation corresponding to that level of stress was calculated assuming different values of Young's modulus. The plot in Figure 3.9 shows that the elastic deformation corresponds to only a few tens of nanometer. If we consider a pillar with a diameter of 2 micrometers, a misalignment of only  $1^\circ$  between the flat punch and the top surface results in a difference in height of 35 nm across the pillar, which is on the order of the elastic deformation. Small misalignment of the pillar top surface relative to the loading direction can result in dramatic reduction of the loading modulus at this length scale.

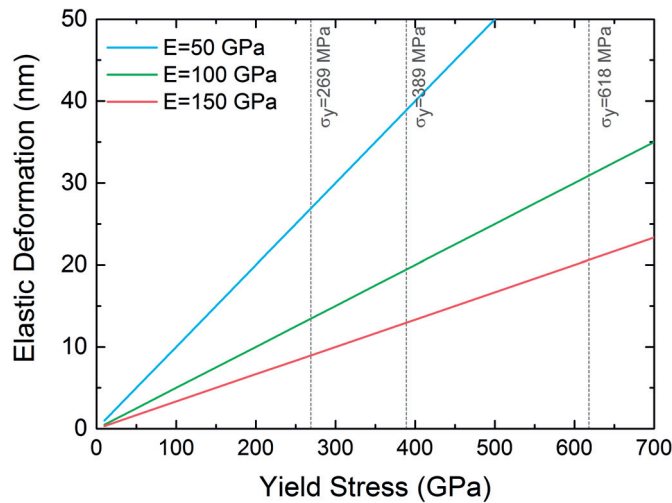


Figure 3.9 – Magnitude of the elastic deformation in deformation as a function of the yield stress for several values of Young's modulus. Dashed lines represent the measured flow stress in the Cu micropillars.

## 3.4 Summary

This chapter outlines the potential of grain boundary engineering with nanoscale twins. Good control of the plating conditions produces Cu films with highly oriented twins. It was found that the twin orientation could be altered from horizontal to vertical by varying the applied potential. This change in twin orientation is attributed to a reduction of diffusion path length of the copper adatoms. In the case of horizontal nanotwin copper, the twin density increased with longer off-time pulse, supporting the claim that the twin formation is linked to stress relaxation during the off-time period, mediated by a diffusion process. Microcompression tests of nanotwinned copper films exhibited high strengths larger than nanocrystalline copper. In addition, the tests showed a strong mechanical anisotropy with the twin orientation. This is related to a change in the dislocation mechanism from dislocation pile-ups at the twin boundary for horizontal twins to dislocations threading inside the twin lamella for vertical twins.

By controlling both the twin density and orientation with appropriate plating parameters, one can go beyond the Hall-Petch relationship for polycrystalline metals and produce functional materials relevant to industry. This chapter exemplifies the concept of controlling the intrinsic size effects in metals to achieve metals with novel properties. In the following chapter, the intrinsic size effect is combined with the extrinsic size effect to produce high-strength cellular metals.



## 4 Investigation of the extrinsic size effect

The mechanical properties of pure metals depend primarily on their crystallographic structure, as shown in the previous chapter, but also on their dimensions when they are small enough. The fact that the mechanical properties of metals change with dimension is called the extrinsic size effect. A distinction must be made between crystalline metals for which a "smaller is stronger" trend is observed and amorphous metal for which a "smaller is ductile" transition occurs. In this chapter, we will therefore review the extrinsic size effect in micro-cellular metals. The first section presents the mechanical results for 3D micro-lattices coated with an amorphous NiB. In the second section, we examine the mechanical properties of nickel inverse opals.

*Parts of this chapter use materials adapted from Mieszala et al. [95] with permission from the Royal Society of Chemistry.*

### 4.1 Effect of the NiB thickness in micro-lattices

In this section, we present the mechanical behaviour of hybrid NiB/polymer micro-lattices obtained by laser lithography and electroless deposition of NiB. The NiB coating thickness was varied to probe the extrinsic size effect in amorphous metal.

### 4.1.1 Control of the NiB film thickness

As mentioned before, it is important to precisely control the uniformity and thickness of the NiB deposit if one wants to correlate the brittle-to-ductile transition with the thickness. NiB electroless deposition on the 3D polymer template was performed according to the process presented in 2.2.3. The deposition thickness was adjusted with the plating time. The plating rate was calibrated for a flat surface and was found to be  $33 \text{ nm.min}^{-1}$ . Thus, the plating time was varied from 18 s to 3 min to achieve NiB film thicknesses ranging from 10 to 100 nm on. These samples were heat treated at  $200^\circ\text{C}$  for 40 min in air after every minute of plating in order to relieve residual stresses and avoid crack formation in the films. The temperature of the heat treatment was chosen to prevent crystallization of the deposited films[96].

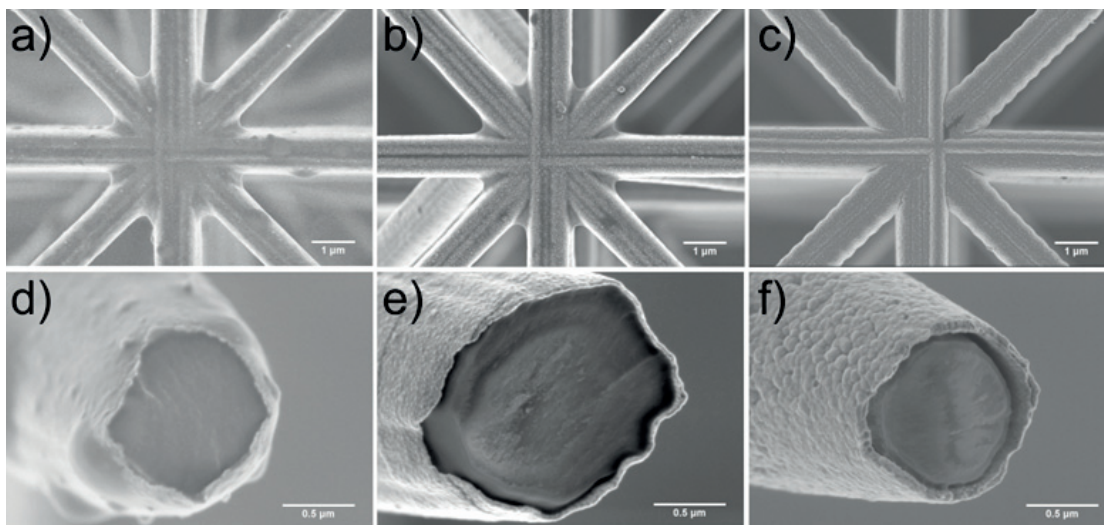


Figure 4.1 – SEM images showing conformal NiB coverage in complex features and uniform NiB coating thickness for a,d) 10 nm, b,e) 30 nm, and c,f) 100 nm.

Figure 2.3 shows SEM micrographs of the polymer template after NiB electroless deposition. Figure 4.1 confirms the good coverage uniformity of NiB even in complex geometry. The micrographs were also used to measure the NiB thickness to make that the same deposition rate applies on polymeric structure.



### 4.1.2 Structural properties of the reference film

The elemental composition and structural properties of the NiB reference film were measured by using elastic recoil detection analysis (ERDA) with a 13 MeV  $^{127}\text{I}$  ion beam and XRD, respectively. The atomic ratio between boron and nickel in the sample was found to be 0.22, yielding an overall composition of  $\text{Ni}_{78}\text{B}_{22}$ . Figure 4.2a shows the XRD pattern obtained from the reference NiB film. Only two sharp peaks are identified and were assigned to Au(111) and Si(100), respectively. The broad peak observed between  $2\theta = 40^\circ$  and  $2\theta = 50^\circ$  suggests that the film is amorphous in as-deposited state, which is consistent with earlier observations [97, 98]. TEM imaging confirmed that the amorphous structure of the NiB deposits was independent of the film thickness (Figure 4.2b). The bright field images did not reveal any diffraction contrast and the selected area diffraction pattern (SAED) exhibited only diffuse rings characteristic of an amorphous material.

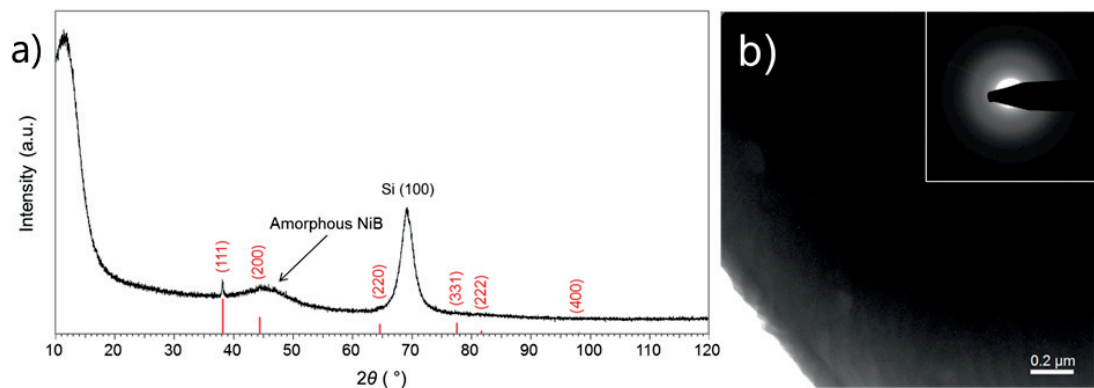


Figure 4.2 – a) XRD diffractogram of the NiB reference on Au-coated Si wafer. Au peaks are indexed in red. b) Bright field image of a representative 30 nm NiB coating. Inset: corresponding SAED pattern.

### 4.1.3 Mechanical properties of the reference film

In order to understand the mechanical properties of hybrid NiB/polymer micro-lattices, we first need to characterize the mechanical properties of bulk NiB. The mechanical properties were measured on a 1.6  $\mu\text{m}$ -thick NiB reference film using a Berkovich indenter tip on an *Alepnis GmbH* nanoindenter system in a load-controlled mode. The maximum depth of penetration of the indenter at maximum load was maintained below 10 % of the film thickness

to minimize the substrate influence. A constant indentation strain rate,  $\dot{\epsilon} = 5 \times 10^{-3} \text{ s}^{-1}$ , was maintained up to the required maximum load of 50 mN.

The hardness (H) and Young's modulus (E) of the NiB film was extracted from the load vs. indentation depth curves. The values of hardness,  $H_{NiB} = 13 \text{ GPa}$ , and Young's modulus,  $E_{NiB} = 250 \text{ GPa}$ , of the NiB film correspond to the upper bound of the previously reported values from the literature for amorphous NiB films[99, 100, 98], which is consistent with the high boron content. Note that the Young's modulus (E) was obtained from the reduced modulus using equation 4.1:

$$E_r = \frac{1 - \nu_{NiB}^2}{E_{NiB}} + \frac{1 - \nu_i^2}{E_i} \quad (4.1)$$

where the Young's modulus and Poisson's ratio of the diamond tip are  $E_i = 1140 \text{ GPa}$ ,  $\nu_i = 0.07$ , respectively, while the Poisson's ratio of NiB is taken as  $\nu_{NiB} = 0.3$ .

### 4.1.4 Mechanical properties of micro-lattices as a function of NiB thickness

The mechanical properties of the micro-architected structures were obtained by using an *in situ* SEM nanoindentation system. Uniaxial compression tests were conducted in a displacement-controlled mode with a  $100 \mu\text{m}$ -diameter diamond flat punch at a displacement rate of  $20 \text{ nm/s}$ . The load-displacement obtained were corrected for thermal drift and instrument compliance. Engineering stress and strain were calculated from the load-displacement curves using the cross-sectional footprint area and the height of each structure, respectively.

4.1. Effect of the NiB thickness in micro-lattices

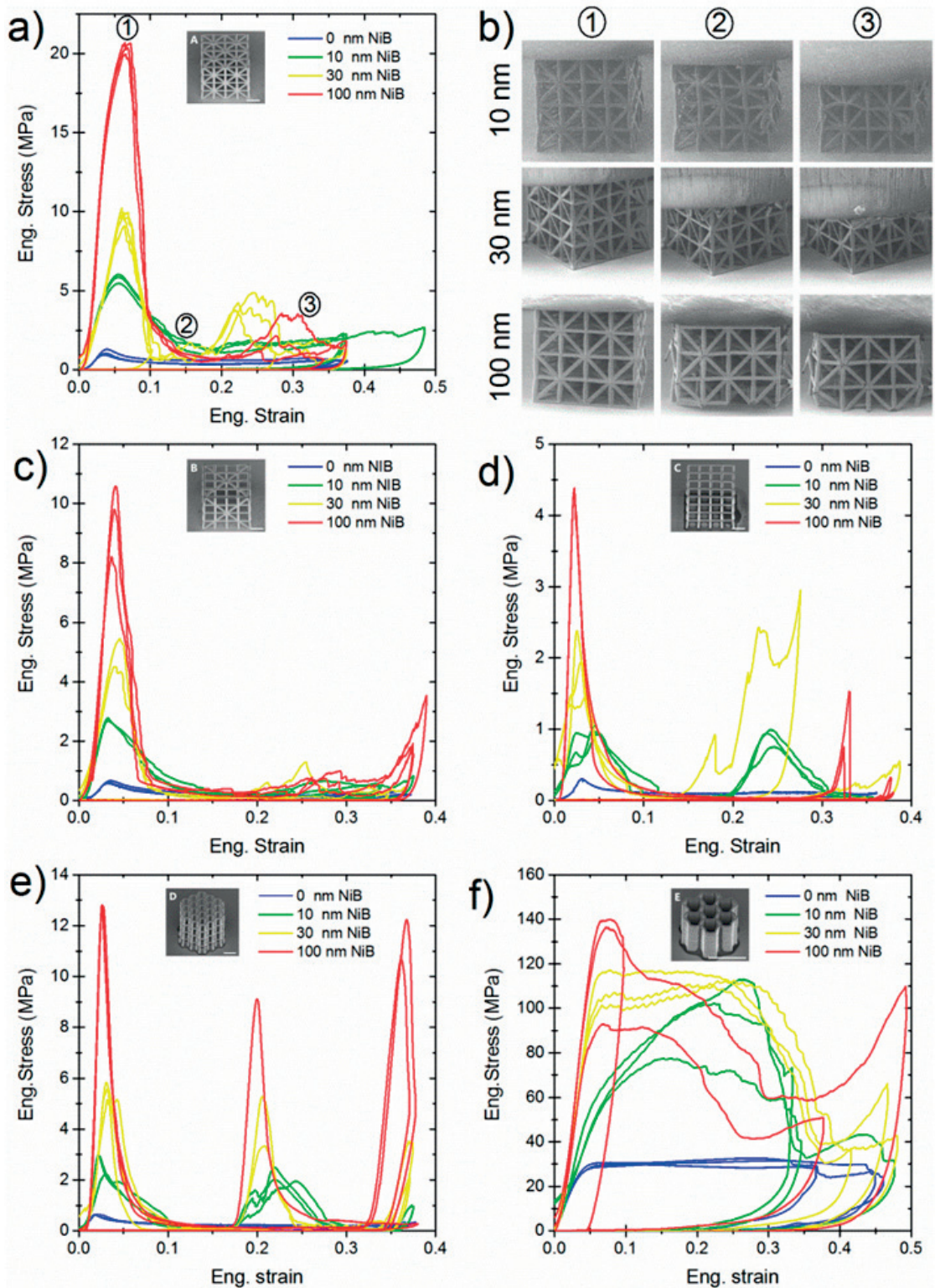
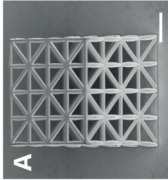
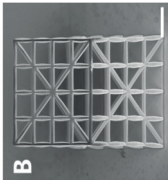
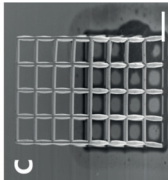
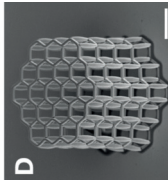
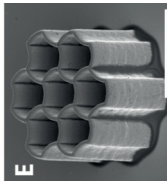


Figure 4.3 – Engineering stress-strain curves as a function of the NiB coating thickness for micro-lattice A, B, C, D and E (a, c-f). b) SEM micrographs of structure A during micro-compression at various levels of strain for 10 nm, 30 nm and 100 nm NiB coating.

Table 4.1 – Physical and mechanical properties as a function of the NiB thickness for each micro-architecture. Values for the peak strength, specific strength and loading modulus are given as mean  $\pm$  standard deviation. Scale bars are 10  $\mu\text{m}$ .

	NiB thickness		Volume fraction		Solid materials		Density $\text{kg}\cdot\text{m}^{-3}$	Peak Strength MPa	Spec. Strength $\text{MPa}\cdot\text{kg}^{-1}\cdot\text{m}^3$	Loading Modulus E, MPa
	mm	nm	Air %	Solid %	Polymer %	NiB %				
	0	11.9	88.1	11.9	100	0	123	$1.10 \pm 0.15$	0.007	51
	10	12.3	87.7	12.3	97.1	2.9	158	$5.79 \pm 0.23$	0.032	165
	30	87	87	13	92.9	7.1	230	$9.77 \pm 0.48$	0.041	221.5
	100	84.5	84.5	15.5	77.1	22.9	441	$20.45 \pm 0.34$	0.046	655
	0	9.2	90.8	9.2	100	0	118	$0.61 \pm 0.04$	0.005	33.2
	10	9.4	90.6	9.4	97.1	2.9	139	$2.72 \pm 0.04$	0.019	135
	30	90	90	10	93	7	176	$4.98 \pm 0.48$	0.028	155
	100	88.1	88.1	11.9	77.3	22.7	337	$9.53 \pm 1.02$	0.028	443
	0	6.4	93.6	6.4	100	0	82	$0.30 \pm 0.08$	0.005	14.79
	10	6.6	93.4	6.6	97.8	2.2	95	$0.99 \pm 0.05$	0.010	44
	30	93	93	7	93.3	6.7	122	$1.94 \pm 0.45$	0.016	116
	100	91.8	91.8	8.2	77.5	22.5	231	$4.18 \pm 0.28$	0.017	344
	0	13.6	86.4	13.6	100	0	175	$0.64 \pm 0.01$	0.007	56.9
	10	13.9	86.1	13.9	98	2	198	$2.74 \pm 0.35$	0.014	219
	30	85.4	85.4	14.6	94	6	247	$5.53 \pm 0.27$	0.022	348
	100	83	83	17	80	20	450	$12.72 \pm 0.14$	0.028	1117
	0	32.8	67.2	32.8	100	0	422	$31.3 \pm 1.2$	0.07	760
	10	34	66	34	96.7	3.3	514	$97.7 \pm 14.8$	0.21	1053
	30	63.6	63.6	36.4	90.1	9.9	714	$113.5 \pm 2.7$	0.17	2283
	100	55.2	55.2	44.8	67	33	1584	$123.0 \pm 21.4$	0.08	2695

#### 4.1. Effect of the NiB thickness in micro-lattices

---

Figure 4.3 shows the stress-strain curves for each cellular micro-architecture coated with three NiB thicknesses, *i.e.* 10 nm, 30 nm and 100 nm-thick films and also for uncoated structures. The compressive response is typical of cellular materials starting with a linear elastic regime, followed by plastic yielding and ending by a plateau stress. If the structures were to be compressed further, an increase in the stress would be observed indicating densification. The loading modulus ( $E$ ) is defined as the slope in the linear elastic regime. The peak strength ( $\sigma_{peak}$ ) designates the maximum stress achieved by the structure. In some experiments, a non-linear region where the slope increases with increasing strain is observed at low strains ( $\varepsilon \leq 0.02$ ). This non-linear elastic response was attributed to the misalignment between the flat punch and the top plane of the micro-architecture. However, the misalignment was proven to have little effect on the overall mechanical response on repeating the experiment.

Table 4.1 summarizes the mechanical properties obtained from the microcompression tests as a function of the NiB thickness. For each micro-architecture the density, loading modulus, peak strength and specific strength, *i.e.* the peak strength divided by the density, are given. The density was derived from the mass of the parent material(s) required to produce the structure divided by the total volume that it fills. The mass was calculated from the volume fraction of each phase (solid-air) and the density of the composite bulk material obtained using a rule of mixtures. The density of the IP-Dip polymer is  $\rho_{IP-Dip} = 1.28 \text{ g.cm}^{-3}$  and  $\rho_{NiB} = 8.6 \text{ g.cm}^{-3}$  for the NiB shell.

##### 4.1.5 Brittle-to-ductile transition in amorphous NiB

Another interesting observation is the apparent brittle-to-ductile transition with increasing NiB layer thickness. Size effects in films of amorphous metals can cause homogeneous flow in the submicron range and shear band propagation above, resulting in an apparent brittle behavior [101, 102]. The critical thickness, at which the ductile to brittle transition occurs, is given by Lee et al. [103]:

$$t_{cr} = \frac{2\sqrt{2}E\Gamma}{\sigma_y^2 A} \quad (4.2)$$

## Chapter 4. Investigation of the extrinsic size effect

with  $E$ , the young's modulus,  $\sigma_y$ , the yield strength,  $A$ , the aspect ratio and  $\Gamma$ , the shear band energy per unit area. Typical value of  $\Gamma$  is  $\sim 10 \text{ J.m}^2$ , corresponding to a 10 nm-thick shear band [104, 105]. Using equation 4.2 with  $E_{NiB} = 250 \text{ GPa}$  and  $\sigma_y \approx \frac{H}{3} = 4.3 \text{ GPa}$ , the critical thickness is  $t_{cr} = 38 \text{ nm}$ , which agrees well with our observations in Figure 4.4. For 10 nm thick NiB, large plastic deformation and partial recovery is observed while for 100 nm NiB the micro-architectures fail in a brittle manner and an intermediate deformation is dominant for 30 nm NiB layer. This shows that size effects can be combined with hierarchical effect in composite micro-architectures to tune the strength, stress and failure behavior.

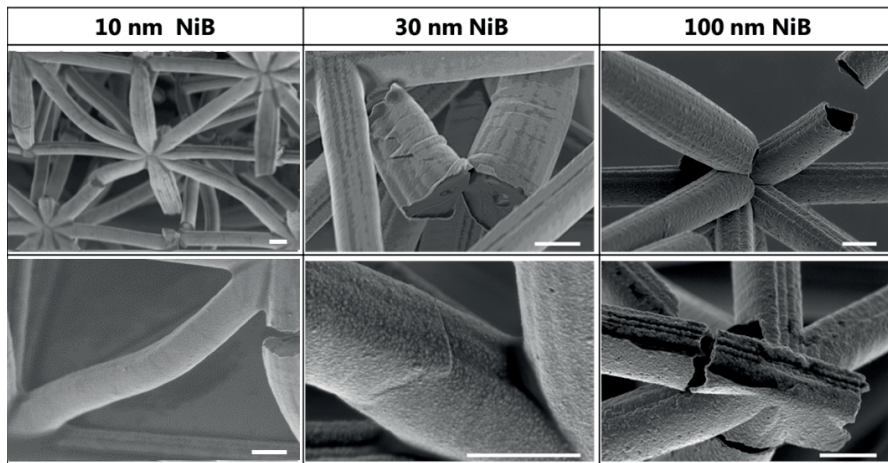


Figure 4.4 – SEM images of the micro-architectures after compression revealing the ductile nature of NiB at 10 nm but its brittle nature at 100 nm. Scale bars are  $1 \mu\text{m}$ .

### 4.1.6 Load drops analysis as an indirect evidence of brittle-to-ductile transition

The stress-strain curves recorded during *in situ* displacement-controlled microcompression experiments show abrupt decreases of stress at constant strain during loading (see Figure 4.5.a). Those discrete events are referred to as load drops. In crystalline and amorphous solids, the load drops are associated with dislocation activity and rearrangement of atomic clusters [106, 107]. In the case of 3D cellular materials, load drops are an indication of catastrophic events such as the fracture of a strut or buckling. A systematic load-drop analysis was therefore conducted to determine the number of load drops, their magnitude and their distribution for each architecture. On the other hand, it is possible to relate these events with the video frames taken during the *in situ* microcompression.

#### 4.1. Effect of the NiB thickness in micro-lattices

Figure 4.5 presents the method that we applied to perform the statistical analysis of the stress drops. To determine the number of stress drops and their magnitude, corresponding  $|\Delta\sigma/\Delta\varepsilon|$  vs. strain relations were plotted in Figure 4.5a. Based on that, we defined as stress drop any stress burst that exceeds the three-sigma limits. It is then possible to plot the stress drops magnitude as a function of the strain as in Figure 4.5b and the cumulative probability distribution of the stress drops, *i.e.* the percentage of the number of stress drops larger than a given stress drop,  $\Delta\sigma$ ,  $P(P > \Delta\sigma)$  as shown in Figure 4.5c.

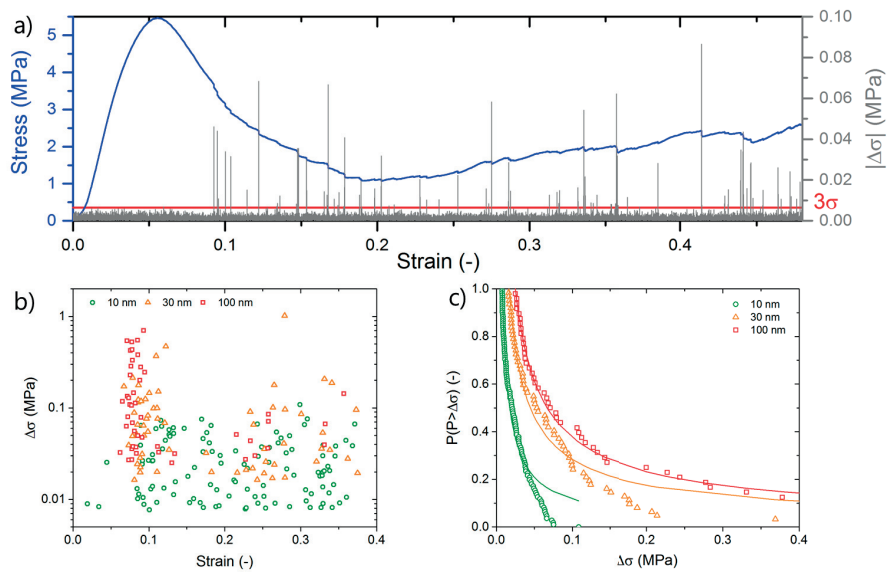


Figure 4.5 – a) Engineering stress-strain curves for micro-architecture A with corresponding  $|\Delta\sigma/\Delta\varepsilon|$  vs. time plotted on the same graph. b) Stress drop magnitude against strain for 10 nm, 30 nm and 100 nm NiB. c) Cumulative probability distribution of the stress drops as a function of the stress drop magnitude. Solid lines present a power-law scaling.

This analysis was conducted for each micro-architecture geometry and each NiB thickness. Results of the analysis are given in Figure 4.6. The number of load-drops and their magnitude tend to increase with thicker NiB layer. For micro-architectures A, D, and E, the number of stress drops first increases for 10 nm and 30 nm NiB layer before decreasing for 100 nm NiB layer. The decrease in the number of stress drops for 100 nm NiB layer is associated with the sudden release of stored elastic energy by fracture of multiple struts in a single event. Each event is, however, characterized by larger stress drop intensity. On the other hand, the number of stress drops for structures B and C continuously increases with NiB thickness. Such behavior is related to the inherent mechanical instability at the nodes induced by the low

stiffness design. During compression, the collapse mechanism proceeds by rotation of the struts around the nodes, acting as plastic hinges, which results in a smooth stress decrease. As the NiB layer gets thicker, this mechanism is delayed and more strut fractures, *i.e.* more stress drops, are observed. The signature of the failure of the architecture is visible from the load drops analysis. The stiffer micro-lattices (A and B) show a larger number of load drops when compared to structure C and D, which fail by shearing. The honeycomb structure, E, is characterized by a limited number of load drop events considering that the structure fails by crack initiation and propagation.

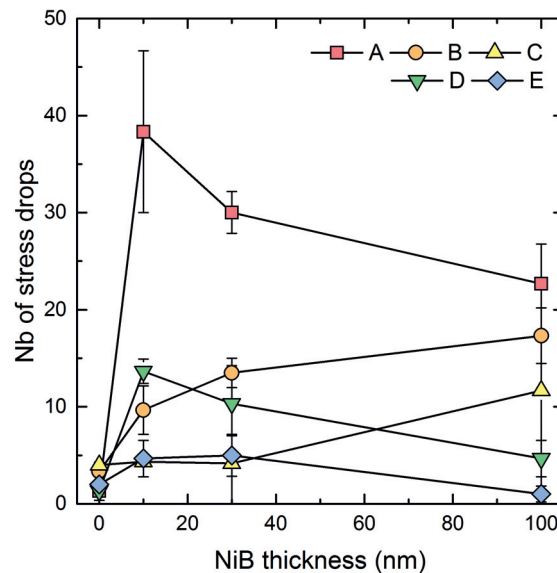


Figure 4.6 – Number of stress drops as a function of the micro-architecture and NiB thickness.

### 4.2 Effect of the ligament size in nc-Ni inverse opals

In this section, the synthesis and mechanical properties of nanocrystalline nickel inverse opals obtained by dual templating and electrodeposition are presented. The mechanical properties of such structures are investigated for different ligament sizes. The ligament size is defined as the smallest dimension of the metal element connecting two pores, as depicted in Figure 4.7. Reducing the size of the ligament is expected to produce nickel inverse opals with enhanced mechanical properties due to the extrinsic size effect.



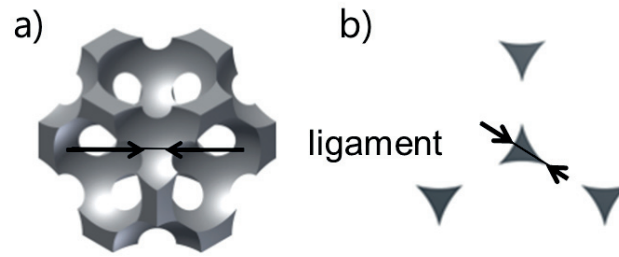


Figure 4.7 – Schematic of a) nickel inverse opal unit cell and b) cross-section of the unit cell revealing the ligament size.

### 4.2.1 Synthesis of porous regular foams with metals

#### Process overview

The process to produce nickel inverse opals (ordered 3D macroporous metal foams) uses a bottom-up approach combining self-assembly of polystyrene (PS) microspheres inside UV-LiGA molds followed by Ni electrodeposition. This unique combination of manufacturing processes enables the control of both the porous features and the microstructure. As illustrated in Figure 4.8, UV-LiGA lithography was first performed to produce micropillars of different cross-sectional shapes and dimensions. The pillar molds were then filled with PS microspheres self-assembled into an ordered colloidal crystal. Nanocrystalline Ni was finally plated inside the the dual template. After removal of the UV-LiGA templates and PS microspheres by reactive ion etching (RIE), nanocrystalline Ni micropillars with an inverse opal structure are obtained.

#### UV-LIGA lithography

As mentioned before, a dual templating technique was used to create the Ni inverse micropillars. The UV-LiGA lithography technique was used to create molds with the desired micropillar shape. The UV-LiGA were made of 80  $\mu\text{m}$ -thick SU-8 negative photoresist on Au-coated silicon wafer according to the procedure described in Section 2.1.1.

Micropillars with different geometries were produced, including circular, square, triangular and pentagonal cross-sections. The dimensions of the characteristic length for each geometry was chosen such that the cross-sectional area is the same for each geometry and that the pillar aspect ratio (height over diameter) is close to 3. Details of the geometry and optical

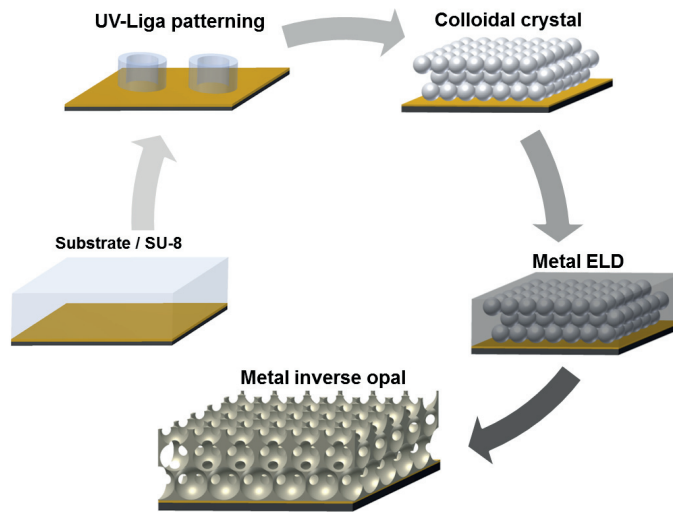


Figure 4.8 – Schematic of the process to obtain porous Ni inverse opals by dual templating.

micrographs of the resulting molds are shown in Figure 4.9.

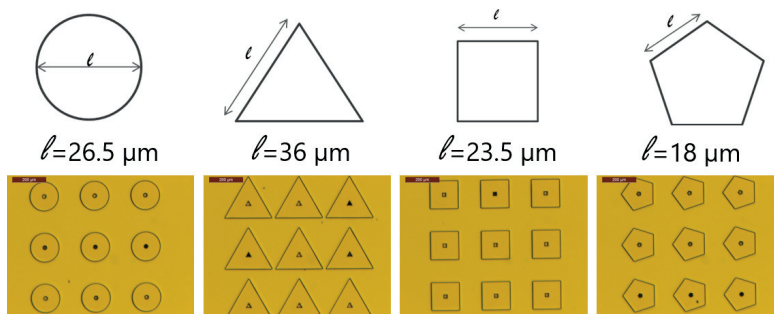


Figure 4.9 – Schematic of a) geometry of the pillar with characteristic length  $l$  and b) optical microscopy of the corresponding array of UV-LiGA molds.

### Microsphere lithography

After UV-LiGA photolithography, the UV-LiGA molds are filled with monodisperse PS spheres. This is done by dispersion of a colloidal solution (1-2wt%) at the surface of the LiGA molds. The sample is then placed in an oven at 60°C until the solvent is completely evaporated. The 3D colloidal crystal is formed by sedimentation and evaporation of the solvent in air. The sedimentation of several PS sphere diameters were investigated: 500 nm, 836 nm, and 2560 nm PS spheres. Varying the PS sphere diameter is a good way to control the ligament size. For 500 nm, 836 nm, and 2560 nm PS spheres, the ligament size measures 110 nm, 185 nm and

## 4.2. Effect of the ligament size in nc-Ni inverse opals

---

540 nm, respectively. The stability of the colloidal crystal is finally reinforced by annealing the sample at 96°C in air. In the ideal case, the PS spheres self-assembled into a perfect closed-pack structure with a theoretical packing density of 0.74. However, the actual packing depends on the packing quality of the PS spheres.

One of the most common methods to assess the quality of self-assembled monolayers and opals relies on image analysis by the fast Fourier transform (FFT). The Fourier transform of a perfect fcc pattern returns a hexagonal signature. On the other hand, the FFT returns a ring when the pattern is completely disordered. In between these two extreme cases, the FFT will be a combination of both the hexagonal and ring signature making quantification of the ordering difficult. Figure 4.10a-c show the SEM micropgraphs for three PS sphere diameters along with the corresponding FFT. It appears that structural organization increases with smaller PS spheres. For 500 nm PS spheres, a few large grains of closed-packed spheres are clearly visible with little defects. For 836 nm PS spheres, a crystalline structure is still visible but the number of vacancies and stacking faults increases. At last, the 2560 nm PS spheres show almost no long range organization. The difference in colloidal crystal quality is linked to the sedimentation rate. PS spheres with a large diameter have a larger sedimentation rate, which lets less time for the spheres to self-assemble into a perfect crystal. This image analysis technique provides an interesting way to compare two colloidal crystals but it does not provide a quantitative and qualitative information on the quality.

If one wants a quantitative way to compare several colloidal crystals, more advanced image analysis techniques need to be implemented. One of this technique is based on the radial distribution function (RDF) of the PS spheres. This technique was first applied to quantify the quality of porous alumina by Hillebrand et al. [108] but is also applicable to the packing of PS microspheres. The RDF  $g$  describes how density  $\rho$  of spheres varies as a function of distance  $r$  from a reference sphere. To compute the RDF of the SEM images shown in Figure 4.10, the coordinates of the PS spheres must be extracted. This was done by pre-processing the SEM images using the software *ImageJ*. The RDF for 500 PS spheres is shown in Figure 4.11a. This graphs shows the probability to find another sphere at a distance  $r$  of a reference sphere. The first peak position is located at a distance of 500 nm, corresponding to the distance between two close-packed spheres. In order to compare the organization of 500 nm, 836 nm

and 2560 nm PS spheres crystals, the RDF was normalized by the PS sphere diameter in Figure 4.11b. The peak position for a perfect fcc crystal are indicated by the dashed lines. The RDF of the 500 nm PS crystal is composed of multiple peaks of high intensity indicating a long-range ordering. On the contrary, the RDF of the 25600 nm PS crystal indicate a short range ordering with an amorphous like structure.

The coordinates of the PS spheres extracted from the SEM images can also be used to visualize the quality and orientation map of the crystal domains. A triangle mesh is created from the coordinates of the PS spheres. Then orientation angle of each triangle is computed and color-coded. Analysis of the SEM images in Figure 4.10 was performed with the *Matlab* software using an algorithm developed by Johnston-Peck et al. [109]. Examples of color-coded PS sphere crystals are shown on Figure 4.10d-f.

### Ni electrodeposition inside colloidal crystals

Galvanostatic pulse plating of nickel was conducted inside the dual template to achieve the Ni inverse opals. The deposition was performed in a nickel sulfamate electrolyte. A square-wave pulse of  $-80 \text{ mA.cm}^2$  was applied with on-time and off-time periods of 60 ms. A good wetting of the micro-porous template all the way down to the conductive substrate is key in achieving a uniform deposit. For that reason, the samples were vacuum impregnated with the Ni electrolyte before deposition. For details of Ni bath and plating conditions, refer to Section 2.2. Figure 6.3 shows SEM images of the Ni inverse opal film obtained on a Au-coated Si wafer with 500 nm pore size. The long range organization is clearly visible along three directions of observation. The fast Fourier transform of the corresponding SEM images confirms that the fcc structure remains after electrodeposition. Therefore the theoretical relative density of nickel inverse opals is 0.26, which means that 26% of the volume is made of Ni. The rest is the air contained in the pores.

Given the good results obtained for the Ni inverse opal films, the electrodeposition was then performed inside LiGA molds with or without PS sphere lithography. Representative SEM images of electrodeposited dense and porous Ni micropillars are shown in Figure 4.13. Good filling of the LiGA molds is observed for all cross-sections. The side walls of the pillar appear to

## 4.2. Effect of the ligament size in nc-Ni inverse opals

---

be smoothed and straight. Note that both dense and porous Ni micropillars were overgrown (deposition thickness exceeds the height of the LiGA molds). As a result, mushroom-shaped micropillars are formed (Figure 4.13f-h). The specimen were then mechanically polished to get a top flat surface (Figure 4.13a-d) necessary to get reliable mechanical properties.

### 4.2.2 Mechanical properties of as-deposited Ni inverse opals

The mechanical properties of the Ni inverse opal micropillars with 500 nm pore size and 2560 nm pore size were measured by *in situ* SEM nanoindentation using a 50  $\mu\text{m}$  diamond flat punch at a constant strain rate of  $10^{-3} \text{ s}^{-1}$ . Dense Ni micropillars were also compressed to assess the mechanical properties of the bulk nanocrystalline Ni. A minimum of 4 pillars per samples were tested. The resulting stress-strain curves are presented in Figure 4.14. Representative images of the sample before and after compression are shown in Figure 4.15.

The bulk yield strength of the nanocrystalline Ni dense pillars is 1179 MPa. The upper limit of the theoretical strength of a porous metal is  $\sigma = \sigma_s \times \rho^*$  with  $\rho^*$  is the relative density. Considering a relative density of 26% and  $\sigma_{Ni}=1179$  MPa, the theoretical strength for a Ni inverse opal should be 306 MPa. The actual measured yield strengths for the Ni inverse opal micropillars with 500 nm pore size and 2560 nm pore size are 168 MPa and 259 MPa, respectively. The strength of a porous metal should be the same for a given relative density. However, we observe a difference of 54% in strength between the two porous structures. This discrepancy indicates a potential size effect.

### 4.2.3 Is the strength the result of the ligament size?

At the beginning, we made the assumption that the mechanical properties of Ni inverse opals are driven by the ligament size; as the ligament size decreases, the strength increases owing to the strengthening mechanism induced by the extrinsic size effect in metal. Given that the ligament size is proportional to the PS sphere size, the size of the ligament in Ni inverse micropillars obtained with 2560 nm and 500 nm PS spheres is  $\approx 110$  nm and  $\approx 540$  nm, respectively. Based on that, the mechanical properties of Ni inverse opals with 500 nm pore size should outperform the one with 2560 nm pore size. However, the experiments show the

opposite. Several limitations have to be pointed out: 1) the grain size as-deposited is actually smaller than the ligament size and therefore there might be a complex interaction between the two; 2) the pore structure might not be perfect (holes, non porous) and thus change the actual density of the micropillar. The second point was confirmed by observing a FIB cross-section of the porous micropillars (Figure 4.16). The electrodeposition inside the micropillar is not as uniform as expected. Some areas of the micropillar with 500 nm pores are empty while some others are dense. For the micropillar with 2560 nm pores, the density appears to be higher. Based on the analysis of the cross-section, the actual relative density is taken as 30% for the micropillar with 500 nm pores and 50% for the micropillar with 2560 nm pores. Those are conservative estimates. Using the actual value of relative density instead of the theoretical one explains part of the measured difference in strength between the two samples. However, it is not sufficient to account for the entire difference.

### 4.3 Summary

In this chapter, the effect of the external dimensions on the mechanical properties and deformation behavior of micro-cellular metals were explored. The failure mechanism of NiB/polymer hybrid micro-architectures was tuned by the NiB thickness. Given its amorphous nature, NiB undergoes a brittle to ductile transition at small scale. The mechanical properties of nanocrystalline Ni inverse opals were investigated for two different ligament sizes. The comparison of the mechanical properties for both ligament sizes indicates a potential extrinsic size effect.

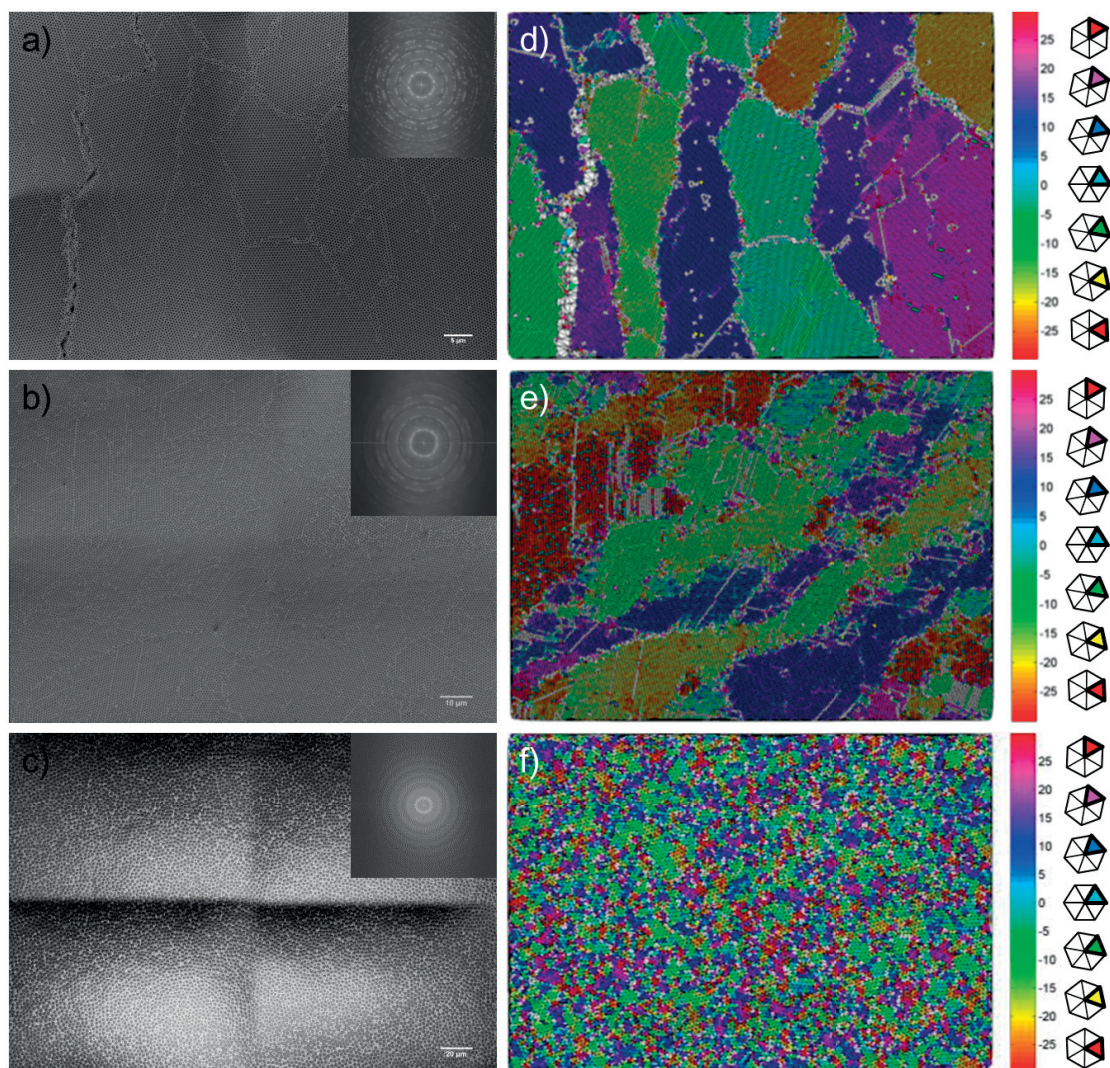


Figure 4.10 – SEM images of the polystyrene colloidal crystals for a) 500 nm, b) 836 nm, and c) 2560 nm PS spheres. The corresponding FFTs are shown in all cases. Color-coded triangular mesh according to orientation angle of the corresponding SEM micrographs (d-f).

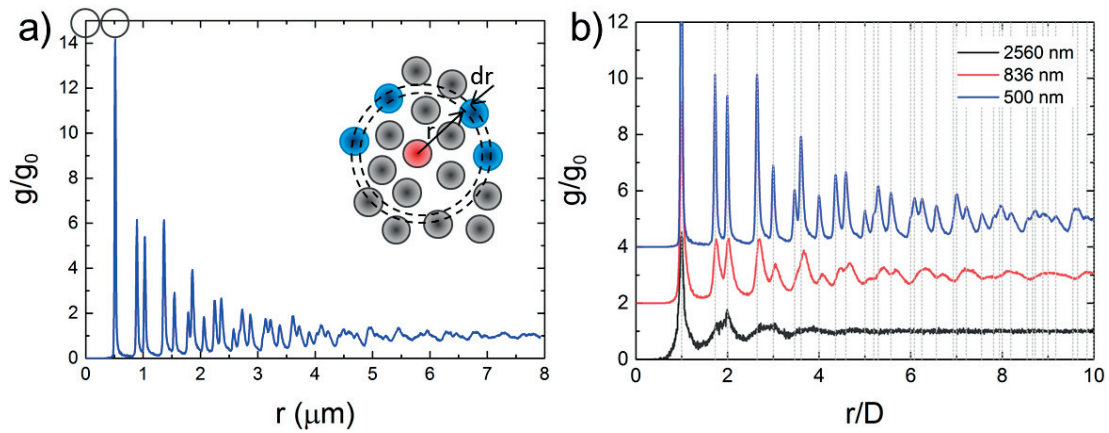


Figure 4.11 – a) Radial distribution function for 500 nm spheres. b) Normalized radial distribution function comparing 500 nm, 836 nm, and 2560 nm PS colloidal crystals.

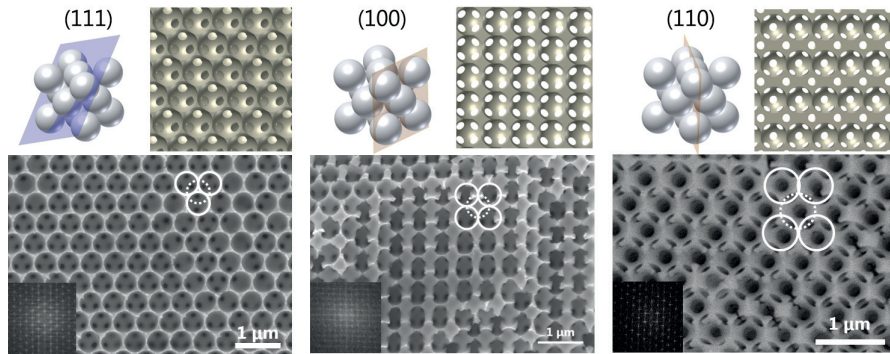


Figure 4.12 – SEM images of Ni inverse opal produced with 500 nm polystyrene spheres seen along a) 111, b) 100, and c) 110 directions. The FCC unit cell with the corresponding plane of interest is depicted. FFTs are shown in all cases. The windows interconnecting the air cavities with those in the underlying plane can be seen: three for 111 faces, four in the case of 100, and five for 110.

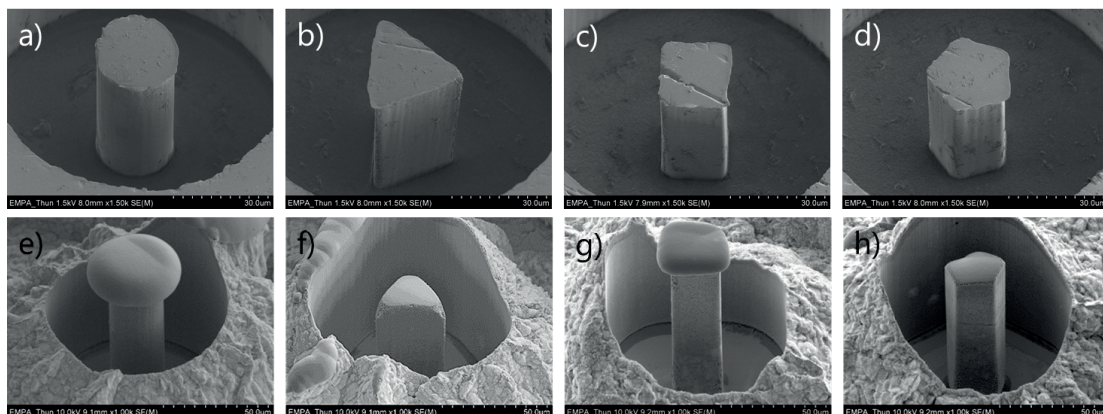


Figure 4.13 – SEM images (a-d) dense Ni micropillars and (f-h) as-deposited porous Ni micropillars obtained by UV-LiGA and PS sphere lithography.



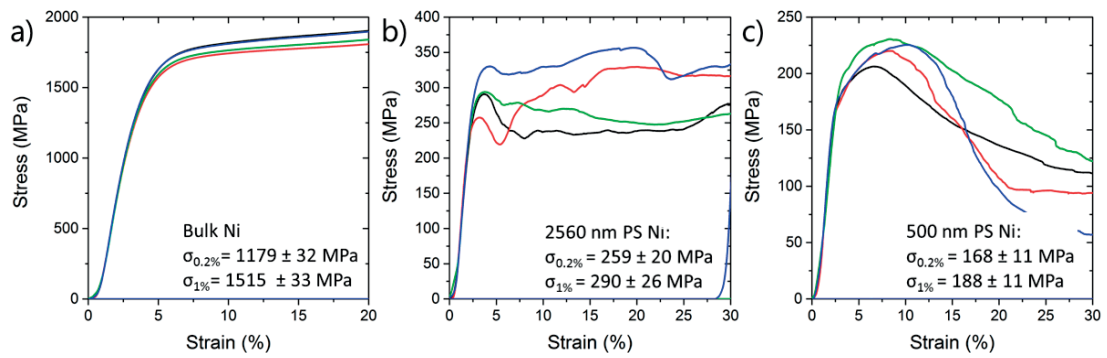


Figure 4.14 – Stress-strain curves of a) dense Ni micropillars and porous Ni micropillars with b) 2560 nm and c) 500 nm pore size.

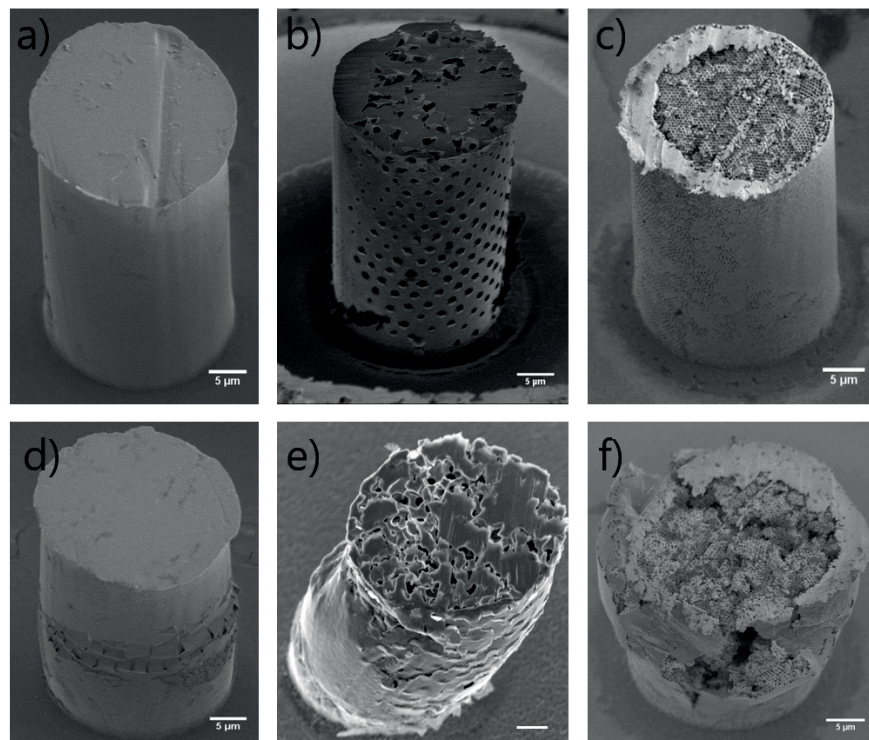


Figure 4.15 – Electrodeposited Ni micropillars before and after micrompression with dense a) dense Ni with b) 2560 nm and c) 500 nm pore size.

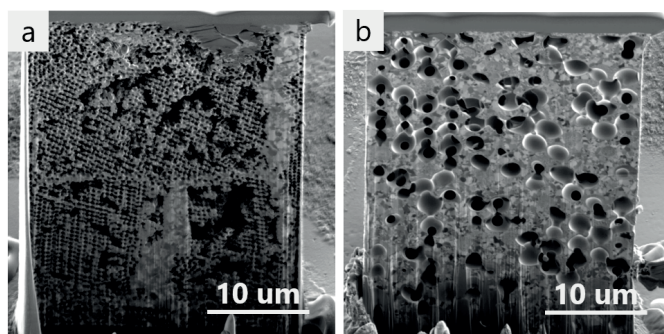


Figure 4.16 – FIB cross-section of a Ni inverse opal micropillar with a) 500 nm and b) 2560 nm pore size.

# 5 Investigation of the architecture effect on the mechanical properties

In previous chapters, we examined the impact of the intrinsic and extrinsic size effects on the mechanical properties of both nanocrystalline Ni and amorphous NiB. Another crucial parameter, if not the most crucial one, is the geometry of the cellular structure itself. The geometry of the cellular structure or architecture modifies the relative density, which in turn changes the mechanical properties through different scaling laws. In this chapter, we will therefore review the influence of the cellular geometry on the mechanical properties and on the energy absorption capability of advanced NiB/polymer hybrid micro-architectures.

## 5.1 NiB/polymer hybrid micro-architectures

### 5.1.1 Strength and stiffness *vs.* architecture

Figure 5.1a compares the engineering stress-strain curves of design A, B and C for the same NiB coating thickness. These three architectures share the same base cubic unit cell and differ only by the addition of bracings. It is clear that design A outperforms design B, which outperforms design C, both in terms of maximum compressive strength and Young's modulus. For instance, the maximum compressive strength of design B is 2.8 times the one of C for a density multiplied only by 1.5. The same correlation was observed between design A and B. This demonstrates a beneficial effect on strength and stiffness of the bracings within a cubic unit cell despite the increased density. Addition of bracings within the cubic unit cell also improves the reproducibility of microcompression tests and lowers the sensitivity to external

## Chapter 5. Investigation of the architecture effect on the mechanical properties

uncertainties such as geometrical defects, coating uniformity, or misalignment. The hexagonal unit cell of structure D outperforms cubic unit cell of structure C.

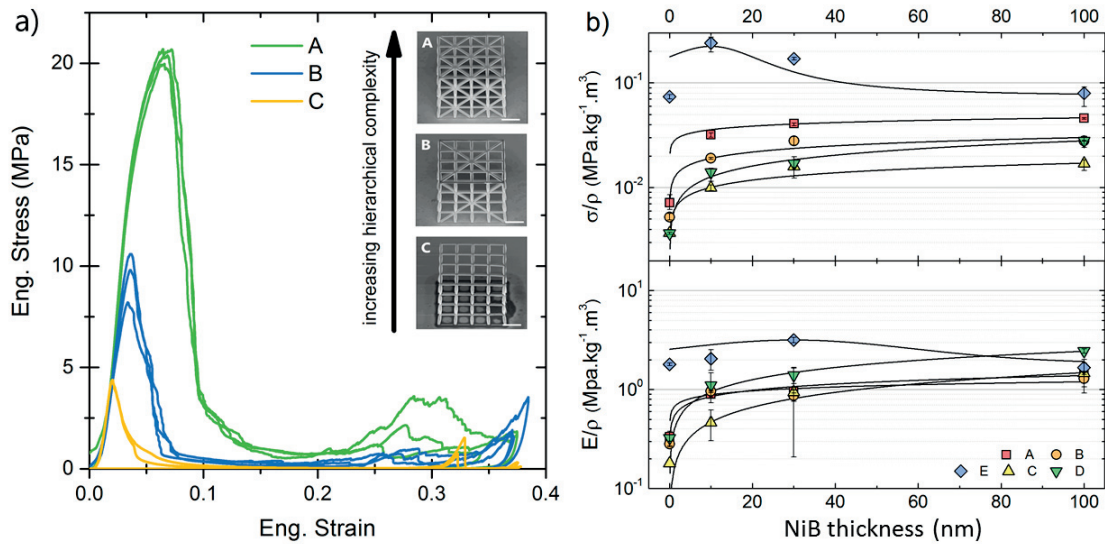


Figure 5.1 – Stress-strain curves for 100 nm NiB coating as a function of the architecture. b) Specific strength  $\sigma/\rho$  and modulus  $E/\rho$  of the micro-architectures as a function of the NiB coating.

Unlike the previous micro-architectures, the honeycomb structure E, demonstrates a different failure mechanism under uniaxial loading. In the microlattices, after the initial peak strength a significant post-yield softening is observed due to the plastic buckling or brittle collapse of struts [17]. On the contrary, a uniform plateau stress is observed in the uncoated honeycomb structure after the elastic regime (Figure 4.3f). The plateau stress value is almost equal to the maximum compressive strength and stays constant for strains up to 0.4. Beyond that strain level, the stress increases again indicating the densification of the structure. The area under the plateau regime represents the capacity of the honeycomb to absorb a large amount of energy. Both stiffness and strength are an order of magnitude higher than the other designs but so is the density. That is the reason why we observe a decrease in specific strength and stiffness with thicker NiB deposits in 5.1b.

### 5.1.2 Energy absorption *vs.* architecture

In this section, the energy absorption capability of the micro-architectures is examined. Micro-architected materials are of interest because they can sustain large amounts of deformation under compression despite their low density. The energy is dissipated through bending, buckling or fracture of the struts. Therefore the plateau stress is a good indicator of the energy dissipation mechanism. The higher the plateau stress of a structure, the larger is its energy absorption capability. The plateau stress was determined by Liu et al. [110],

$$\sigma_{pl} = \frac{1}{\varepsilon_{\alpha} - \varepsilon_{peak}} \int_{\varepsilon_{peak}}^{\varepsilon_{\alpha}} \sigma(x) d\varepsilon \quad (5.1)$$

from the strain at peak load,  $\varepsilon_{peak}$ , up to the strain  $\varepsilon_{\alpha}$  as shown in Figure 5.2.

Figure 5.2b shows the variation of the plateau stress for each sample. The plateau stress is primarily governed by the architecture geometry. However, since the preferred deformation mode is dependent on the layer thickness, there is no linear increase of the plateau stress with the coating thickness. At zero and thin NiB coating thicknesses, the micro-architectures failed by buckling while they failed by crushing for 100 nm-thick NiB coating. Another way to assess the energy absorption capability of the micro-architectures is by measuring the absorbed energy:

$$W(\varepsilon) = \int_0^{\varepsilon_{\alpha}} \sigma(\varepsilon) d\varepsilon. \quad (5.2)$$

The absorbed energy is the area under the stress-strain curve up to a given strain,  $\varepsilon_{\alpha}$ . As observed in Figure 5.2c, the energy dissipated during compression increases with the coating thickness in a similar fashion as the plateau stress. Finally, an energy absorption efficiency approach is applied to compare the energy absorption capability of the different micro-architectures. The efficiency is defined as the ratio of the absorbed energy by the micro-architecture over the energy adsorbed by an ideal energy absorber [111] (area shaded in light gray in Figure 5.2a),

$$\eta(\varepsilon) = \frac{1}{\varepsilon_{\alpha} \sigma_{peak}} \int_0^{\varepsilon_{\alpha}} \sigma(\varepsilon) d\varepsilon \quad (5.3)$$

where  $\sigma_{peak}$  is the stress at peak load. The best energy efficiency is achieved for the honeycomb structure E ( $\eta=70-90\%$ ) because of the high value of plateau stress. The efficiency of the micro-lattices A, B, C and D ranges from 45% down to 10%. The efficiency decays continuously with the NiB thickness for micro-lattice structures as the post-yield softening (the ratio of peak stress to plateau stress) increases with an increase in catastrophic failure. However, the rate of decay is lower by a factor of 3 for structure A when compared to structures B, C and D, which shows that the energy absorption capability is controllable by design and that a fully triangulated structure outperforms other micro-lattices.

A final approach, which takes into account the shape of the stress–strain curve and which is independent of the bounds of integration, has been proposed by Maiti and co-workers, called energy absorption diagrams [112, 113]. The energy absorption diagrams are constructed by plotting the energy absorbed per unit of volume up to a given strain (by integration of the stress–strain curve) against the stress at that given strain. The energy absorption diagrams for each micro-architecture are presented in Figure 5.3a-e. The best absorbing material is defined as the one that absorbs the most energy up the maximum peak stress. It is observed that maximum transmitted stress and absorbed energy increase with the NiB thickness. Unlike stochastic foams, micro-architected structures absorb most of their energy in the linear-elastic regime (*i.e.* linear stored energy) because of the post-yield softening which results in lower plateau stress. Depending on the NiB coating thickness and the micro-architecture design, the micro-architectures exhibit not only one plateau stress but also multiple plateau stresses. For comparison, the micro-architectures with similar densities ( $236\pm 7 \text{ kg.m}^3$ ) are depicted in Figure 5.3f along with polyethylene foam [112] ( $360 \text{ kg.m}^3$ ) and an aluminum foam [114] ( $300 \text{ kg.m}^3$ ). For a given density, a wide range of energy absorption responses is possible for composite micro-architectures as reported by Schaedler et al. [111]. Figure 5.3f also shows that the micro-architectures can compete with and even outperform metallic or polymeric stochastic foams in terms of energy absorption capability.

## 5.2 Summary

In this chapter, we investigated the influence of the architecture on the mechanical properties of 3D cellular solids. It was shown that the energy absorption behavior of NiB/polymer hybrid

micro-architectures can be controlled by the architecture topology. For a given material density, it is possible to design 3D architectures with different levels of plateau stress and/or multiple plateau stresses unlike stochastic foams which show an homogeneous plateau stress.

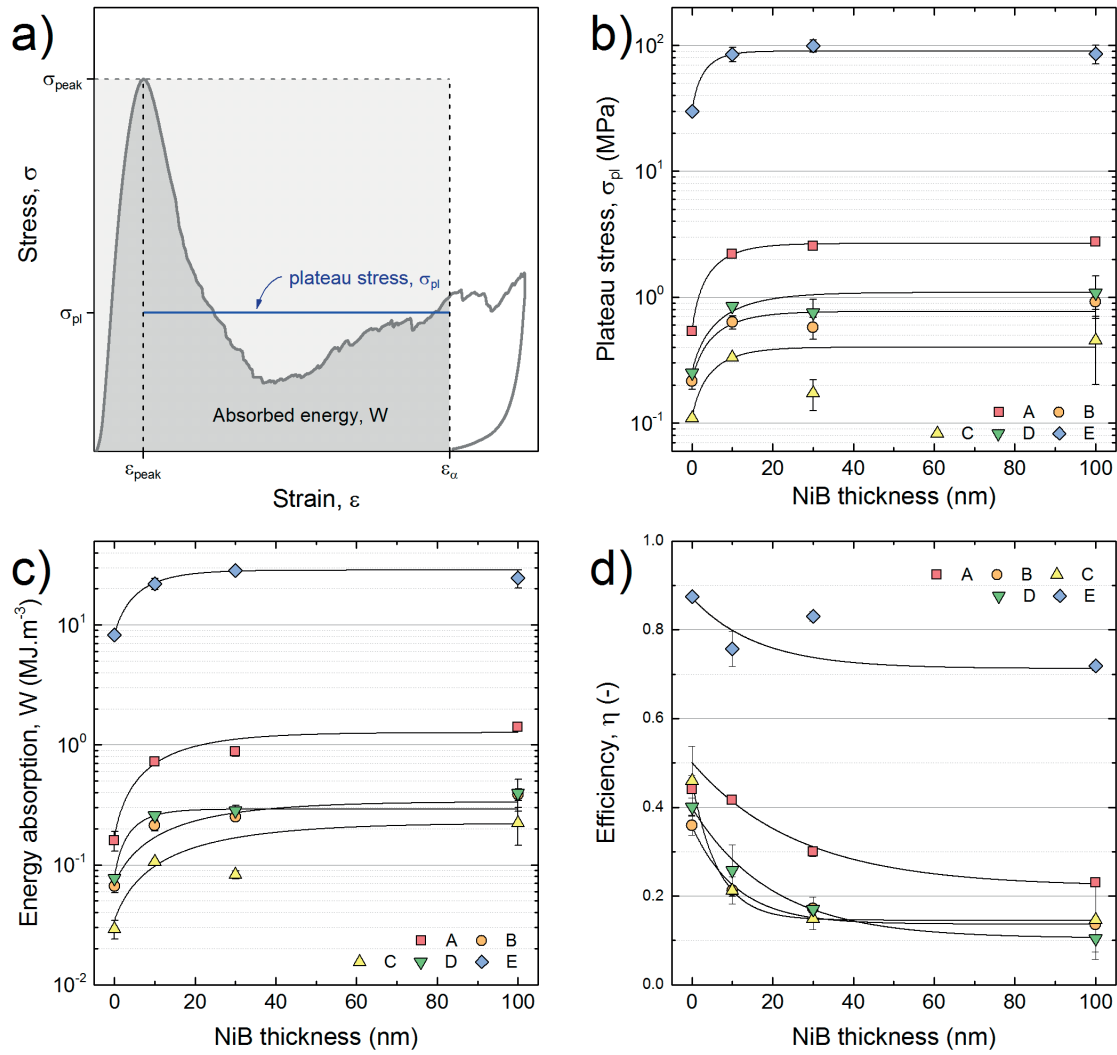


Figure 5.2 – a) Typical stress-strain curve of micro-architected structures, showing the important energy parameters and the energy dissipated by a theoretic ideal absorber (area shaded in gray). Variation of b) the plateau stress, c) the absorbed energy per unit volume and d) the energy absorption efficiency versus NiB thickness for each microarchitecture. Solid lines are guidelines for the eyes.



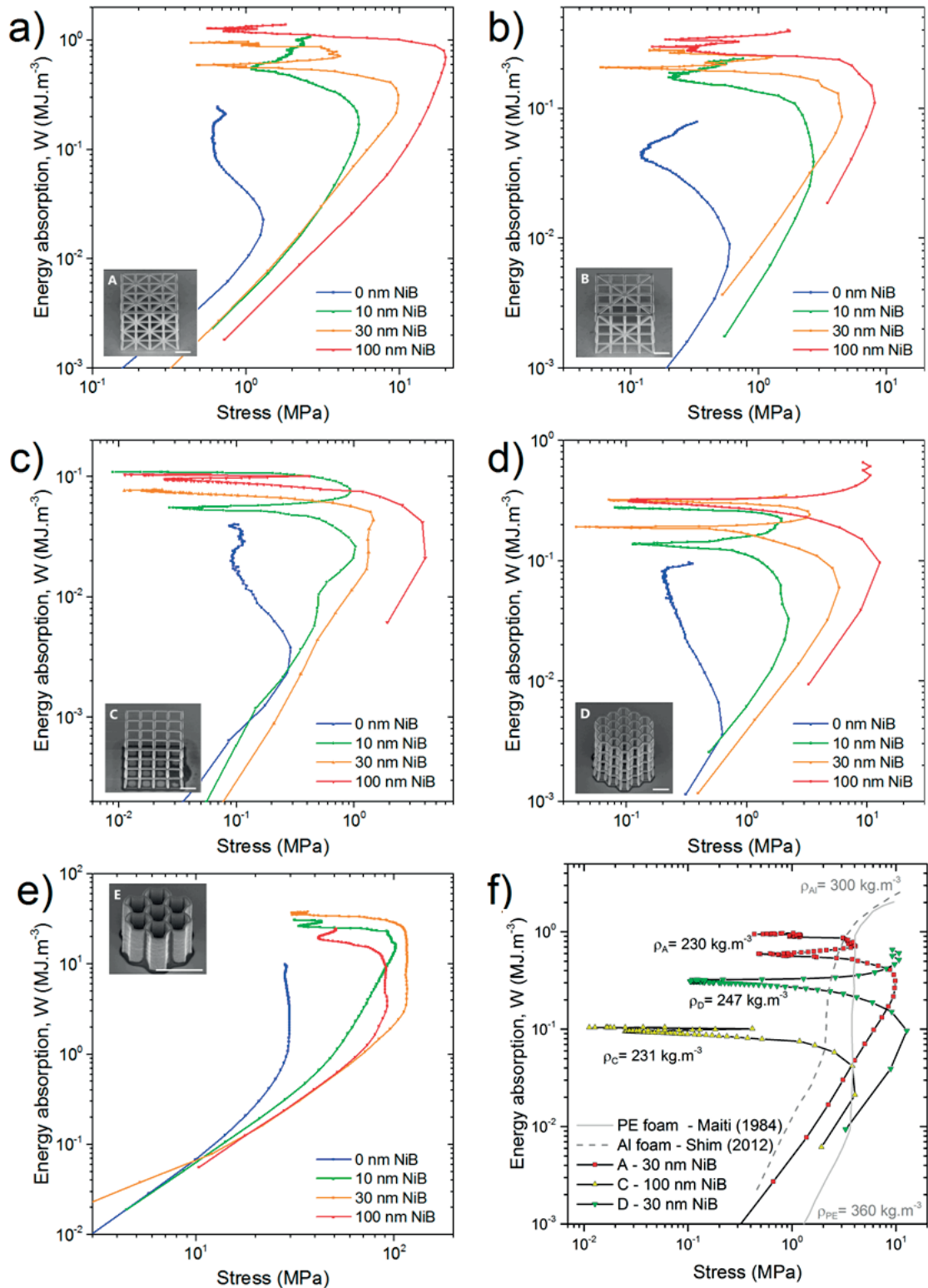


Figure 5.3 – (a-e) Energy absorption diagrams for each NiB/polymer hybrid micro-architectures. f) Energy absorption diagrams for micro-architectures with similar density. Comparison with a PE foam and Al foam [112, 114].



## 6 Combination of size effects

Thus far, we have examined the size effects independently, starting with the microstructure, continuing with the external dimensions, and finally finishing with the architecture. In this chapter, we look at the mechanical properties and deformation behavior of 3D micro-cellular metals when several size effects are combined together.

### 6.1 Controlling the buckling behavior with ductile to brittle transition in NiB/polymer micro-architectures

While the micro-architectures fail either by buckling or by crushing, failure modes are directly related to the thickness of the NiB film. However, the mechanical properties of the micro-architectures result from the combination of both the polymeric template and the NiB coating. In order to understand the underlying effect of the compliant elastic core and predict the dominant failure mode, a simple buckling model for cylindrical shells filled with an elastic core was considered as follows [115]. Assuming the core to act as an elastic foundation, the axisymmetric buckling stress can be obtained as:

$$\sigma_{cr} = \frac{E_{NiB} t}{a} f \quad (6.1)$$

## Chapter 6. Combination of size effects

where  $t$  is the NiB coating thickness,  $a$  is the mean radius of a strut and  $f$  is defined as:

$$f = \left[ \frac{1}{12(1 - \nu_{NiB}^2)} \frac{(a/t)}{(\lambda_{cr}/t)^2} + \frac{(\lambda_{cr}/t)^2}{(a/t)} + \frac{3}{(3 - \nu_{pol})(1 + \nu_{pol})} \frac{E_{pol}}{E_{NiB}} \left( \frac{\lambda_{cr}}{t} \right) \left( \frac{a}{t} \right) \right] \quad (6.2)$$

and  $\lambda_{cr}$  is the buckling half-wavelength divided by  $\pi$ :

$$\lambda_{cr} = \frac{L}{m\pi} \quad (6.3)$$

where  $L$  is the length of the cylindrical shell and  $m$  is the buckling mode (Figure 6.1-a and b).

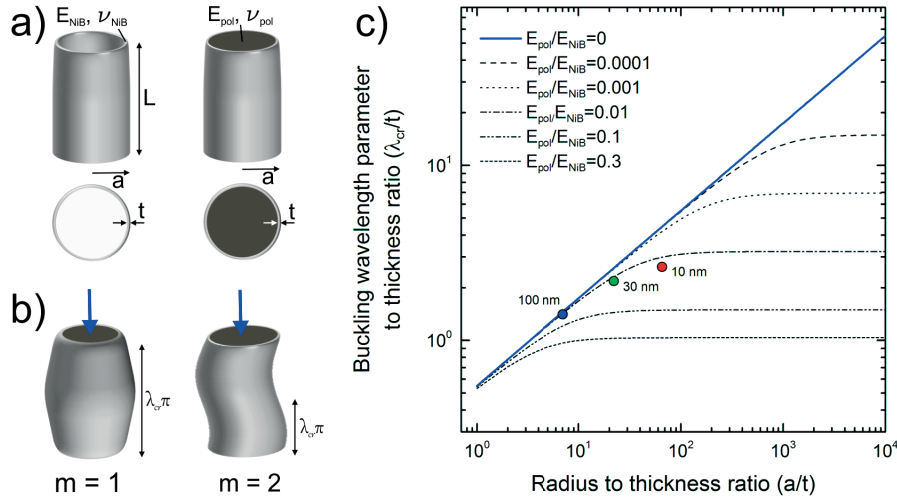


Figure 6.1 – Model geometry parameters for hollow cylindrical shell and hollow cylindrical shell filled with a compliant core a) before and b) after buckling. c) Buckling wavelength parameter plotted as a function of the radius to thickness ratio. The values for the 3 NiB thicknesses are indicated on the plot. Adapted from Karam and Gibson [115]

The values of  $\lambda_{cr}/t$  are plotted against the radius to thickness ratio  $a/t$  for various  $E_{NiB}/E_{pol}$  in Figure 6.1c. For low  $a/t$  ratios, the compliant core has little effect on the mechanical response and the NiB coating behaves like a hollow cylindrical shell (solid blue line in Figure 6.1). On the other hand, for large  $a/t$  ratios, the compliant core acts as an elastic foundation. Using the properties of the NiB coating,  $E_{NiB} = 250$  GPa and  $\nu_{NiB} = 0.3$ , and the properties of the IP-Dip polymer,  $E_{pol} = 2.2$  GPa and  $\nu_{pol} = 0.4$  [116], the buckling wavelength parameter to thickness ratio  $\lambda_{cr}/t$  calculated for  $t=10$  nm,  $t=30$  nm, and  $t=100$  nm are presented in Figure 6.1. When  $t=100$  nm, the data point lies on the solid line indicating that the core is not stiff enough to improve the load-bearing capability and that the buckling stress is determined by the

## 6.2. Combination of intrinsic and extrinsic size effects in inverse opals

buckling stress of the hollow shell. In the case of a 10 nm-thick NiB coating, the polymer core is sufficiently stiff to support the outer shell, which enhances the buckling stress. The micro-architectures with 30 nm NiB layer lie in transition regime between the behavior of the hollow shell and that of the shell with a compliant core.

Hence, the diameter to thickness ratio is key in controlling the deformation mode in hybrid cellular materials. At a low NiB film thickness, the analytical model shows that the micro-architecture is prone to buckling. At the same time, the NiB film is ductile for this thickness. Resilient micro-architectures under large deformation can be designed.

## 6.2 Combination of intrinsic and extrinsic size effects in inverse opals

To distinguish whether the strength is dominated by the grain size or the ligament size in Ni inverse opals, annealing tests were performed to increase the grain size. The mechanical performances of the annealed samples were tested and compared to as-deposited samples.

### 6.2.1 Annealing tests of Ni inverse opals

The mean crystallite size of the electrodeposited nanocrystalline Ni films in as-deposited condition were found to measure 28 nm using XRD. This means that each ligament in the Ni porous micropillars with 500 nm pore size and with 2500 nm pore size contains 4 and 20 grains, respectively. It is likely that the mechanical properties of the Ni inverse opals are a combination of the strengthening effect from the grain size and from the ligament size. To distinguish both effects, it was decided to anneal the samples to increase the grain size.

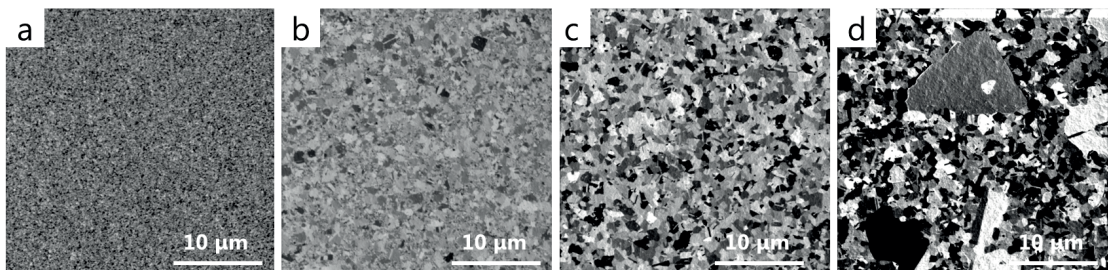


Figure 6.2 – FIB images of a) as-deposited nanocrystalline Ni films and annealed 30 minutes at b) 300°C c) 400°C, and d) 500°C.

## Chapter 6. Combination of size effects

---

Annealing tests were first performed on dense Ni films ( $\approx 80 \mu\text{m}$ ) to find the optimum annealing conditions for uniform grain growth. Figure 6.2 shows ion contrast channeling images of the top surface. Up to  $400^\circ\text{C}$ , the grains grow homogeneously. Beyond that temperature, grains of several microns inside a matrix of fine grains are observed. This bimodal grain growth is sometimes observed in nanocrystalline electrodeposited metals and is referred to as abnormal grain growth [117]. An annealing temperature of  $250^\circ\text{C}$  for 1hr was chosen to anneal Ni inverse opal samples in order to promote uniform grain growth while limiting the residual stress induced by the thermal mismatch between the Si wafer and Ni.

### 6.2.2 Mechanical properties as a function of annealing time

The mechanical properties of the Ni inverse opal micropillars were measured after 1hr, 2hr, 4hr, 8hr and 16hr of annealing at  $250^\circ\text{C}$ . The yield strength is plotted as a function of the number of annealing hours at  $250^\circ\text{C}$  in Figure 6.3. The yield strength decreases with annealing time for the two pore sizes. The grains grow with annealing time, thus reducing the number of grains per ligament. If the average grain size is larger than the ligament size, then there are no more grain boundaries inside the ligament. In this case, the strength is expected to be controlled only by the ligament size. Owing to the extrinsic size effect "smaller is stronger" in single crystal metal, the porous micropillar with 500 nm PS is expected to outperform the one with 2560 nm PS. Yet our results do not show this cross-over in strength. One possible explanation is that the annealing temperature does not provide sufficient thermal activation energy to further increase the grain size. Grain size determination using XRD after 16hr at  $250^\circ\text{C}$  revealed a mean grain size of 200 nm for both samples. It is interesting to note that the effect of annealing on dense nanocrystalline Ni is much more significant. The yield strength of Ni is divided by 2, whereas the strength of the Ni inverse opals is reduced by only 30% as reported in Table 6.1.

Table 6.1 – 0.2% offset yield strength (MPa),  $\sigma_{0.2\%}$ , of porous Ni inverse opals in as-deposited and annealed conditions.

	As-deposited	Annealed
Bulk Ni	$1179 \pm 32$	$603 \pm 83$
500 nm PS	$168 \pm 11$	$124 \pm 6$
2560 nm PS	$259 \pm 20$	$198 \pm 6$

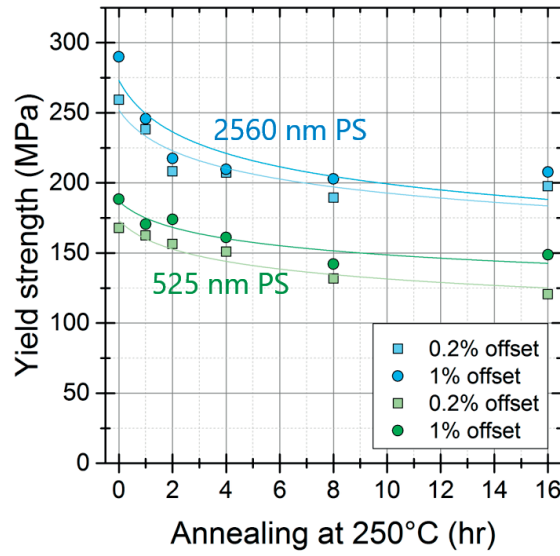


Figure 6.3 – Yield strength of Ni inverse opals as a function of the annealing time at 250°C for 500 nm and 2560 nm PS spheres.

### 6.2.3 Reverse approach to measure the strength

According to Gibson and Ashby [113], the yield strength  $\sigma$  of an open-cell foam can be expressed as a function of the relative density  $\rho/\rho_s$  according to:

$$\sigma = 0.3\sigma_s \left( \frac{\rho}{\rho_s} \right)^{3/2} \quad (6.4)$$

where  $\sigma$  and  $\rho$  are the yield strength and density of the foam whereas  $\sigma_s$  and  $\rho_s$  denote the properties of the bulk. Some researchers suggested that this relation could be used to back calculate the strength inside the ligament [30]. In this case,  $\sigma_s$  in equation 6.4 is assumed to be size dependent. This approach was applied to our samples and the results are presented in Table 6.2. According to this approach, the strength of Ni ligaments vary from 1.8 GPa to 3.4 GPa. The ligament strength of Ni inverse opals with 500 nm pore size (2.5-3.4 GPa) surpasses the of of Ni inverse opals with 2560 nm pore size (1.9-2.4 GPa). This is consistent with the fact that smaller ligament size yields larger strength. On the other hand, the ligament strength of annealed Ni inverse opals with 500 nm pore size and as-deposited Ni inverse opals with 2560 nm pore size is similar despite different ligament sizes. Part of the observed difference may be attributed to the difference in grain size (28 nm vs. 200 nm) due to the annealing treatment. The present results indicate that looking at the ligament size only or the grain size only is not

## Chapter 6. Combination of size effects

sufficient to explain the mechanical properties of Ni inverse opals.

Table 6.2 – Grain size, ligament size, relative density, measured yield stress and calculated ligament strength for Ni inverse opals with 500 nm pore size or 2560 nm pore size. A stands for annealed.

	Grain size (nm)	Ligament size (nm)	Relative density	Measured yield stress (MPa)	Calculated ligament strength (MPa)
Ni 500nm	28	≈110	≈0.3	168 ± 11	3408 ± 223
Ni 500nm A.	200	≈110	≈0.3	124 ± 6	2515 ± 122
Ni 2560nm	28	≈540	≈0.5	259 ± 20	2442 ± 189
Ni 2560nm A.	200	≈540	≈0.5	198 ± 6	1867 ± 57

### 6.2.4 Comparison with other materials from the literature

The method presented in the previous section provided a way to calculate the theoretical bulk strength within a ligament for each porous structure. On the other hand, the mechanical results from the micropillar compression of the Ni inverse opal structures indicate that the strength of such structures depends on the grain size and ligament size. However, the exact contribution of each effect is not clear. In an attempt to clarify this issue, the strength of the ligament is plotted in Figure 6.4 and compared to values from the literature.

Figure 6.4a shows the yield strength of the Ni porous inverse opals plotted as a function of grain size. The results are compared to Ni samples with various grain size [42, 92, 118–120, 117, 121–123]. The strengths measured for dense Ni pillars in as-deposited and annealed conditions fit well with the literature data. The mechanical properties of the Ni inverse opals outperform the one from the literature with similar grain size.

Figure 6.4b shows the critical resolved shear stress (CRSS) of the Ni porous inverse opals as a function of sample size or ligament size. The CRSS stress corresponds to the stress required to initiate slip inside a single crystal. The CRSS value is a materials constant and can therefore be compared with single crystals with varying external dimensions. The CRSS strength of single crystal Ni was calculated by dividing the measured yield stress by the Schmid factor corresponding to the loading direction. The CRSS of Ni foam was obtained by dividing the ligament strength by the Taylor factor ( 3.06) given that the microstructure is polycrystalline. The results are compared to single crystal Ni with various orientations [55, 124, 125], single



## 6.2. Combination of intrinsic and extrinsic size effects in inverse opals

crystal nanowires [126] and molecular dynamics simulations [127]. The slope of the best fit for the CRSS is given by the exponent  $n - 0.58$ . If we take the ligament size as the driving parameter for the strength, the Ni inverse opals show much higher CRSS than their single crystal counterparts.

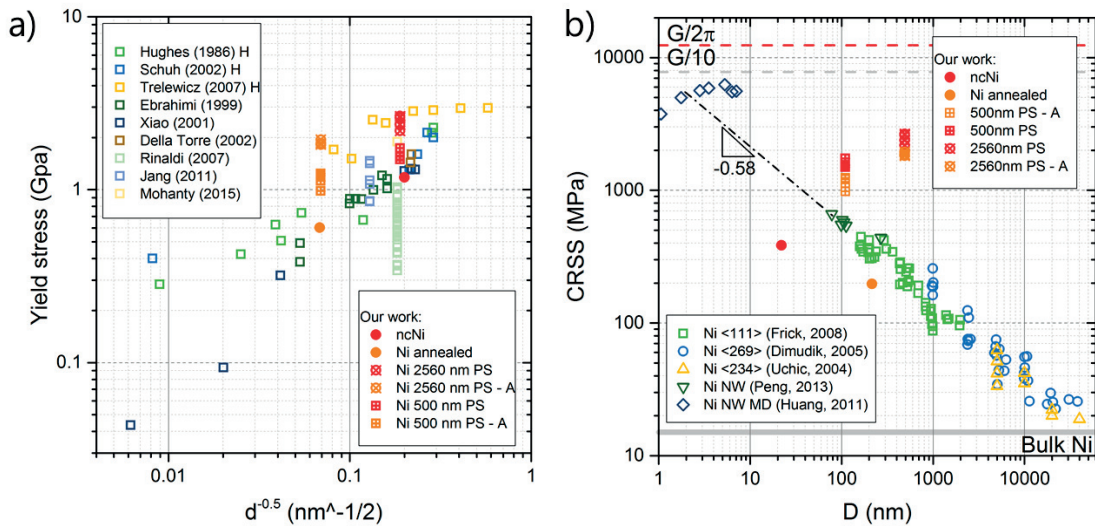


Figure 6.4 – Comparison of our mechanical results with data from the literature considering only the extrinsic size (ligament) or only the intrinsic size (grain) effect.

### 6.2.5 Summary

In this chapter, we investigated the complex interaction of size effects for two material systems:

1. In NiB/polymer micro-architectures, the cellular structure interacts with the brittle-to-ductile transition in the amorphous NiB film to control the overall deformation behavior of the micro-architectures.
2. The mechanical properties of Ni inverse opals indicate that grain size and ligament size related to each other in a non trivial way. The strength in Ni inverse opals decreases with annealing for both pore sizes but no cross-over in strength was observed between both pore size when the grain size exceeds the ligament size.

In conclusion, the complex interactions between the different length scales and the microstructure are not yet understood. Nevertheless, this work clearly shows that significantly improved

## **Chapter 6. Combination of size effects**

---

mechanical properties of nickel cellular structures can be achieved by a tailored combination of extrinsic and intrinsic size effects.

## 7 General discussion

Historically, the scaling laws that describes the mechanical properties of cellular metals were developed for bulk stochastic polymeric and metallic foams by Ashby [23]. However, the scaling laws do not account for the potential size effects occurring in tailored periodic metal foams and micro-lattices. The present chapter addresses this question. First the mechanical properties of the nickel inverse opals and NiB/polymer hybrid micro-lattices are compared to current scaling laws. The mechanical results are also presented in a broader perspective, with comparisons from the literature. Finally, the development of new models encompassing the size effects that we studied in this thesis is discussed.

### 7.1 Comparison with other materials

#### 7.1.1 Scaling laws for Ni inverse opals

Models for the compressive properties of random foams indicate that that open-cell foams should have lower specific strength than closed-cell foams. The mechanical properties of the studied Ni inverse opals are plotted against the relative density in Figure 7.1. On that plot, the scaling laws for an open- and closed-cell foam are indicated. The scaling law for an open-cell porous metal structure is given by:

$$\frac{\sigma}{\sigma_s} = 0.3 \left( \frac{\rho}{\rho_s} \right)^{3/2} \quad (7.1)$$

## Chapter 7. General discussion

The upper bound is then given by a closed-cell foam:

$$\frac{\sigma}{\sigma_s} = 0.3 \left( \frac{\rho}{\rho_s} \right)^2 + 0.44 \left( \frac{\rho}{\rho_s} \right) \quad (7.2)$$

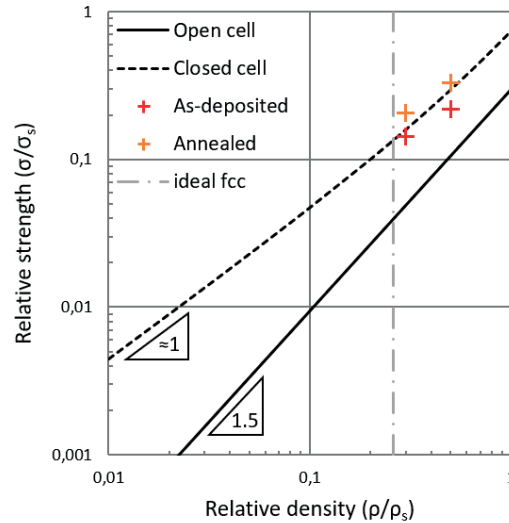


Figure 7.1 – Material property plot of strength versus density for our Ni inverse opals with current scaling laws.

Figure 7.1 shows that our samples perform better than the predicted value for an open cell foam. The data points actually lie close to the dashed line representing the scaling law for closed-cell foams, as prescribed by Equation 7.2. The additional strength of metallic closed-cell foams is provided by the cell wall and the gas pressure inside the unit cell but, in practice, the specific strength of closed-cell foams is similar to that of open cell foams due the presence of defects in the cell walls. The enhanced specific strength of Ni inverse opals is therefore attributed to a combination of the regular porous structure and the potential intrinsic and extrinsic size effect. However, the current results does not allow to quantify the influence of each parameter on the mechanical properties.

### 7.1.2 Scaling laws for 3D metal-polymer hybrid micro-architectures

Ashby et al. derived scaling laws for foams and microlattices as a function of the topology and deformation mechanism. When plotting the relative density versus the relative modulus or

strength, the mechanical performances can be expressed as follows:

$$\frac{E}{E_s} = C \left( \frac{\rho}{\rho_s} \right)^n \quad (7.3)$$

where the subscript  $s$  refers to the solid material,  $C$  is a constant related to the micro-architecture geometry and  $n$  is an exponent characteristic of the deformation mode. The relative density and relative strength are plotted in Figure 7.2. The relative Young's modulus varies with the square of relative density. This scaling indicates bending-dominated behaviour. The constant is equal to  $C \approx 1.03$ , which is a typical value for this deformation mechanism. The scatter is larger for the relative strength. Overall the relative strength scales with  $\rho/\rho_s^{1.5}$ , as expected for open-cell foam.

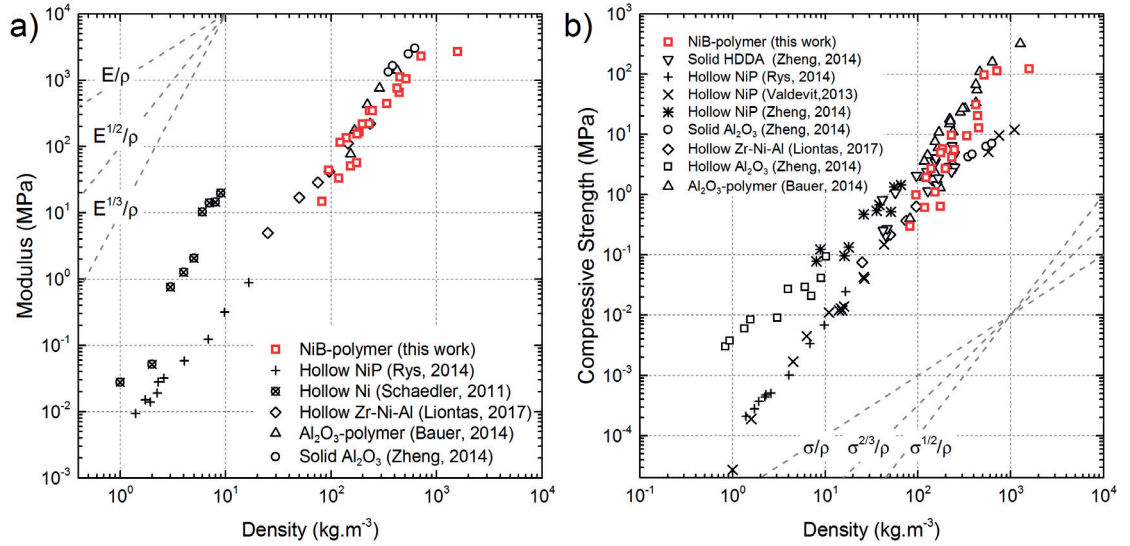


Figure 7.2 – Material property plot of a) elastic modulus and b) strength versus density for our NiB/polymer hybrid micro-lattices (red squares) compared with other micro-lattices from literature. Data are from references [11, 16, 35, 15, 13, 128]

When compared to other 3D micro-architectures, the amorphous NiB/polymer hybrid micro-lattices show comparable modulus and strength to  $Al_2O_3$ /polymer counterparts. The composite nature of the NiB/polymer micro-lattices implies a higher density ( $100\text{-}2000 \text{ kg.m}^{-3}$ ) resulting in a large range of modulus ( $10\text{-}3000 \text{ MPa}$ ) and strength ( $0.5\text{-}150 \text{ MPa}$ ). These structures show much larger strength than their hollow counterparts, whether they are metal-based [35, 16, 15] or ceramic-based. The NiB/polymer composites with high densities outperform the NiP hollow micro-lattices [16] and solid  $Al_2O_3$  microlattices [15]. This makes these

materials good candidates for porous electrodes, energy conversion or biomedical devices.

### 7.2 Expanding the material property space

In the introduction, we stated that our ultimate goal was to explore the mechanical properties of 3D architected metals to expand the material property space. The results of the mechanical tests that we performed during this thesis are summarized in Figure 7.3, which plots the compressive strength against density. We produced metals and cellular micro-architectures with densities spanning from 100 to 8900 kg.m<sup>3</sup>, with compressive strengths varying between 0.3 to 689 MPa. To accomplish this, we combined the following strengthening strategies:

- the microstructure in electrodeposited nt-Cu,
- the microstructure and the cellular structure in the case of regular porous Ni
- the microstructure and the architecture in the case of 3D metal-polymer hybrid micro-architectures

The NiB/polymer micro-architectures populate the low density area of the material property space. Most micro-architectures are located at the border between the envelope for the foams and the white space. At the other end of the density scale, we substantially changed the mechanical properties at constant density by tuning the microstructure of pure Cu. By changing the orientation of nanoscale twins in electrodeposited copper, the strength was varied by a factor of two at constant density. At intermediate densities, we find the Ni inverse opals, which demonstrate a strength similar to bulk copper for just the third of the density.

### 7.3 Towards a unified scaling law including the size effects

In this thesis, we experimentally investigated the size effects in cellular metals at the micron scale and how they interact with each other. Each size effect is the results from a different physical phenomenon: a geometry parameter for the architecture, and the dislocation activity for the intrinsic and extrinsic size effect. It is therefore challenging to propose a model that would capture all these possibilities.

### 7.3. Towards a unified scaling law including the size effects

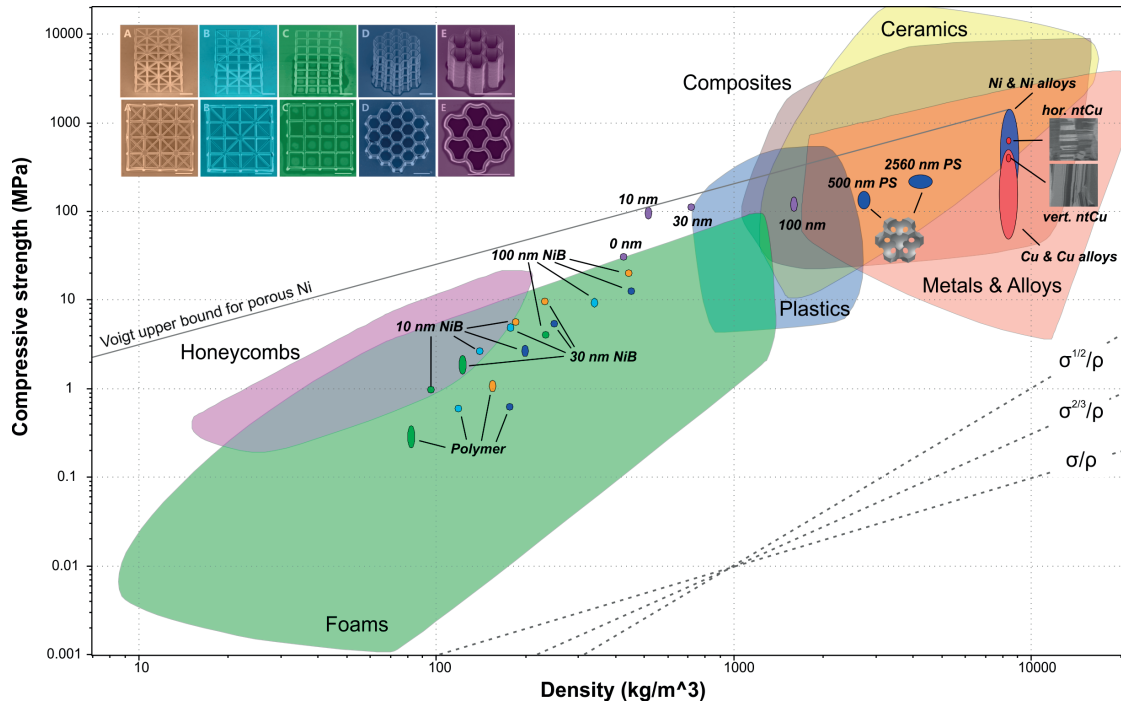


Figure 7.3 – A strength versus density chart showing the position in the material property space of nanotwinned Cu, Ni inverse opals and 3D hybrid micro-lattices. Material properties are obtained from the Software CES Edupack.

In 2007, Hodge et al. [28] already started to develop a scaling law that included the effect of the ligament size on the mechanical properties of metal foams:

$$\sigma^* = C_1 \left( \sigma_0 + \frac{k}{\sqrt{L}} \right) \left( \frac{\rho^*}{\rho_s} \right)^{3/2} \quad (7.4)$$

This equation is based on the classic scaling law for porous material, except that the strength of the parent material is now size-dependent and follow a Hall-Petch type of equation with the characteristic dimension L. Let's call d, the grain size and D, the sample dimension or ligament size. We can therefore apply this model for a crystalline metal where L takes the value of D, d or an effective length scale  $1/d + 1/D$  in equation 7.4. In that case:

#### 1. Crystalline metal

- single crystal or  $D \ll d$ : the characteristic dimension is given by the sample dimension or the ligament size, *i.e.*  $L=D$ . It means that the strength is governed by sample size only. As the external dimension is reduced, the strength increases.

## Chapter 7. General discussion

---

- polycrystalline: the characteristic dimension is given by the grain size, *i.e.*  $L=d$ . The strength scales with the inverse of the grain size according to the Hall-Petch relationship.
- $D/d < 10$ : in this intermediate regime in which both the grain size and ligament size interact with each other, an effective length is defined as a combination of both parameters,  $\frac{1}{L} = \frac{1}{D} + \frac{1}{d}$ .

### 2. Amorphous metal

For amorphous metals, a brittle-to-ductile transition is observed as the external dimension is reduced. This transition occurs at the critical thickness which is given by Equation 4.2,  $t_{cr} = \frac{2\sqrt{2}E\Gamma}{\sigma_y^2 A}$ . Based on the sample dimension, one can predict the preferred deformation behavior as follows:

- $L > t_{cr}$ : brittle failure of the structure.
- $L < t_{cr}$ : elasto-plastic collapse of the micro-architectures.

Note that the parameters  $\sigma_o$  and  $k$  in equation 7.4 depend on the type of microstructure and should be determined for each material system. This tentative model only gives the important parameters to include for developing a functional model. If one wants to develop a functional model, more systematic studies are required. But we believe that the nickel inverse opals is a very good model material to carry out this work because the grain size and ligament can be finely controlled.



# Conclusions & Future work

## Conclusions

The purpose of this dissertation was to analyze the influence of size effects on the mechanical properties of 3D metal structures with tailored microstructure. To this end, electrochemical deposition of metal films and structures, micro-mechanical tests, and extensive structural and microstructural investigations were carried out. The main conclusions can be summarized as follows:

- We were able to control the **intrinsic size effect** in metals by controlling the microstructure during electrodeposition: from an amorphous structure (NiB coating on 3D micro-lattice), to nanocrystalline nickel (Ni inverse opals) and copper with engineered grain boundaries. This range of microstructures provides a large range of mechanical properties relevant to our study. To illustrate the intrinsic size effect in metals, we focused our attention on the electrodeposition and mechanical properties of copper with nanoscale twins. Copper films with highly-oriented nanoscale twins – both horizontally and vertically – exhibited outstanding mechanical properties and a strong mechanical anisotropy. This mechanical anisotropy was related to a change in the dislocation activity as a function of the twin orientation. This work highlights the potential of controlling the microstructure in fcc metals to tailor their mechanical properties.
- We were able to control the **extrinsic size effect** in metals by depositing inside a colloidal crystal template and onto a 3D polymer template via electrochemical routes. In the former case, the Ni metal is confined by the microsphere arrangement. Therefore one can control the ligament size by modifying the microsphere diameter and consequently

## Conclusions & Future work

---

tune the mechanical properties by virtue of the "smaller is stronger" effect. In the latter, the amorphous NiB coating is produced by electroless deposition, which allows us to deposit very thin conformal metal layer. Given the amorphous microstructure, the thickness of the NiB layer governs the failure mechanism through a brittle-to-ductile transition.

- The undertaken experiments suggested a complex interaction between the size effects and the cellular structure of porous metals. The mechanical response of NiB/ polymer hybrid microarchitectures relies on two distinct effects. The mechanical properties and energy absorption capability are determined by the onset of plasticity (*i.e.* extrinsic size effect) and/or buckling behavior (*i.e.* architecture effect) depending on the NiB thickness.

## Future work and outlook

This research has experimentally shown that tailored mechanical properties arise from the combination of metal size effects and well-designed micro-architectures. This was made possible by merging advanced microfabrication techniques and characterization tools with state-of-the-art micro-mechanical tests. Ultimately, we believe that using the demonstrated approaches could further extend the material property space.

To complete the results and confirm the trend observed in this work, we suggest the following experimental investigations:

- The mechanical properties of nt-Cu were measured for two twin orientations. It would be interesting to test additional intermediate orientations to get the full evolution of the mechanical properties.
- Our promising results concerning the interaction of the intrinsic and extrinsic size effects in regular porous metals should be validated with a broader range of grain sizes, ligaments sizes and relative densities. The grain sizes can be tuned by annealing or electroplating. The ligament size can be modified by using smaller or larger polystyrene microspheres. Concerning the relative density, several approaches are possible: vary the

---

annealing time of the colloidal crystal, prepare an inverse opal from a binary colloidal crystal [129], or perform an electropolishing step on the Ni inverse opal to uniformly dissolve the metal [130].

- An interesting prospect would be to reduce the boron content of the NiB/polymer hybrid microarchitectures by changing the plating conditions. This will make the NiB deposit crystalline with modified mechanical properties. Another possibility to improve the understanding of cellular metals would be to remove the polymer core to achieve hollow metal micro-architectures. This would drastically reduce the density, while retaining good mechanical properties.

The work described in this thesis contributes to the current trend of merging several manufacturing and synthesizing techniques to produce materials with novel properties. We believe that we can go even further and we therefore recommend:

- investigating novel microstructures such as gradient microstructure, alternating microstructures, and co-deposition for multilayers or metallic nanocomposites. All of these advanced microstructures can be achieved by electrochemical deposition.
- combining electroless deposition of thin films with atomic layer deposition of ceramics or oxides to produce multilayers and multifunctional materials on polymeric templates.

The mechanical testing of 3D micro-cellular metals requires complex instrumented nanoindentation systems designed to perform quasi-static tests. However, the new capabilities of the mechanical testing systems now offer the possibility to:

- Perform temperature-dependent microcompression tests at elevated or cryogenic temperature [131] to extract the activation energies of such 3D structures.
- Perform dynamic mechanical tests [132] such as cycling loading or vibrational tests to look into catastrophic failure of such structures in relation with design variables at the micron-scale and the material size effects.

Finally, scaling up the manufacturing of such cellular metals designed in the laboratory and

## **Conclusions & Future work**

---

incorporating them into real world applications such as MEMS devices or LiGA parts is the next step to demonstrate their potential and change the way we think about materials.

# Bibliography

- [1] Michael F. Ashby. Chapter 4 - material property charts. In M.F. Ashby, editor, *Materials Selection in Mechanical Design*, pages 57 – 96. Butterworth-Heinemann, Oxford, fourth edition, 2011. doi: <https://doi.org/10.1016/B978-1-85617-663-7.00004-7>.
- [2] M. Ashby. Designing architected materials. *Scripta Materialia*, 68(1):4–7, 2013. doi: [10.1016/j.scriptamat.2012.04.033](https://doi.org/10.1016/j.scriptamat.2012.04.033).
- [3] A. Argon. *Strengthening Mechanisms in Crystal Plasticity*. Oxford University Press, 2008. doi: [10.1080/00107514.2013.857723](https://doi.org/10.1080/00107514.2013.857723).
- [4] N. A. Fleck, V. S. Deshpande, and M. F. Ashby. Micro-architected materials: past, present and future. *Proceedings of the Royal Society A: Mathematical, Physical and Engineering Sciences*, 466(2121):2495–2516, 2010. doi: [10.1098/rspa.2010.0215](https://doi.org/10.1098/rspa.2010.0215).
- [5] R. Goodall and A. Mortensen. Porous Metals. In *Physical Metallurgy*, volume 2, pages 2399–2595. Elsevier B.V., fifth edition, 2013. doi: [10.1016/B978-0-444-53770-6.00024-1](https://doi.org/10.1016/B978-0-444-53770-6.00024-1).
- [6] J. Stampfl, H. E. Pettermann, and M. H. Luxner. Three-Dimensional Open Cell Structures: Evaluation and Fabrication by Additive Manufacturing. In *Fabrication and Characterization in the Micro-Nano Range*, volume 10 of *Advanced Structured Materials*, pages 95–111. Springer Berlin Heidelberg, 2011. doi: [10.1007/978-3-642-17782-8](https://doi.org/10.1007/978-3-642-17782-8).
- [7] T. Bückmann, N. Stenger, M. Kadic, J. Kaschke, A. Frölich, T. Kennerknecht, C. Eberl, M. Thiel, and M. Wegener. Tailored 3D mechanical metamaterials made by dip-in direct-laser-writing optical lithography. *Advanced materials*, 24(20):2710–2714, 2012. doi: [10.1002/adma.201200584](https://doi.org/10.1002/adma.201200584).
- [8] S. Babaei, J. Shim, J. C. Weaver, E. R. Chen, N. Patel, and K. Bertoldi. 3D Soft Metamaterials with Negative Poisson’s Ratio. *Advanced Materials*, 25(36):5044–5049, 2013. doi: [10.1002/adma.201200584](https://doi.org/10.1002/adma.201200584).

## Bibliography

---

- 10.1002/adma.201301986.
- [9] A. Stein and R. C. Schrodén. Colloidal crystal templating of three-dimensionally ordered macroporous solids : materials for photonics and beyond. *Solid state & materials science*, 5(2001):553–564, 2002.
- [10] Y. Yin, Z. Li, and Y. Xia. Template-Directed Growth of ( 100 ) -Oriented Colloidal Crystals. *Langmuir*, 19(100):622–631, 2003.
- [11] J. Bauer, S. Hengsbach, I. Tesari, R. Schwaiger, and O. Kraft. High-strength cellular ceramic composites with 3D microarchitecture. *Proceedings of the National Academy of Sciences*, 111(7):1–6, 2014. doi: 10.1073/pnas.1315147111.
- [12] L.R. Meza, S. Das, and J.R. Greer. Strong, lightweight, and recoverable three-dimensional ceramic nanolattices. *Science*, 345(6202):1322–1326, 2014. doi: 10.1126/science.1255908.
- [13] T.A. Schaedler, A.J. Jacobsen, A. Torrents, A.E. Sorensen, J. Lian, J.R. Greer, L. Valdevit, and W.B. Carter. Ultralight metallic microlattices. *Science (New York, N.Y.)*, 334(6058): 962–5, 2011. doi: 10.1126/science.1211649.
- [14] J. H. Pikul, Z. Dai, X. Yu, H. Zhang, T. Kim, P. V. Braun, and W. P. King. Micromechanical devices with controllable stiffness fabricated from regular 3D porous materials. *Journal of Micromechanics and Microengineering*, 24(10):105006, 2014. doi: 10.1088/0960-1317/24/10/105006.
- [15] X. Zheng, H. Lee, T. H. Weisgraber, M. Shusteff, J. DeOtte, E. B. Duoss, J. D. Kuntz, M. M. Biener, Q. Ge, J. A. Jackson, S. O. Kucheyev, N. X. Fang, and C. M. Spadaccini. Ultralight, Ultrastiff Mechanical Metamaterials. *Science*, 344(6190):1373–1377, 2014. doi: 10.1126/science.1252291.
- [16] L. Valdevit, S.W. Godfrey, T.A. Schaedler, A.J. Jacobsen, and W.B. Carter. Compressive strength of hollow microlattices: Experimental characterization, modeling, and optimal design. *Journal of Materials Research*, 28(17):2461–2473, 2013. doi: 10.1557/jmr.2013.160.
- [17] M.F. Ashby. The properties of foams and lattices. *Philosophical transactions. Series A, Mathematical, physical, and engineering sciences*, 364(1838):15–30, 2006. doi: 10.1098/rsta.2005.1678.

- [18] J. Lian, D. Jang, L. Valdevit, T. A. Schaedler, A. J. Jacobsen, W. B. Carter, and J. R. Greer. Catastrophic vs Gradual Collapse of Thin-Walled Nanocrystalline Ni. *Nano letters*, 11(10):4118–4125, 2011.
- [19] O. Sigmund and S. Torquato. Design of Materials With Extreme Thermal Expansion Using a Three-Phase Topology. *Journal of the Mechanics and Physics of Solids*, 45(6):1037–1067, 1997. doi: 10.1016/S0022-5096(96)00114-7.
- [20] C.A. Steeves, S.L. dos Santos e Lucato, M. He, E. Antinucci, J.W. Hutchinson, and A.G. Evans. Concepts for structurally robust materials that combine low thermal expansion with high stiffness. *Journal of the Mechanics and Physics of Solids*, 55(9):1803–1822, 2007. doi: 10.1016/j.jmps.2007.02.009.
- [21] N.M.A. Palumbo, C.W. Smith, W. Miller, and K.E. Evans. Near-zero thermal expansivity 2-D lattice structures: Performance in terms of mass and mechanical properties. *Acta Materialia*, 59(6):2392–2403, 2011. doi: 10.1016/j.actamat.2010.12.037.
- [22] C. I. Hammetter. Pyramidal Lattice Structures for High Strength and Energy Absorption. *Journal of Applied Mechanics*, 81(1):041015, 2013. doi: 10.1115/1.4024408.
- [23] M.F. Ashby. The Mechanical Properties of Cellular Solids. *Metallurgical Transactions A*, 14:1755–1769, 1983.
- [24] V.S. Deshpande, M.F. Ashby, and N.A. Fleck. Foam topology: bending versus stretching dominated architectures. *Acta Materialia*, 49(6):1035–1040, 2001. doi: 10.1016/S1359-6454(00)00379-7.
- [25] B. Jiang, C. He, N. Zhao, C. Nash, Pand Shi, and Z. Wang. Ultralight metal foams. *Scientific Reports*, 5:1–8, 2015. doi: 10.1038/srep13825.
- [26] A. Fallet, P. Lhuissier, L. Solvo, and Y. Bréchet. Mechanical behaviour of metallic hollow spheres foam. *Advanced Engineering Materials*, 10(9):858–862, 2008. doi: 10.1002/adem.200800094.
- [27] R. Zhu, M.A. McLachlan, D.W. McComb, and M.P. Ryan. Electrochemically Grown Metallic Inverse Opals. *ECS Transactions*, 13(18):1–6, 2008.
- [28] A.M. Hodge, J. Biener, J.R. Hayes, P.M. Bythrow, C.A. Volkert, and A.V. Hamza. Scaling equation for yield strength of nanoporous open-cell foams. *Acta Materialia*, 55(4):

## Bibliography

---

- 1343–1349, 2007. doi: 10.1016/j.actamat.2006.09.038.
- [29] C. A. Volkert, E. T. Lilleodden, D. Kramer, and J. Weissmüller. Approaching the theoretical strength in nanoporous Au. *Applied Physics Letters*, 89(6):10–13, 2006. doi: 10.1063/1.2240109.
- [30] J. Biener, A.M. Hodge, J.R. Hayes, C. a Volkert, L.A. Zepeda-Ruiz, A.V. Hamza, and F.F. Abraham. Size effects on the mechanical behavior of nanoporous Au. *Nano letters*, 6(10):2379–82, 2006. doi: 10.1021/nl061978i.
- [31] I.-Chung Cheng and Andrea M. Hodge. Strength scale behavior of nanoporous Ag, Pd and Cu foams. *Scripta Materialia*, 69(4):295–298, 2013.
- [32] W.S. Sanders and L.J. Gibson. Mechanics of BCC and FCC hollow-sphere foams. 352(1-2):150–161, 2003. doi: 10.1016/S0921-5093(02)00890-0.
- [33] J. Bauer, L.R. Meza, T.A. Schaedler, R. Schwaiger, Xi. Zheng, and L. Valdevit. Nanolattices: An Emerging Class of Mechanical Metamaterials. *Advanced Materials*, 1701850:1–26, 2017. doi: 10.1002/adma.201701850.
- [34] L.C Montemayor and J.R. Greer. Mechanical response of metallic nanolattices: combining structural and material size effects. *Journal of Applied Mechanics*, 82:1–10, 2015. doi: 10.1115/1.4030361.
- [35] J. Rys, L. Valdevit, T.A. Schaedler, A.J. Jacobsen, W.B. Carter, and J.R. Greer. Fabrication and Deformation of Metallic Glass Micro-Lattices. *Advanced Engineering Materials*, 16:889–896, 2014. doi: 10.1002/adem.201300454.
- [36] D. Jang, L. R Meza, F. Greer, and J. R Greer. Fabrication and deformation of three-dimensional hollow ceramic nanostructures. 12(10):893–898, 2013. doi: 10.1038/nmat3738.
- [37] K.S. Siow, A.A.O. Tay, and P. Oruganti. Mechanical properties of nanocrystalline copper and nickel. *Materials Science and Technology*, 20(3):285–294, 2004. doi: 10.1179/026708304225010460.
- [38] A. Misra, J.P. Hirth, and R.G. Hoagland. Length-scale-dependent deformation mechanisms in incoherent metallic multilayered composites. *Acta Materialia*, 53:4817–4824, 2005. doi: 10.1016/j.actamat.2005.06.025.



- [39] N. Hansen. Hall–Petch relation and boundary strengthening. *Scripta Materialia*, 51(8): 801–806, 2004. doi: 10.1016/j.scriptamat.2004.06.002.
- [40] E.O. Hall. The Deformation and Ageing of Mild Steel: III Discussion of Results. *Proceedings of the Physical Society. Section B*, 64(9):747–753, 1951. doi: 10.1088/0370-1301/64/9/303.
- [41] N.J. Petch. The Cleavage Strength of Polycrystals. *The Journal of Iron and Steel Institute*, 173:25–30, 1953.
- [42] J.R. Trelewicz and C.A. Schuh. The Hall-Petch breakdown in nanocrystalline metals: A crossover to glass-like deformation. *Acta Materialia*, 55(17):5948–5958, 2007. doi: 10.1016/j.actamat.2007.07.020.
- [43] L. Lu, Y. Shen, X. Chen, L. Qian, and K. Lu. Ultrahigh strength and high electrical conductivity in copper. *Science*, 304(5669):422–6, 2004. doi: 10.1126/science.1092905.
- [44] J.R. Greer and J.Th.M. De Hosson. Plasticity in small-sized metallic systems: Intrinsic versus extrinsic size effect. *Progress in Materials Science*, 56(6):654–724, 2011. doi: 10.1016/j.pmatsci.2011.01.005.
- [45] Z.S. You, L. Lu, and K. Lu. Tensile behavior of columnar grained Cu with preferentially oriented nanoscale twins. *Acta Materialia*, 59(18):6927–6937, 2011. doi: 10.1016/j.actamat.2011.07.044.
- [46] L. Zhu, H. Ruan, X. Li, M. Dao, H. Gao, and J. Lu. Modeling grain size dependent optimal twin spacing for achieving ultimate high strength and related high ductility in nanotwinned metals. *Acta Materialia*, 59(14):5544–5557, 2011. doi: 10.1016/j.actamat.2011.05.027.
- [47] M. Dao, L. Lu, Y.F. Shen, and S. Suresh. Strength, strain-rate sensitivity and ductility of copper with nanoscale twins. *Acta Materialia*, 54(20):5421–5432, 2006. doi: 10.1016/j.actamat.2006.06.062.
- [48] Y.F. Shen, L. Lu, M. Dao, and S. Suresh. Strain rate sensitivity of Cu with nanoscale twins. *Scripta Materialia*, 55(4):319–322, 2006. doi: 10.1016/j.scriptamat.2006.04.046.
- [49] L. Lu, R. Schwaiger, Z.W. Shan, M. Dao, K. Lu, and S. Suresh. Nano-sized twins induce high rate sensitivity of flow stress in pure copper. *Acta Materialia*, 53(7):2169–2179, 2005.

## Bibliography

---

- doi: 10.1016/j.actamat.2005.01.031.
- [50] D. Jang, X. Li, H. Gao, and J.R. Greer. Deformation mechanisms in nanotwinned metal nanopillars. *Nature nanotechnology*, 7(9):594–601, 2012. doi: 10.1038/nnano.2012.116.
- [51] J.C. Ye, Y.M. Wang, T.W. Barbee, and A.V. Hamza. Orientation-dependent hardness and strain rate sensitivity in nanotwin copper. *Applied Physics Letters*, 100(26):261912, 2012. doi: 10.1063/1.4731242.
- [52] Z. You, X. Li, L. Gui, Q. Lu, T. Zhu, H. Gao, and L. Lu. Plastic anisotropy and associated deformation mechanisms in nanotwinned metals. *Acta Materialia*, 61(1):217–227, 2013. doi: 10.1016/j.actamat.2012.09.052.
- [53] J.R. Greer, W.C. Oliver, and W.D. Nix. Size dependence of mechanical properties of gold at the micron scale in the absence of strain gradients. *Acta Materialia*, 53(6):1821–1830, 2005. doi: 10.1016/j.actamat.2004.12.031.
- [54] J.M. Wheeler, R. Raghavan, V. Chawla, J. Zechner, I. Utke, and J. Michler. Failure mechanisms in metal–metal nanolaminates at elevated temperatures: Microcompression of Cu–W multilayers. *Scripta Materialia*, 98:28–31, 2015. doi: 10.1016/j.scriptamat.2014.11.007.
- [55] D.M. Dimiduk, M.D. Uchic, and T.A. Parthasarathy. Size-affected single-slip behavior of pure nickel microcrystals. *Acta Materialia*, 53(15):4065–4077, 2005. doi: 10.1016/j.actamat.2005.05.023.
- [56] W.D. Nix. Mechanical Properties of Thin Films. *Metallurgical Transactions A*, 20:2217–2245, 1989.
- [57] J.R. Greer and W.D. Nix. Nanoscale gold pillars strengthened through dislocation starvation. *Physical Review B - Condensed Matter and Materials Physics*, 73(24):1–6, 2006. doi: 10.1103/PhysRevB.73.245410.
- [58] E.S. Park. *Applied Microscopy*, 45(2):63–73, 2015. doi: 10.9729/AM.2015.45.2.63.
- [59] D. Z. Chen, D. Jang, K. M. Guan, Q. An, W. a. Goddard, and J. R. Greer. Nanometallic glasses: Size reduction brings ductility, surface state drives its extent. *Nano Letters*, 13(9):4462–4468, 2013. doi: 10.1021/nl402384r.
- [60] M. Yoshino, Y. Nonaka, J. Sasano, I. Matsuda, Y. Shacham-Diamand, and T. Osaka. All-

- wet fabrication process for ULSI interconnect technologies. *Electrochimica Acta*, 51(5): 916–920, 2005. doi: 10.1016/j.electacta.2005.04.069.
- [61] X. Chen, X. Liu, P. Childs, N. Brandon, and B. Wu. A Low Cost Desktop Electrochemical Metal 3D Printer. *Advanced Materials Technologies*, 1700148:1700148, 2017. doi: 10.1002/admt.201700148.
- [62] P. Jiang and M.J. McFarland. Large-scale fabrication of wafer-size colloidal crystals, macroporous polymers and nanocomposites by spin-coating. *Journal of the American Chemical Society*, 126(42):13778–13786, 2004. doi: 10.1021/ja0470923.
- [63] G.D. Moon, T.I. Lee, B. Kim, G. Chae, J. Kim, S. Kim, J. Myoung, and U. Jeong. Assembled monolayers of hydrophilic particles on water surfaces. *ACS nano*, 5(11):8600–12, 2011. doi: 10.1021/nn202733f.
- [64] Y. Fu, Z. Jin, G. Liu, and Y. Yin. Self-assembly of polystyrene sphere colloidal crystals by in situ solvent evaporation method. *Synthetic Metals*, 159:1744–1750, 2009. doi: 10.1016/j.synthmet.2009.05.017.
- [65] H. Míguez, F. Meseguer, C. López, A. Blanco, J.S. Moya, J. Requena, A. Mifsud, and V. Fornés. Control of the Photonic Crystal Properties of fcc-Packed Submicrometer SiO<sub>2</sub> Spheres by Sintering. *Advanced materials*, 10(6):480–483, 1998. doi: 10.1002/(SICI)1521-4095(199804)10:6<480::AID-ADMA480>3.0.CO;2-Y.
- [66] A L Rogach, N A Kotov, D S Koktysh, J W Ostrander, and G A Ragoisha. Electrophoretic Deposition of Latex-Based 3D Colloidal Photonic Crystals : A Technique for Rapid Production of High-Quality Opals. *Chemistry of Materials*, 12(9):2721–2726, 2000. doi: 10.1021/cm000274l.
- [67] G. Genolet and H. Lorenz. UV-LIGA: From development to commercialization. *Micro-machines*, 5(3):486–495, 2014. doi: 10.3390/mi5030486.
- [68] L.T. Romankiw. A path: from electroplating through lithographic masks in electronics to LIGA in MEMS. *Electrochimica Acta*, 42(20-22):2985–3005, 1997. doi: 10.1016/S0013-4686(97)00146-1.
- [69] P.C. Andricacos, C. Uzoh, J.O. Dukovic, J. Horkans, and H. Deligianni. Damascene copper electroplating for chip interconnections. *IBM Journal of Research and Development*, 42(5):567–574, 1998.

## Bibliography

---

- [70] M. Hasegawa, Y. Negishi, T. Nakanishi, and T. Osaka. Effects of Additives on Copper Electrodeposition in Submicrometer Trenches. *Journal of The Electrochemical Society*, 152(4):C221, 2005. doi: 10.1149/1.1867672.
- [71] S Maruo, O Nakamura, and S Kawata. Three-dimensional microfabrication with two-photon-absorbed photopolymerization. *Optics letters*, 22(2):132–134, 1997. doi: 10.1364/OL.22.000132.
- [72] J. Fischer and M. Wegener. Three-dimensional direct laser writing inspired by stimulated-emission-depletion microscopy. *Opt. Mater. Express*, 1(4):614–624, 2011. doi: 10.1364/OME.1.000614.
- [73] L. Ding, W. Yuren, M. Wenjie, C. He, X. Taohua, and Y. Can. The key factors in fabrication of high-quality ordered macroporous copper film. *Applied Surface Science*, 254(21): 6775–6778, 2008. doi: 10.1016/j.apsusc.2008.04.079.
- [74] S. Heitkam, W. Drenckhan, and J. Fröhlich. Packing spheres tightly: Influence of mechanical stability on close-packed sphere structures. *Physical Review Letters*, 108(14): 1–5, 2012. doi: 10.1103/PhysRevLett.108.148302.
- [75] H. Nishiyama and Y. Hirata. Femtosecond laser nonlinear lithography. In Michael Wang, editor, *Lithography*, chapter 04. InTech, Rijeka, 2010. doi: 10.5772/8170.
- [76] A.M. El-Sherik and U. Erb. Synthesis of bulk nanocrystalline nickel by pulsed electrodeposition. *Journal of Materials Science*, 30(22):5743–5749, 1995. doi: 10.1007/BF00356715.
- [77] M. Charbonnier and M. Romand. Polymer pretreatments for enhanced adhesion of metals deposited by the electroless process. *International Journal of Adhesion and Adhesives*, 23(4):277–285, 2003. doi: 10.1016/S0143-7496(03)00045-9.
- [78] W.J. Dressick, C.S. Dulcey, J.H. Georger, G.S. Calabrese, and J.M. Calvert. Covalent Binding of Pd Catalysts to Ligating Self-Assembled Monolayer Films for Selective Electroless Metal Deposition. *Journal of The Electrochemical Society*, 141(1):210, 1994. doi: 10.1149/1.2054686.
- [79] M. Yoshino, H. Aramaki, I. Matsuda, Y. Okinaka, and T. Osaka. Effect of Organosilane Underlayers on the Effectiveness of NiB Barrier Layers in ULSI Metallization. *Electrochemical and Solid-State Letters*, 12(4):D19–D21, 2009. doi: 10.1149/1.3072778.

- [80] K. Jung Huh, Y. and Hong and K. S. Shin. Amorphization induced by focused ion beam milling in metallic and electronic materials. *Microscopy and Microanalysis*, 19(S5):33–37, 2013. doi: 10.1017/S1431927613012282.
- [81] W.C. Oliver and G.M. Pharr. Measurement of hardness and elastic modulus by instrumented indentation: Advances in understanding and refinements to methodology. *Journal of Materials Research*, 19(01):3–20, 2011. doi: 10.1557/jmr.2004.19.1.3.
- [82] I.N. Sneddon. The relation between load and penetration in the axisymmetric boussinesq problem for a punch of arbitrary profile. *International journal of engineering science*, 3(1):47–57, 1965.
- [83] M. Hasegawa, M. Mieszala, Y. Zhang, R. Erni, J. n Michler, and L. Philippe. Orientation-controlled nanotwinned copper prepared by electrodeposition. *Electrochimica Acta*, 178:458–467, 2015. doi: 10.1016/j.electacta.2015.08.022.
- [84] M. Mieszala, G. Guillonneau, M. Hasegawa, R. Raghavan, J.M. Wheeler, S. Mischler, J. Michler, and L. Philippe. Orientation-dependent mechanical behaviour of electrodeposited copper with nanoscale twins. *Nanoscale*, 8(35):15999–16004, 2016. doi: 10.1039/C6NR05116B.
- [85] Y.-S. Wang, W.-H. Lee, S.-C. Chang, J.-N. Nian, and Y.-L. Wang. An electroplating method for copper plane twin boundary manufacturing. *Thin Solid Films*, 544:157–161, 2013. doi: 10.1016/j.tsf.2013.03.131.
- [86] N. Lu, K. Du, L. Lu, and H.Q. Ye. Transition of dislocation nucleation induced by local stress concentration in nanotwinned copper. *Nature communications*, 6:7648, 2015. doi: 10.1038/ncomms8648.
- [87] V.A. Vas’ko, I. Tabakovic, and S.C. Riemer. Structure and Room-Temperature Recrystallization of Electrodeposited Copper. *Electrochemical and Solid-State Letters*, 6(7): 100–102, 2003. doi: 10.1149/1.1575592.
- [88] T.C. Chan, Y.L. Chueh, and C.N. Liao. Manipulating the crystallographic texture of nanotwinned Cu films by electrodeposition. *Crystal Growth and Design*, 11(11):4970–4974, 2011. doi: 10.1021/cg200877f.
- [89] V. Maier, K. Durst, J. Mueller, B. Backes, H. Höppel, and M. Göken. Nanoindentation strain-rate jump tests for determining the local strain-rate sensitivity in nanocrystalline

## Bibliography

---

- Ni and ultrafine-grained Al. *Journal of Materials Research*, 26(11):1421–1430, 2011. doi: 10.1557/jmr.2011.156.
- [90] Y.M. Wang, R.T. Ott, T. van Buuren, T.M. Willey, M.M. Biener, and A.V. Hamza. Controlling factors in tensile deformation of nanocrystalline cobalt and nickel. *Physical Review B*, 85(1):014101, 2012. doi: 10.1103/PhysRevB.85.014101.
- [91] H. Conrad. Plastic deformation kinetics in nanocrystalline FCC metals based on the pile-up of dislocations. *Nanotechnology*, 18:1–8, 2007. doi: 10.1088/0957-4484/18/32/325701.
- [92] G. Mohanty, J.M. Wheeler, R. Raghavan, J. Wehrs, M. Hasegawa, S. Mischler, L. Philippe, and J. Michler. Elevated temperature, strain rate jump microcompression of nanocrystalline nickel. *Philosophical Magazine*, 95(16-18):1878–1895, 2015. doi: 10.1080/14786435.2014.951709.
- [93] David E.J. Armstrong, Angus J. Wilkinson, and Steve G. Roberts. Measuring anisotropy in Young’s modulus of copper using microcantilever testing. *Journal of Materials Research*, 24(11):3268–3276, 2009. doi: 10.1557/jmr.2009.0396.
- [94] H. Zhang, B. E. Schuster, Q. Wei, and K. T. Ramesh. The design of accurate micro-compression experiments. *Scripta Materialia*, 54(2):181–186, 2006. doi: 10.1016/j.scriptamat.2005.06.043.
- [95] M. Mieszala, M. Hasegawa, G. Guillonneau, J. Bauer, R. Raghavan, C. Frantz, O. Kraft, S. Mischler, J. Michler, and L. Philippe. Micromechanics of Amorphous Metal / Polymer Hybrid Structures with 3D Cellular Architectures : Size Effects , Buckling Behavior , and Energy Absorption Capability. *Small*, 13(8):1602514, 2017. doi: 10.1002/smll.201602514.
- [96] O.V. Safonova, L.N. Vykhodtseva, L.A. Fishgoit, N.N. Kononkova, P. Glatzel, and V.A. Safonov. Elucidation of the chemical state of phosphorus and boron in crystallographically amorphous nickel electroplates. *Russian Journal of Electrochemistry*, 46(11):1223–1229, 2010. doi: 10.1134/S1023193510110030.
- [97] W. Thomas Evans and M. Schlesinger. The Effect of Solution pH and Heat-Treatment on the Properties of Electroless Nickel Boron Films. *Journal of the Electrochemical Society*, 141(1):78–82, 1994.
- [98] V. Vitry, A.-F. Kanta, J. Dille, and F. Delaunois. Structural state of electroless nickel–boron

- deposits (5wt.% B): Characterization by XRD and TEM. *Surface and Coatings Technology*, 206(16):3444–3449, 2012. doi: 10.1016/j.surfcoat.2012.02.003.
- [99] B. Oraon, G. Majumdar, and B. Ghosh. Improving hardness of electroless Ni–B coatings using optimized deposition conditions and annealing. *Materials & Design*, 29(7):1412–1418, 2008. doi: 10.1016/j.matdes.2007.09.005.
- [100] A. Dominguez-Rios, C. and Hurtado-Macias, R. Torres-Sanchez, M.A. Ramos, and J. Gonzales-Hernandez. Measurement of Mechanical Properties of an Electroless Ni-B Coating Using Nanoindentation. *Industrial and Engineering Chemistry Research*, 51(22): 7762–7768, 2012.
- [101] C. Schuh, T. Hufnagel, and U. Ramamurty. Mechanical behavior of amorphous alloys. *Acta Materialia*, 55(12):4067–4109, 2007. doi: 10.1016/j.actamat.2007.01.052.
- [102] H. Guo, P.F. Yan, Y.B. Wang, J. Tan, Z.F. Zhang, M.L. Sui, and E. Ma. Tensile ductility and necking of metallic glass. *Nature materials*, 6(10):735–739, 2007. doi: 10.1038/nmat1984.
- [103] S.W. Lee, M. Jafary-Zadeh, D.Z. Chen, Y.W. Zhang, and J.R. Greer. Size Effect Suppresses Brittle Failure in Hollow Cu<sub>60</sub>Zr<sub>40</sub> Metallic Glass Nanolattices Deformed at Cryogenic Temperatures. *Nano Letters*, 15(9):5673–5681, 2015. doi: 10.1021/acs.nanolett.5b01034.
- [104] C.A. Volkert, A. Donohue, and F. Spaepen. Effect of sample size on deformation in amorphous metals. *Journal of Applied Physics*, 103(8):083539, 2008. doi: 10.1063/1.2884584.
- [105] Y. Zhang and A.L. Greer. Thickness of shear bands in metallic glasses. *Applied Physics Letters*, 89(7), 2006. doi: 10.1063/1.2336598.
- [106] F.F. Csikor, C. Motz, D. Weygand, M. Zaiser, and S. Zapperi. Dislocation avalanches, strain bursts, and the problem of plastic forming at the micrometer scale. *Science*, 318: 251–254, 2007. doi: 10.1126/science.1143719.
- [107] S.H. Chen, K.C. Chan, G. Wang, F.F. Wu, L. Xia, J.L. Ren, J. Li, K.A. Dahmen, and P.K. Liaw. Loading-rate-independent delay of catastrophic avalanches in a bulk metallic glass. *Scientific Reports*, 6:21967, 2016. doi: 10.1038/srep21967.
- [108] R. Hillebrand, F. Muller, K. Schwirn, W. Lee, and M. Steinhart. Quantitative analysis of the grain morphology in self-assembled hexagonal lattices. *ACS Nano*, 2(5):913–920,

## Bibliography

---

2008. doi: 10.1021/nn700318v.
- [109] A.C. Johnston-Peck, J. Wang, and J.B. Tracy. Formation and grain analysis of spin-cast magnetic nanoparticle monolayers. *Langmuir*, 27(8):5040–5046, 2011. doi: 10.1021/la200005q.
- [110] Y. Liu, T.A. Schaedler, A.J. Jacobsen, and X. Chen. Quasi-static energy absorption of hollow microlattice structures. *Composites Part B: Engineering*, 67:39–49, 2014. doi: 10.1016/j.compositesb.2014.06.024.
- [111] T.A. Schaedler, C.J. Ro, A.E. Sorensen, Z. Eckel, S.S. Yang, W.B. Carter, and A.J. Jacobsen. Designing metallic microlattices for energy absorber applications. *Advanced Engineering Materials*, 16(3):276–283, 2014. doi: 10.1002/adem.201300206.
- [112] S.K. Maiti, L.J. Gibson, and M.F. Ashby. Deformation and energy absorption diagrams for cellular solids. *Acta Metallurgica*, 32(11):1963–1975, 1984. doi: 10.1016/0001-6160(84)90177-9.
- [113] L.J. Gibson and M.F. Ashby. Energy absorption in cellular materials. In *Cellular Solids: Structure and Properties*, pages 309–344. Cambridge University Press, Cambridge, 1997.
- [114] C. Shim, N. Yun, R. Yu, and D. Byun. Mitigation of Blast Effects on Protective Structures by Aluminum Foam Panels. *Metals*, 2(2):170–177, 2012. doi: 10.3390/met2020170.
- [115] G.N. Karam and L.J. Gibson. Elastic buckling of cylindrical shells with elastic cores—I. Analysis. *International Journal of Solids and Structures*, 32(8-9):1259–1283, 1995. doi: 10.1016/0020-7683(94)00147-O.
- [116] L.R. Meza, A.J. Zelhofer, N. Clarke, A.J. Mateos, D.M. Kochmann, and J.R. Greer. Resilient 3D hierarchical architected metamaterials. *Proceedings of the National Academy of Sciences of the United States of America*, 112(37):11502–7, 2015. doi: 10.1073/pnas.1509120112.
- [117] C. Xiao, R.A. Mirshams, S.H. Whang, and W.M. Yin. Tensile behavior and fracture in nickel and carbon doped nanocrystalline nickel. *Materials Science and Engineering A*, 301(1):35–43, 2001. doi: 10.1016/S0921-5093(00)01392-7.
- [118] G.D. Hughes, S.D. Smith, C.S. Pande, H.R. Johnson, and R.W. Armstrong. Hall-petch strengthening for the microhardness of twelve nanometer grain diameter electrode-



- posited nickel. *Scripta Metallurgica*, 20(1):93–97, 1986. doi: 10.1016/0036-9748(86)90219-X.
- [119] C.A. Schuh, T.G. Nieh, and T. Yamasaki. Hall–petch breakdown manifested in abrasive wear resistance of nanocrystalline nickel. *Scripta Materialia*, 46(10):735 – 740, 2002. doi: [https://doi.org/10.1016/S1359-6462\(02\)00062-3](https://doi.org/10.1016/S1359-6462(02)00062-3).
- [120] F. Ebrahimi, G.R. Bourne, M.S. Kelly, and T.E. Matthews. Mechanical properties of nanocrystalline nickel produced by electrodeposition. *Nanostructured Materials*, 11(3): 343–350, 1999. doi: 10.1016/S0965-9773(99)00050-1.
- [121] A. Rinaldi, P. Peralta, C. Friesen, and K. Sieradzki. Sample-size effects in the yield behavior of nanocrystalline nickel. *Acta Materialia*, 56(3):511–517, 2008. doi: 10.1016/j.actamat.2007.09.044.
- [122] D. Jang and J.R. Greer. Size-induced weakening and grain boundary-assisted deformation in 60 nm grained Ni nanopillars. *Scripta Materialia*, 64(1):77–80, 2011. doi: 10.1016/j.scriptamat.2010.09.010.
- [123] F. Dalla Torre, H. Van Swygenhoven, and M. Victoria. Nanocrystalline electrodeposited Ni: Microstructure and tensile properties. *Acta Materialia*, 50(15):3957–3970, 2002. doi: 10.1016/S1359-6454(02)00198-2.
- [124] C.P. Frick, B.G. Clark, S. Orso, A.S. Schneider, and E. Arzt. Size effect on strength and strain hardening of small-scale [1 1 1] nickel compression pillars. *Materials Science and Engineering A*, 489(1-2):319–329, 2008. doi: 10.1016/j.msea.2007.12.038.
- [125] M.D. Uchic, D.M. Dimiduk, J.N. Florando, and W.D. Nix. Sample Dimensions Influence Strength and Crystal Plasticity. *Science*, 305(5686):986–989, 2004. doi: 10.1126/science.1098993.
- [126] C. Peng, Y. Zhong, Y. Lu, S. Narayanan, T. Zhu, and J. Lou. Strain rate dependent mechanical properties in single crystal nickel nanowires. *Applied Physics Letters*, 102(8): 8–13, 2013. doi: 10.1063/1.4793481.
- [127] D. Huang and P. Qiao. Mechanical Behavior and Size Sensitivity of Nanocrystalline Nickel Wires Using Molecular Dynamics Simulation. *Journal of Aerospace Engineering*, 24:147–153, 2011. doi: 10.1061/(ASCE)AS.1943-5525.0000006.

## Bibliography

---

- [128] R. Lontas and J.R. Greer. 3D nano-architected metallic glass: Size effect suppresses catastrophic failure. *Acta Materialia*, 133:393–407, 2017. doi: 10.1016/j.actamat.2017.05.019.
- [129] J. Wang, S. Ahl, Q. Li, M. Kreiter, T. Neumann, K. Burkert, W. Knoll, and U. Jonas. Structural and optical characterization of 3D binary colloidal crystal and inverse opal films prepared by direct co-deposition. *Journal of Materials Chemistry*, 18(9):981, 2008. doi: 10.1039/b715329e.
- [130] X. Yu, Y.-J. Lee, R. Furstenberg, J.O. White, and P.V. Braun. Filling fraction dependent properties of inverse opal metallic photonic crystals. *Advanced Materials*, 19(13):1669–1692, 2007. doi: 10.1002/adma.200602792.
- [131] J. Wehrs, M.J. Deckarm, J.M. Wheeler, X. Maeder, R. Birringer, S. Mischler, and J. Michler. Elevated temperature, micro-compression transient plasticity tests on nanocrystalline Palladium-Gold: Probing activation parameters at the lower limit of crystallinity. *Acta Materialia*, 129:124–137, 2017. doi: 10.1016/j.actamat.2017.02.045.
- [132] G. Guillonau, M. Mieszala, J. Wehrs, J. Schwiedrzik, S. Grop, D. Frey, L. Philippe, J.-M. Breguet, J. Michler, and J.M. Wheeler. Nanomechanical testing at high strain rates: new instrumentation for nanoindentation and microcompression. *Review Scientific Instruments (under revision)*, 2018.

# Curriculum Vitae

Maxime MIESZALA

Born in 1989 in Dole, France

## EDUCATION

- 2013-2017 Doctoral student  
Laboratory for Mechanics of Materials and Nanostructures  
Empa, Thun, Switzerland
- 2011-2012 Master of Science in Advanced Materials  
Cranfield University, Cranfield, UK
- 2008-2013 Diplôme d'Ingénieur in Materials Science  
Mines Albi, Albi, France

## PUBLICATIONS

- M. Hasegawa, **M. Mieszala**, Y. Zhang, R. Erni, J. Michler, Laetitia Philippe, *Orientation-controlled nanotwinned copper prepared by electrodeposition*, *Electrochimica Acta*, 178 (2015), pp 458-467. DOI: 10.1016/j.electacta.2015.08.022.
- **M. Mieszala**, G. Guillonnet, M. Hasegawa, R. Raghavan, J. Wheeler, S. Mischler, J. Michler, L. Philippe, *Orientation-dependent mechanical behaviour of electrodeposited copper with nanoscale twins*, *Nanoscale* (2016). DOI: 10.1039/C6NR05116B.
- **M. Mieszala**, M. Hasegawa, G. Guillonnet, J. Bauer, R. Raghavan, C. Frantz, O. Kraft, S. Mischler, J. Michler, L. Philippe, *Micro-mechanics of amorphous metal/polymer hybrid*

## Bibliography

---

*structures with 3D cellular architectures: size effects, buckling behavior and energy absorption capability*. *Small*, 13 (2017), 1602514. DOI: 10.1002/sml.201602514.

- **M. Mieszala**, P. Lozano Torrubia, D. Axinte, Y. Guo, J. Schwiedrzik, S. Mischler, J. Michler, L. Philippe, *Erosion mechanisms during abrasive waterjet machining: model microstructures and single impact experiments*, *Journal of Materials Processing Technology*, 247 (2017), pp 92-102. DOI: 10.1016/j.jmatprotec.2017.04.003.
- G. Guillonneau, **M. Mieszala**, J. Wehrs, J. Schwiedrzik, S. Grop, D. Frey, L. Philippe, J.M. Breguet, J. Michler, J.M. Wheeler, *Nanomechanical testing at high strain rates: new instrumentation for nanoindentation and microcompression*, submitted to *Materials & Design*.

## CONFERENCES

- *Electrodeposition of highly-textured nanotwinned copper*, presented at the 229<sup>th</sup> ECS Meeting, October 8, 2014, Cancun, Mexico.
- *Mechanical properties of electrodeposited copper films with preferentially oriented nanotwins*, presented at the E-MRS Spring Meeting, May 14, 2015, Lille, France.
- (Invited) *Electrochemical synthesis of high strength regular metal foams and 3D micro-lattices*, presented at the 229<sup>th</sup> ECS Meeting, June 1, 2016, San Diego, USA.
- *Nickel electrodeposits as a model material to study abrasive waterjet machining*, presented at the 229<sup>th</sup> ECS Meeting, June 1, 2016, San Diego, USA.
- *A study of surface/subsurface modification observed in abrasive waterjet machining using a nickel model material*, presented at the Eurocorr, September 13, 2016, Montpellier, France.
- *Effect of nanoscale twin orientation on the mechanical properties of electrodeposited copper films*, presented at the E-MRS Spring Meeting, May 22, 2017, Strasbourg, France.

